COVERAGE OPTIMIZATION USING LATTICE FLOWER CONSTELLATIONS

A Dissertation

by

SANG HYUN LEE

Submitted to the Office of Graduate and Professional Studies of
Texas A&M University
in partial fulfillment of the requirements for the degree of

DOCTOR OF PHILOSOPHY

Chair of Committee,	Daniele Mortari
Committee Members,	Thomas Pollock
	John Valasek
	Aniruddha Datta
Head of Department,	Rodney Bowersox

May 2015

Major Subject: Aerospace Engineering

Copyright 2015 Sang Hyun Lee

ABSTRACT

Recently developed satellite systems require a group of satellites acting in concert with one another to meet mission objectives. Specifying a constellation by defining all the orbit elements for each satellite is complex, inconvenient, and computationally impossible for constellations with many satellites. There are many degrees of freedom in the parameters for constellations such as number of orbital planes, number of satellites in the orbital plane, orbital inclination and altitude. Therefore, an efficient way to design to a constellation is to adopt some orbital elements with common value and some other derived by algorithms and various algorithms have been proposed. Among them, the Lattice Flower Constellations theory is more suitable to optimization of constellation design because it is a minimum parameterization theory and because this design methodology contains most of the existing methodologies as subsets.

The main contributions of this dissertation are 1) the development of an algorithm which provides uniform points on a sphere for fast evaluation of coverage fitness functions, 2) the presentation of a set of three non-classical constellation missions using Lattice Flower Constellations, and 3) the investigation of a new class of orbits, called "J_2-propelled," and associated constellations which are particularly suitable in the three-dimensional lattice theory of flower constellations.

For global coverage missions, fitness functions for constellation design are computed using globally distributed points. Most of the grid data sets are provided with a fixed step in latitude and longitude. Therefore, conventionally computed points are distributed with a fixed step in latitude and longitude. Since these are certainly not uniform distributions of points on the Earth, mainly due to the increase of point density at high latitude regions, converting these data into an "equivalent" distribution of points (with different weights) is needed. This will allow the data sets to be dramatically decreased to small amount data sets with appropriate values and, consequently, computational burden is then reduced using "equivalent" uniformly distributed points.

For elliptical constellations, the Lattice Flower Constellations require nine design parameters of which six are integers. For circular constellations, there are five required design parameters of which three are integers. A general optimization technique implies finding the optimal values of these parameters. This dissertation introduces a general process to perform constellation optimization for *any* specific optimality definition, that is, for *any* specific space mission. To demonstrate the feasibility and the effectiveness of the proposed approach this optimization tool is applied to three distinct types of space missions: a) global radio occultation, b) interferometric imaging, and c) constrained communication missions. The results obtained validate the proposed methodology.

A linear theory to design orbits and constellations where the Earth oblateness perturbation, the J_2 perturbation, generates dynamics that are periodic in an inertial or in a rotating frame is presented. In J_2-propelled orbits, the linear (secular) J_2 effect is used instead of being fought to allow the satellites accessing specific 3-dimensional volumes around the Earth. The main motivation is to design space missions (satellites and constellations) able to measure physical quantities (e.g., magnetic or electric fields) in large space volumes by limiting the control costs to compensate the other gravitational and non-gravitational orbital perturbations only.

DEDICATION

To my beloved wife Kyungoh
and my sweet daughter Susie

ACKNOWLEDGEMENTS

It is a great pleasure to thank those who made this thesis possible. I would like to begin my acknowledgements by expressing great appreciation for my advisor, Dr. Daniele Mortari, for his guidance and support throughout the course of my Ph.D. I have learned how to develop and verify my ideas for new research. He has encouraged my work and given many advices for the future career. It has been a great pleasure to discuss science with him.

I am also extremely grateful to my committee members, Dr. Thomas Pollock, Dr. John Valasek and Dr. Aniruddha Datta for their kind encouragement which helps me accomplish my research. I would like to extend my appreciation to Dr. Martìn Eugenio Avendaño Gonzales for the Java based the Lattice Flower Constellation visualization tool. It would be difficult to complete the applet without his contribution.

I am also grateful for all the lessons I've learned from the outstanding professors who taught my classes at Texas A&M University. Thanks also go to the Aerospace Engineering Department for the kind support I received throughout my doctorate program. A special thanks goes to Ms. Karen Knabe for her administrative assistance.

I offer my regard and blessings to all the members of Dr. Mortari groub. I really want to thank for their valuable discussion and friendship. Special thanks to officemates - Dr. Reza Raymond Karimi, Dr. Jonathan William Missel, Dr. Francesco de Dilectis and Stoian Borissov. Additionally, I would like to express gratitude to the Republic of Korea Air Force for providing tremendous opportunity of studying abroad for my Ph. D. degree.

Finally, I would like to thank my family. The unconditional love and support of my parents and parents-in-law have been the greatest motivation during the graduate study. And most importantly, I would like to express the deepest gratitude to most precious wife and daughter for their love and support.

NOMENCLATURE

a	Semi-major axis [km]
e	Eccentricity
i	Inclination [rad]
Ω	Right ascension of the ascending node [rad]
ω	Argument of perigee [rad]
M	Mean anomaly [rad]
h	altitude [km]
$\rho_{\min}$	minimum distance between two satellites [km]
p	Semi-latus rectum [km]
$\dot{\Omega}$	Nodal regression rate [rad/s]
$\dot{\omega}$	Perigee rotation rate [rad/s]
μ	The Earth's gravitational constant [$\mathrm{km}^3/\mathrm{s}^2$]
n	Perturbed mean motion [rad/s]
n_0	Unperturbed mean motion [rad/s]
N_o	the number of orbital planes
N_ω	the number of orbits per orbital planes
N_{so}	the number of satellites per orbit
N_c	the configuration number
T_p	the orbit nodal period
T_d	the Greenwich nodal period
N_p	the number of revolutions required to complete one period of repetition
N_d	the number of sidereal days the Earth completes during one period of repetition

J_2	second zonal harmonic coefficient
$R_\oplus$	the Earth radius [km]
$\omega_\oplus$	the Earth's rotation rate [rad/s]

TABLE OF CONTENTS

Page

LIST OF FIGURES

FIGURE Page

LIST OF TABLES

TABLE Page

1. INTRODUCTION

1.1 Background

Recently developed satellite systems require groups of artificial satellites working in concert for a common purpose. Because satellites must perform in a coordinated manner to accomplish the mission objectives, these multiple satellites are called satellite constellations. A major trend in the evolution of satellite systems is an increase in the number of smaller and cheaper satellites. This has led to a rapid increase in the number of Earth-orbiting constellations for communications, navigation, and observations. [1]. Iridium, Globalstar, and ORBCOMM [2, 3] have been developed as Low Earth orbit communications constellations. Global Positioning System (GPS) and Galileo are examples of constellations for navigation [4].

Specifying a constellation by defining all of the orbit elements for each satellite is complex, inconvenient, and overwhelming in its range of options [5]. There are many of degrees of freedom in the parameters for constellations; number of orbital planes, number of satellites in the orbital plane, orbital inclination and altitude. An efficient way to design is utilizing specific constellation algorithms with common parameters, and various patterns have been proposed by many researchers. Among them, two types of patterns are currently popular and practiced today. The Streets-of-Coverage constellations algorithm [6, 7] typically involves placing satellites in polar orbits that have been spaced such that the path covered by a satellite touches or overlaps the path from the satellite in the next plane over [6]. This algorithm has advantages in its simplicity of evaluating coverage but provides unnecessary overlapping coverage in the polar region. The Walker algorithm provides symmetric constellations [8, 9] and is more efficient for a global coverage mission. In general, classical constellation patterns have focused on satellite constellation design for coverage of the Earth in the inertial frame. However, Flower constellations provide repeating ground tracks using periodic dynamics in a Planet-Centered-Planet-Fixed rotating frame [10]. The recently developed Lattice Flower Constellations (LFC) theory [11, 12] is more suitable to optimization of constellation design because it is a minimum parameterization theory.

Each orbit depends on six parameters, and that high dimensionality complicates optimal constellation design. Therefore, the first step of optimal constellation design is selecting constellation algorithm appropriate to mission. The next step is to obtain a reasonably reduced problem dimensionality without cutting out potentially useful solutions. For elliptical constellations, the LFC require seven parameters of which three integers while for circular constellations the parameters become five of which three are integers because eccentricity and argument of perigee are not necessary. Optimizing the LFC implies finding these parameters to fulfill mission requirements. This research shows how to derive these parameters in order to minimize fitness function. Reasonable initial radius ranges can be obtained by limiting the atmospheric drag and by avoiding the inner Van Allen belt. Since the main aim of this research is to present a general procedure to optimize a constellation geometry along with mission based criterion, various examples for specific missions such as radio occultation, interferometric imaging, and constrained communication missions will be examined.

1.2 Lattice Flower Constellations Design

Important characteristics of the Lattice theory of Flower Constellation are: 1) it is a minimum-parameter design tool (no equivalency problem), and 2) the theory is independent from compatibility condition (free to use any orbit). From a mathematical point of view, the satellite's phasing is described by a regular lattice on a three-dimensional torus (each axis is an angle, modulo 2π) in a four-dimensional space.

1.2.1 2-D Lattice Flower Constellations Design

The 2-D Lattice Flower Constellations design methodology has been introduced in Ref. [13]. In general 2-D LFC are characterized by four continuous parameters (semi-major axis, eccentricity, inclination and argument of perigee) and three independent integer parameters establishing the constellation satellite distribution in the (M, Ω)-space. These integer parameters are the number of orbital planes, N_o, the number of satellites per orbit, N_{so}, and the configuration number, N_c (phasing parameter). Using these integer parameters, the satellites' right ascension of the ascending node (Ω_{ij}) and the initial mean anomaly (M_{ij}) are solutions of the following equation

$$\begin{bmatrix} N_o & 0 \\ N_c & N_{so} \end{bmatrix} \begin{Bmatrix} \Omega_{ij} \\ M_{ij} \end{Bmatrix} = 2\pi \begin{Bmatrix} i-1 \\ j-1 \end{Bmatrix} \tag{1.1}$$

where $i = 1, \cdots, N_o$, $j = 1, \cdots, N_{so}$, and $N_c \in [1, N_o]$. The "i-j" element is the j-th satellite on the i-th orbital plane. If repeating ground tracks are required, then the compatibility equation

$$N_p \, T_p = N_p \, \frac{2\pi}{n + \dot{\omega}} = N_d \, T_d = N_d \, \frac{2\pi}{\omega_\oplus - \dot{\Omega}}, \tag{1.2}$$

where T_p is the orbit nodal period and T_d is the Greenwich nodal period, provides the value of the orbit radius for each coprime integers, N_p and N_d. Equation (1.2) takes into account the main gravitational perturbation due to the Earth oblateness, known as the J_2 effect. The secular and persistent J_2 effect modifies the mean motion according to

$$n = n_0 \left[1 + \frac{3}{4} J_2 \left(\frac{R_\oplus}{p} \right)^2 (2 - 3 \sin^2 i) \sqrt{1 - e^2} \right], \tag{1.3}$$

where $R_\oplus = 6,378.14$ km is the Earth radius, $p = a(1 - e^2)$ is the orbital semi-latus rectum, $J_2 = 1.8262668355 \times 10^{-3}$ is the second zonal harmonic coefficient (non-dimensional) of the Earth gravitational field, $n_0 = \sqrt{\frac{\mu}{a^3}}$ is the unperturbed mean motion, and $\mu = 3.986 \cdot 10^5 \text{km}^3/\text{s}^2$ is the Earth's gravitational constant, and the perturbed mean motion linearly changes the right ascension of the ascending node [14, 15]

$$\dot{\Omega} = -\frac{3}{2} J_2 \left(\frac{R_\oplus}{p} \right)^2 n \cos i, \tag{1.4}$$

as well as the argument of perigee,

$$\dot{\omega} = \frac{3}{4} J_2 \left(\frac{R_\oplus}{p} \right)^2 n \, (5 \cos^2 i - 1). \tag{1.5}$$

All satellites have the same semi-major axis, eccentricity and inclination.

1.2.2 3-D Lattice Flower Constellations Design

2-D Lattice Theory has been extended to 3-D Lattice Theory of Flower Constellations (FC) [16, 12] by including the J_2 perturbation. Since the 2-D Lattice theory does not include the J_2 perturbation, from a practical point of view it can be used for circular orbits or orbits at critical inclinations ($i = 63.4°$ or $i = 116.6°$) only, as the J_2 effect will slowly destroy the initial optimal configuration. Constellation station-keeping costs will quickly become expensive. While the variation of Ω can be compensated by a proper selection of the orbital period (this variation is identical for all orbits, and consequently it will not destroy the symmetric distribution) the ω variation changes the latitudinal locations of perigee/apogee with catastrophic departure from the initial optimal configuration. Trying to keep the perigee in its location has proven to be very expensive.

By placing on the same orbital plane orbits with identical shapes that are uniformly distributed in ω, a uniform rotation of these orbits on the same orbital plane is obtained, and this plane is rotating about the Earth spin axis. Satellite phasing is described by the solution of

$$\begin{bmatrix} N_o & 0 & 0 \\ N_{c3} & N_\omega & 0 \\ N_{c1} & N_{c2} & N_{so} \end{bmatrix} \begin{Bmatrix} \Omega_{ikj} \\ \omega_{ikj} \\ M_{ikj} \end{Bmatrix} = 2\pi \begin{Bmatrix} i-1 \\ k-1 \\ j-1 \end{Bmatrix} \bmod (2\pi) \tag{1.6}$$

where N_o is the number of orbital planes, N_ω the number of orbits per orbital plane, N_{so} the number of satellites per orbit, $i \in [1, N_o]$, $j \in [1, N_{so}]$, $k \in [1, N_\omega]$, and $N_{c1} \in [1, N_o]$, $N_{c2} \in [1, N_\omega]$, and $N_{c3} \in [1, N_o]$ are three integers (called configuration numbers) identifying the satellite phasing. In Eq. (1.6), the indices have the following meaning: the "i, k, j" satellite indicates that it belongs to the j-th mean anomaly location of the k-th orbit belonging to the i-th orbital plane. Again, the importance of this theory consists of extending the constellation design to the use elliptical orbits at *any inclination* under the linear J_2 effect.

1.3 Research Objectives and Contributions

The objectives of this research are to develop a general approach using LFC theory to estimate the best design parameters for *any* specific optimality definition, that is, for any specific space mission application. In particular, an algorithm, providing uniform points on a sphere for faster and better fitness function evaluation, has been developed to optimize GPS-type of constellations. In addition, an entirely new class of orbits, called "J_2-propelled orbits," has been developed and investigated particularly suitable to access large space volumes around the Earth with no use of fuel.

This research provides improved algorithms based on a quasi-equal area spherical subdivision to obtain uniform distribution of points on a sphere. The proposed algorithm is fast and efficient as compared to previous approach. Consequently, it is suitable for various applications requiring high value of N and can be applied to two geographical data distributions that are modeled by quasi-uniform distribution of weighted points. The capability of uniformly distributing points on a sphere results in important application possibilities such as survey sampling, dynamic modeling and information storage, allowing the development of optimal algorithms. Therefore, this algorithm can be applied to several other scientific problems and it will help various groups to reduce surveying costs.

The proposed methods to optimize a LFC to satisfy specific mission requirements allow for promoting the acceptance of the newly developed LFC by the space community. Therefore one of the main goals of this work is that of presenting design techniques and procedures that can be applied to satisfy practical mission requirements. The proposed procedures and numerical solutions in the overall dissertation will be highly valuable in mission analysis and expected to be broadly useful for constellations designer.

The J_2-propelled orbits repeatedly cover specific volumes around the gravitational body and are particularly suitable to be adopted in the three-dimensional (3-D) LFC theory, which has been developed to include the J_2 linear perturbation. Using, rather than fighting, the J_2 perturbation directly implies long-term orbit stability, with low orbital maintenance costs that can be conveniently dedicated to compensate the non-J_2 orbital perturbations. Therefore, this new class of orbits allows research people to achieve single or multi-satellite space missions aiming to investigate the 3-Dimensional coverage of space volumes in inertial and/or Earth-rotating reference frames. Hence, these orbits are suitable to monitor physical quantities.

1.4 Dissertation Organization

This section gives a brief description of each chapter of the dissertation beginning with Chapter 2.

Chapter 2 addresses the problem of uniformly distributing points on a sphere. A mathematical formulation and a scheme to generate the points problem are presented. In addition, two kinds of methods for observation check are proposed with geographical data applications.

In Chapter 3, the procedure for optimization is studied and applied to a variety of applications in design of satellite constellations. Before optimization process, geometric characteristics of various missions are investigated to select a suitable fitness function. The resulting constellations are explored from a mission performance perspective to make optimality selection.

Chapter 4 introduces the concept of "J_2-propelled" orbits. Analytical derivations are developed to find the conditions for the J_2-propelled orbits. Circular and elliptical orbits are specifically analyzed separately with numerical examples.

Finally, Chapter 5 summarizes all of the findings and conclusions discussed in Chapters 2 through 4.

2. DATABASE PRE-PROCESSING FOR FAST OPTIMIZATION DESIGN

2.1 Introduction

The problem of distributing N points uniformly over the surface of a sphere has been investigated for many decades [17, 18]. This problem is one of the most challenging mathematical problems of the century, known as the 7th Smale's problem [19]. However, because of its implications in many areas of mathematics and its immediate practical applications, it has not only inspired mathematical researchers but also attracted the attention of applied mathematicians in various fields [20]. The capability of uniformly distributing points on a sphere has important theoretical consequences in mathematics and important applications such as survey sampling, dynamic modeling and information storage, and display in engineering, allowing the development of optimal algorithms [21].

Various algorithms have been developed for a small number of points [17, 18, 22]. However, most of them use optimization techniques that are not efficient for a large number of points. Other more modern algorithms, such as Chan's Quadrilateralized Spherical Cube Map (QSCM) projection (1975 Navy report, now out-of-print), extensively analyzed in Ref. [23] and applied by Naval and NASA programs, and the algorithm by Snyder (Ref. 24), which is based on Platonic solids, are efficient and available. These methods all generate a total number of points (N) proportional to the number of faces of a Platonic solid; for instance, six points are generated proportional to the number of faces of Hexahedron for the QSCM. Reference 25 suggested an icosahedron-based method by subsequent quadrisection for evenly spaced binning data. Reference 26 presented a method of constructing equal area triangles by repeatedly applying quadrisection to icosahedron and iterative equalization.

In this of view, subdivision approach is considered to develop algorithm to distribute a large number of points on the sphere. This paper is organized as follows. The first section of this paper examines subdivision approach. Then the original equal area subdivision algorithm and quasi-equal area subdivision algorithms are provided. Finally, applications to geographical data are presented.

2.2 Subdivision Approach

2.2.1 Splitting a Spherical Triangle in Two Equal Area Spherical Triangles

Consider the generic spherical triangle that is formed on the surface of the unit sphere by three great circular arcs intersecting pairwise in three vertices as shown in Fig. 2.1.

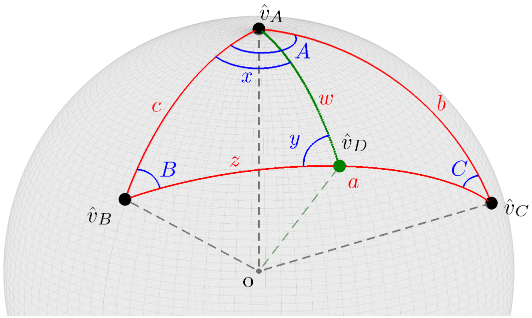

Figure 2.1: Splitting a spherical triangle in two equal area

The area of a spherical triangle $[\hat{\boldsymbol{v}}_A, \hat{\boldsymbol{v}}_B, \hat{\boldsymbol{v}}_C]$ is obtained by

$$S = A + B + C - \pi \tag{2.1}$$

where angles A, B, and C are the dihedral angles of the spherical triangle [in radians] [27]. Incidentally, Eq. (2.1) implies that the sum of the dihedral angles of a spherical triangle must be greater than or equal to π, with equality holding only to the case of a degenerated spherical triangle with zero area.

Let a be the largest side angle, $\hat{\boldsymbol{v}}_C \cdot \hat{\boldsymbol{v}}_B = \cos a$. The problem to solve here is to find the point on the side a such that the two spherical triangles identified by the unit-vectors, $[\hat{\boldsymbol{v}}_A, \hat{\boldsymbol{v}}_C, \hat{\boldsymbol{v}}_D]$ and $[\hat{\boldsymbol{v}}_A, \hat{\boldsymbol{v}}_B, \hat{\boldsymbol{v}}_D]$, have identical areas. Since the unit-vector $\hat{\boldsymbol{v}}_D$ is co-planar to $\hat{\boldsymbol{v}}_C$ and $\hat{\boldsymbol{v}}_D$, it can be linearly expressed by the unit-vectors $\hat{\boldsymbol{v}}_C$ and $\hat{\boldsymbol{v}}_D$ as follows.

$$\hat{\boldsymbol{v}}_D = \frac{1}{\sin a}[\hat{\boldsymbol{v}}_C \sin z + \hat{\boldsymbol{v}}_B \sin(a - z)] \tag{2.2}$$

The area of the spherical triangle $[\hat{\boldsymbol{v}}_A, \hat{\boldsymbol{v}}_C, \hat{\boldsymbol{v}}_D]$ is

$$S_1 = x + y + B - \pi = \frac{S}{2} = \frac{A + B + C - \pi}{2} \tag{2.3}$$

then

$$x + y = \frac{A + C + \pi - B}{2} = D \qquad \text{and} \qquad y = D - x \tag{2.4}$$

Applying the law of cosines to the spherical triangle $[\hat{\boldsymbol{v}}_A, \hat{\boldsymbol{v}}_B, \hat{\boldsymbol{v}}_D]$ gives

$$\cos y = \sin x \sin B \cos c = \cos x \cos B \tag{2.5}$$

Then, using angle difference identity and Eq. (2.4), we obtain

$$\cos D \cos x + \sin D \sin x = \sin x \sin B \cos c - \cos x \cos B \tag{2.6}$$

and

$$\tan x = \frac{\cos D + \cos B}{\sin B \cos c - \sin D}. \tag{2.7}$$

Finally, using the law of sines with the spherical triangle $[\hat{\boldsymbol{v}}_A, \hat{\boldsymbol{v}}_B, \hat{\boldsymbol{v}}_D]$, $\sin z \sin y =$

$\sin c \sin x$, the following solution

$$\sin z = \frac{\sin x \sin c}{\sin(D - x)} \tag{2.8}$$

is obtained. With the knowledge of z (the correct solution satisfies $z < \pi/2$), then it is possible to compute the splitting point, $\hat{\boldsymbol{v}}_D$, using Eq. (2.2).

[21] have introduced the following conjecture to generate uniformly distributed points on a 2-dimensional sphere. This conjecture is based on recursive equal area subdivision of triangles.

Conjecture: *by s recursive splits of an original spherical triangle we obtain a set of* 2^s *non-degenerating spherical triangles with identical areas. As* $s \to \infty$ *centers of the final small spherical triangle identify a distribution of points satisfying Eq.* (2.11) *and Eq.* (2.12) *for the original spherical triangle.*

If this conjecture is correct, then the creation of N asymptotically uniformly distributed points on a sphere depends on how the sphere is split in a spherical triangle.

The idea of splitting spherical polygons to distribute points on a sphere finds the most natural approach (not the most general) by taking advantage from the perfect spherical symmetry provided by Platonic solids. Therefore, subdivision process is started by selecting one of the Platonic solids.

2.2.2 Platonic Solids

Platonic solids are convex regular polyhedra as shown in Fig. 2.2. A polyhedron is said to be regular if its faces and vertex figures are regular polygons. Their faces are identical regular polygons with the same number of faces meeting at each vertex. Five solids exist that satisfy those criteria. Each solid is named according to its number of faces. Interchanging vertices for faces makes the dual of a Platonic solid.

The tetrahedron is the self dual. The hexahedron and octahedron are duals as are the icosahedron and and the dodecahedron.

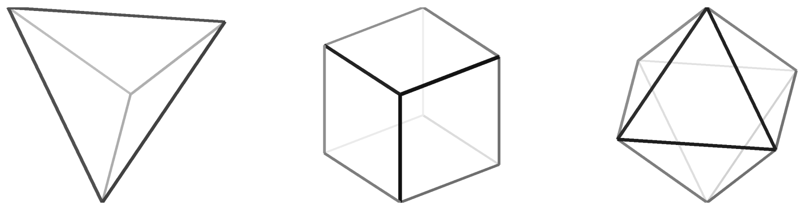

(a) Tetrahedron (b) Hexahedron (c) Octahedron

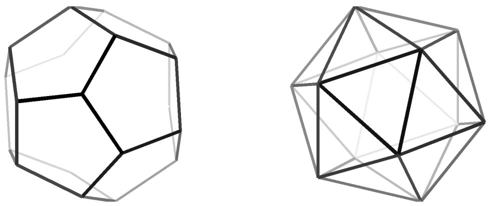

(d) Dodecahedron (e) Icosahedron

Figure 2.2: Platonic solids

The parameters defining the five Platonic solids are summarized in Table 2.1. In this table, v indicates the total number of vertices, e the total number of edges, f the total number of faces, p the number of edges in each face (3 for equilateral triangles, 4 for the squares and 5 for regular pentagons), q the number of edges meeting at each vertex [28], s the type of initial division (3 for trisection 4 for quadrisection and 5 for pentasection), and i the number of initial faces ($i = p\,f$). Since splitting a face into the number of edges with a center of face and vertices generates identical smaller triangles, initial division depends on shape of the face. Note that dual solids have same number of initial faces.

Table 2.1: Platonic solids parameters

Platonic solids	v	e	f	p	q	s	i
Tetrahedron	4	6	4	3	3	3	12
Hexahedron	8	12	6	4	3	4	24
Octahedron	6	12	8	3	4	3	24
Dodecahedron	20	30	12	5	3	5	60
Icosahedron	12	30	20	3	5	3	60

Platonic solids with most initial faces are the icosahedron and dodecahedron as shown in Table 2.1. For this reason, to create a quasi-uniform distribution of points on a sphere we start by splitting the $n = 60$ triangles by equal area. At every split new triangles will be created. In this case the quasi-uniform distribution of points is made with the set of all the centers of triangular faces.

The sides of a Platonic solid can be projected into a sphere where they form arcs. This "Platonic sphere" is the central projection of the sides of the Platonic solid onto the surface of a unit-radius sphere. The projection is on the Platonic solids's circum-sphere, which acts like a curved projection screen [29]. All edges in Platonic solids have been transformed into geodesic arcs in corresponding platonic spheres. In platonic spheres all arcs have same length as well as all edges in Platonic solids. The vertices are nodes in the case of spheres while the vertices are corner in the case of solids.

2.2.3 Icosahedron

The vertices of an icosahedron can be defined using the Golden ratio

$$\varphi = \frac{1+\sqrt{5}}{2} \tag{2.9}$$

The 12 vertices can then be obtained as all even permutations of coordinates as follows

$$\left(0, \pm\frac{1}{\sqrt{1+\varphi^2}}, \pm\frac{\varphi}{\sqrt{1+\varphi^2}}\right) \tag{2.10}$$

An icosahedron has 20 faces, 12 vertices, and 30 edges, as shown in Fig. 2.3a. An icosahedral sphere also has same number of faces, vertices, and edges. However, faces are regular spherical triangles and edges are arc-edges as shown in Fig. 2.3b.

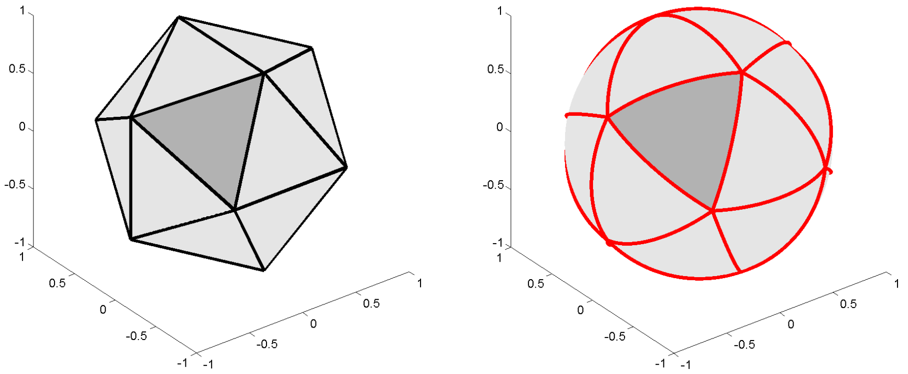

(a) Icosahedron (b) Icosahedral sphere

Figure 2.3: Icosahedron

2.2.4 Subdivision Surfaces

For equal area subdivisions the algorithm must satisfy the following requirements:

(1) every subdivision generates triangles for recursive subdivision, and

(2) the greatest spherical dihedral angle cannot be greater than 90°. This does not allow triangles to degenerate.

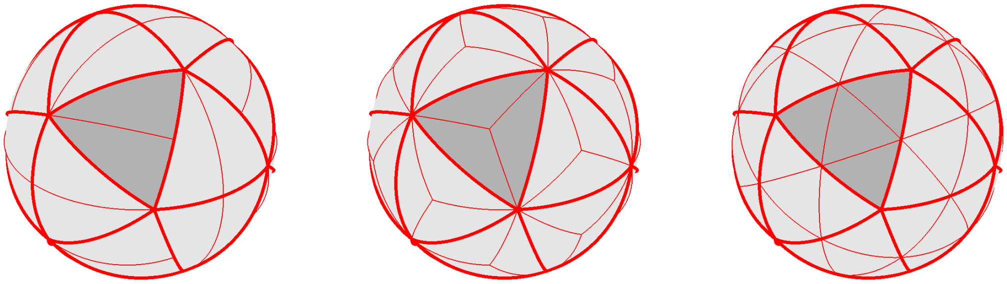

(a) Bisection (b) Trisection (c) Quadrisection

Figure 2.4: Subdivision surfaces

It is possible to use various types of equal area subdivision which preserve area between faces in a planar triangle. However, a few subdivision methods can be applied to a spherical triangle. Figure 2.4a shows the bisection subdivision of spherical triangles. In particular, both planar and spherical faces are shown. In order to keep the sub-triangles as close as possible to the equilateral one, the longest side is selected to split. This avoids the generation of elongated triangles.

Three equal area subdivision (trisection) of spherical triangles can also be performed. For a generic spherical triangle, there is a unique point (direction) where the trisection can be done. The computation of this point/direction requires some effort. Figure 2.4b shows both planar and spherical faces of a trisection subdivision. It is clear that as the subdivisions increase the triangles generated become elongated. This is in contradiction with requirement **(2)**.

Four equal area subdivision (quadrisection) can be obtained by adding a new vertex at the midpoint of each edge of an equilateral triangle and dividing each edge in two. The quadrisection subdivision creates four new triangles in flat faces with equivalent areas (if the original triangle is equilateral). However, projecting these new triangles on the sphere does not provide equivalent spherical areas. Figure 2.4c shows the result of projection on the first level of subdivision. In this figure the dark triangle is quadrisected in four triangles. The internal spherical triangle has a larger area than other adjacent three triangles. This difference then increases with subsequent quadrisections. In addition there is no freedom in choosing the midpoints along the edges for equivalent areas. For the above reasons quadrisection is excluded in potential subdivision candidates.

Ultimately, only one method can be used to recursively subdivide a spherical triangle satisfying requirements **(1)** and **(2)**: *subdivision of spherical triangles in two equal-area spherical triangles by splitting the longest side.*

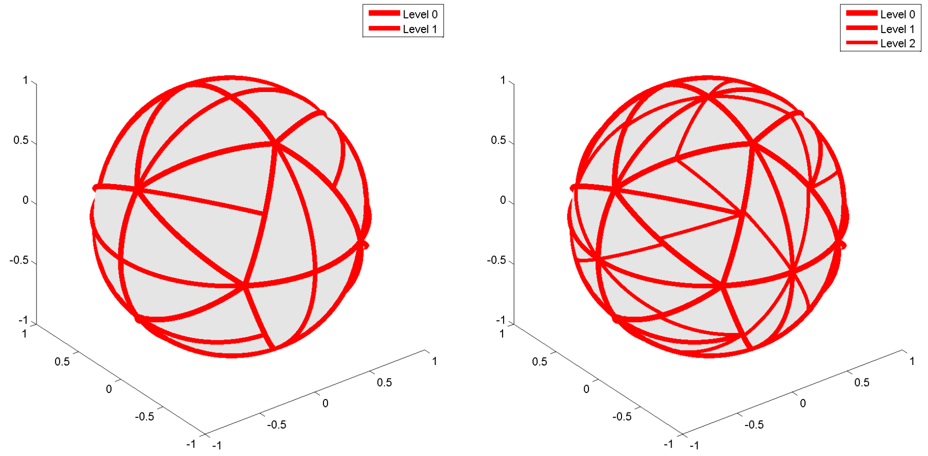

(a) First bisection (b) Second bisection

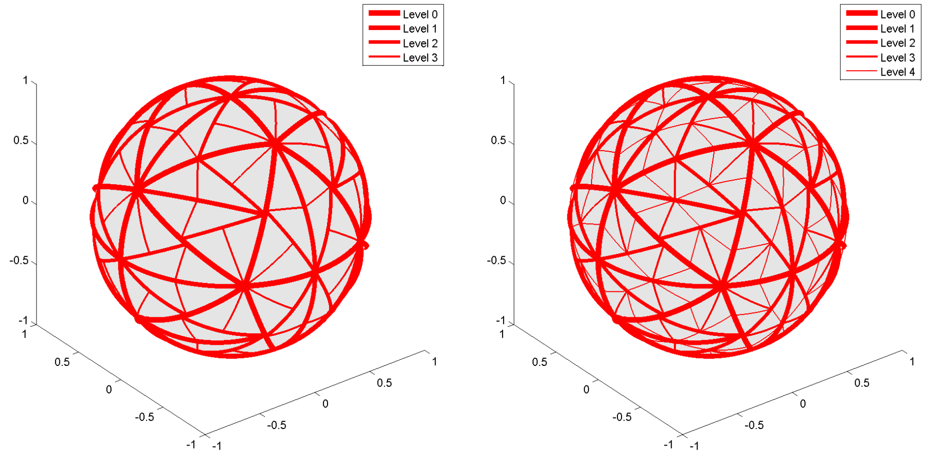

(c) Third bisection (d) Fourth bisection

Figure 2.5: Original equal area subdivision algorithm

Starting with a Platonic solid (e.g., icosahedron) and subsequently performing a set of equal area triangle divisions (as previously described), a final set of small triangles all with the same areas are obtained. The original algorithm [21] considers the directions to centers of these triangles as the set of quasi-uniform directions in space. The number of directions that can be obtained is dependent on the Platonic solid initially considered. For instance, starting from an icosahedron, a total number of $n = 20 \cdot 2^s$ directions can be obtained, where s is the number of subsequent divisions.

This original equal area subdivision algorithm creates quasi-uniform distributed points in space. This procedure is shown in Fig. 2.5. The number of times the equal area subdivision is performed (s) is subsequently referred to as the 'level'. The level 0 corresponds to the initial spherical icosahedron, the level 1 refers to spherical triangles after the first subdivision, and so on. Improvement of this algorithm is described in the next section.

2.4 Quasi-Equal Area Subdivision Algorithm

Quasi-equal area subdivision algorithm scheme comprises of two steps :

1. dividing spherical triangles into equal area spherical triangles subsequently (perform a single equal area trisection, then perform s equal area subdivisions, as previously described), and
2. reshaping the final obtuse triangles after the final even number of divisions.

Note that reshaping (step 2) is applied one time only after all subsequent divisions, because *reshaping does not preserve the area of triangles.*

2.4.1 Step 1: Spherical Triangles Subdivision in Equal-Area Spherical Triangles

This subsequent subdivision consists of one trisection and several bisections. A icosahedron is first subdivided by the equal area trisection. There are now three triangles for each original triangle as shown in Fig. 2.6a. Note that this trisection makes adjacent triangles share common vertices after subdivision. Then, the trisection is followed by s sequential equal area bisections which are identical to subdivisions of the original equal area subdivision algorithm.

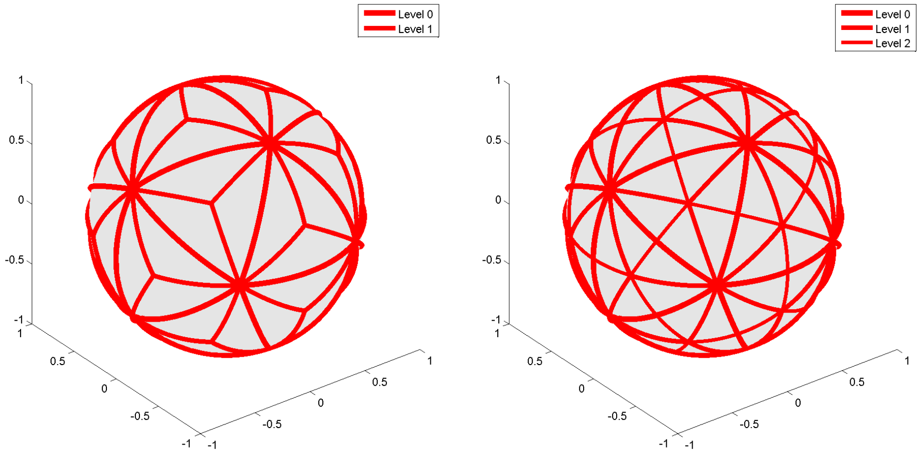

(a) Initial trisection (b) First bisection

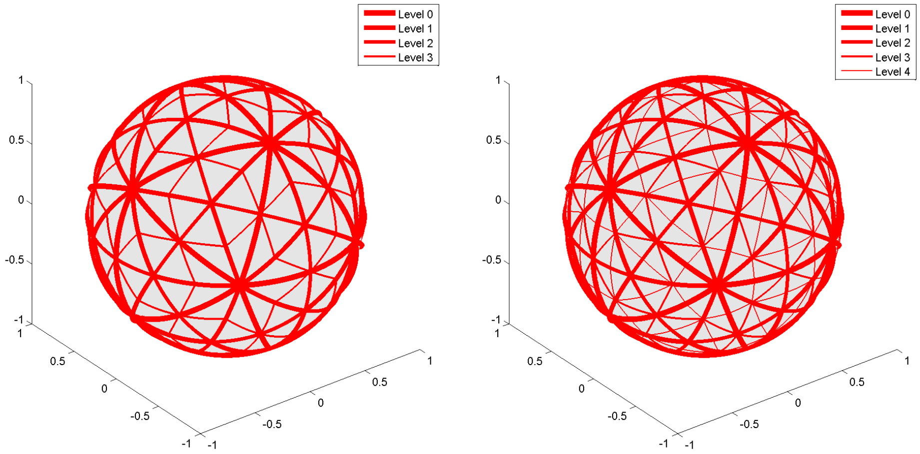

(c) Second bisection (d) Third bisection

Figure 2.6: Step 1: Dividing spherical triangles into equal-area spherical triangles subsequently

The number of vertices and faces of generated triangles in each level is given in Table 2.2.

Table 2.2: Number of vertices and faces of generated triangles in each level

Level	# of vertices	# of faces
0	12	20
1	32	60
2	62	120
3	122	240
4	242	480
5	482	960
6	962	1,920
7	1,922	3,840
8	3,842	7,680
9	7,682	15,360
10	15,362	30,720
11	30,722	61,440
12	61,442	122,880
13	122,882	245,760
14	245762	491520
15	491522	983040

2.4.2 Step 2: Final Reshaping of Obtuse Triangles to Acute Triangles

As shown in Fig. 2.7a and 2.7c, obtuse triangles (dark regions) appear after *even bisections*. The number of obtuse triangles is half the number of total triangles. Since a pair of obtuse triangles exist, they can be reshaped to two acute triangles.

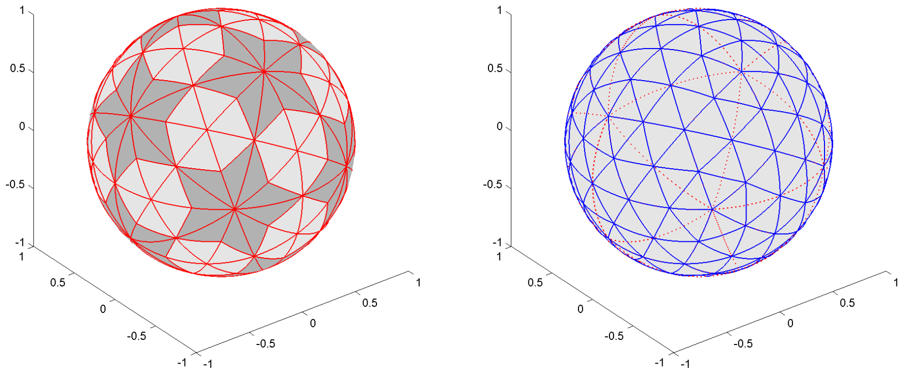

(a) Obtuse triangles after 2 bisections (level 3)

(b) Reshaping after after 2 bisections (level 3)

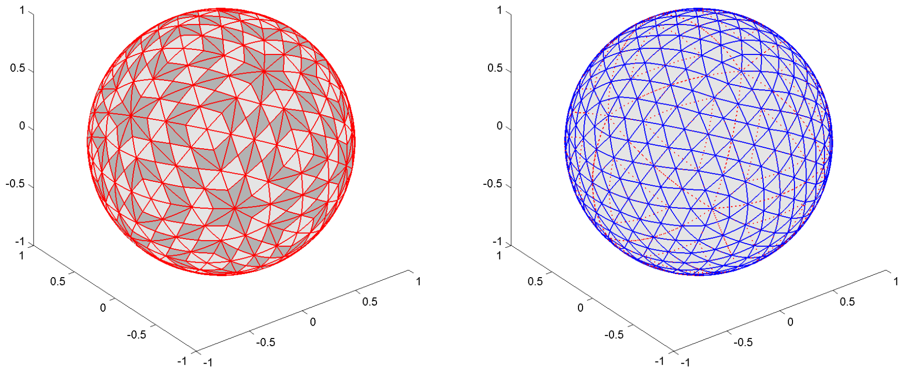

(c) Obtuse triangles after 4 bisections (level 5)

(d) Reshaping after after 4 bisections (level 5)

Figure 2.7: Step 2: Reshaping obtuse triangles to acute triangles

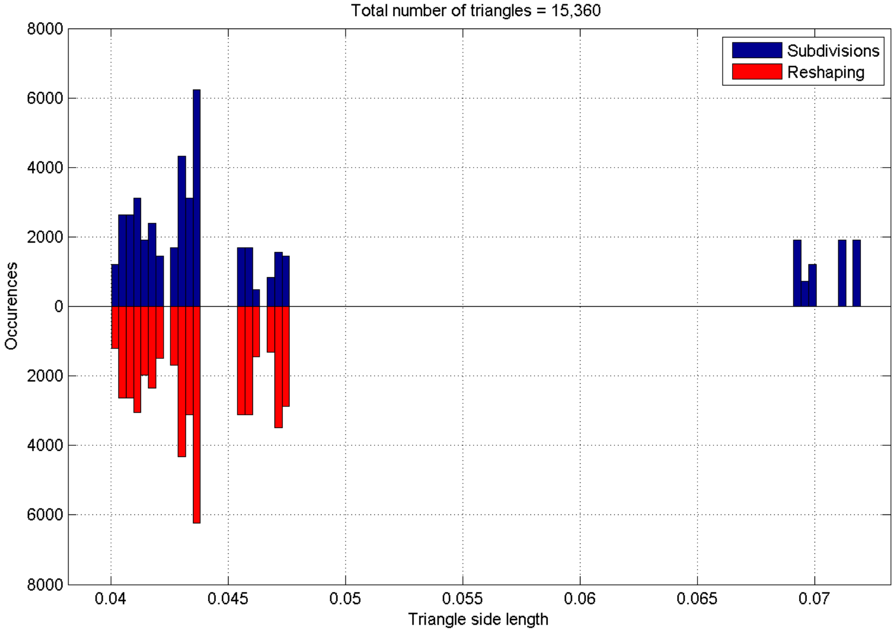

Figure 2.8: Triangles sides length histograms ($s = 9$) with and without reshaping

Figure 2.8 illustrates histograms of the sides' lengths of the final smallest triangles obtained by splitting the icosahedron by $s = 9$ subdivisions. This figure clearly shows that 1) the final resulting triangle sides are bounded, meaning that no degenerated triangle is obtained by recursive application of the splitting algorithm and 2) a smaller bound is obtained by final reshaping (because obtuse triangles disappear after reshaping).

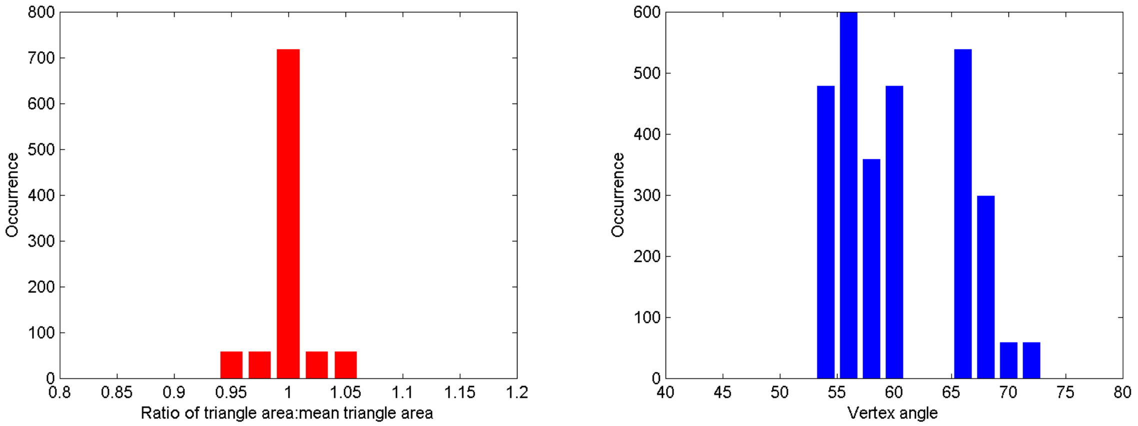

Figure 2.9: Histogram of the ratio of spherical triangle area to mean spherical triangle area and vertex angles in a level 5

Since the final reshaping step changes the area of each reshaped triangle, evaluation for the area preservation is performed with the method by [26]. As shown in the left histogram of Fig. 2.9, all areas of the spherical triangles are within ±5% of the average area. The right histogram clearly shows that the spherical triangle vertex angles are bounded in a small range. Assuming that area with in ±2.5% of the mean area is preserved area, there are 75% of preserved area of spherical triangles in level 5 as illustrated in Fig. 2.10. At higher levels more spherical triangles can be area preserved.

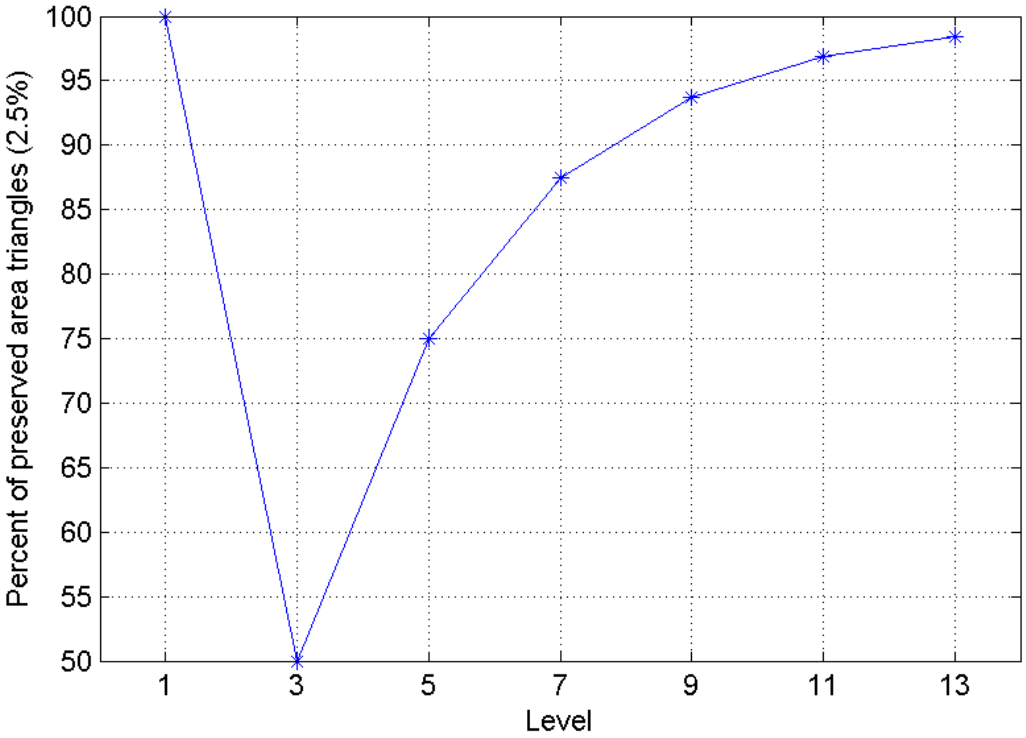

Figure 2.10: Percent of preserved area spherical triangles (within 2.5% of the average area) in each level

Compared to the triangles by method of Ref. 25, this algorithm has the advantage of having triangles of the quasi-equal area. In addition, it doesn't require equalization process in method of Ref. 26.

2.4.3 Construction of Quasi-Uniform Points

[21] suggested taking centers of the triangles as the quasi-uniform points since some of generated triangles are obtuse triangles while [25] and [26] considered vertices of the triangular mesh. Since quasi-equal area subdivision algorithm with even number of bisections provides all acute triangles, vertices of triangles can be consid-

ered to construct quasi-uniform points. Extensive numerical tests have shown that the selection of vertices is a better choice.

Visual results of the original algorithm [21], Fig. 2.11a, and the proposed improvements, Figs. 2.11b and 2.11c, are provided.

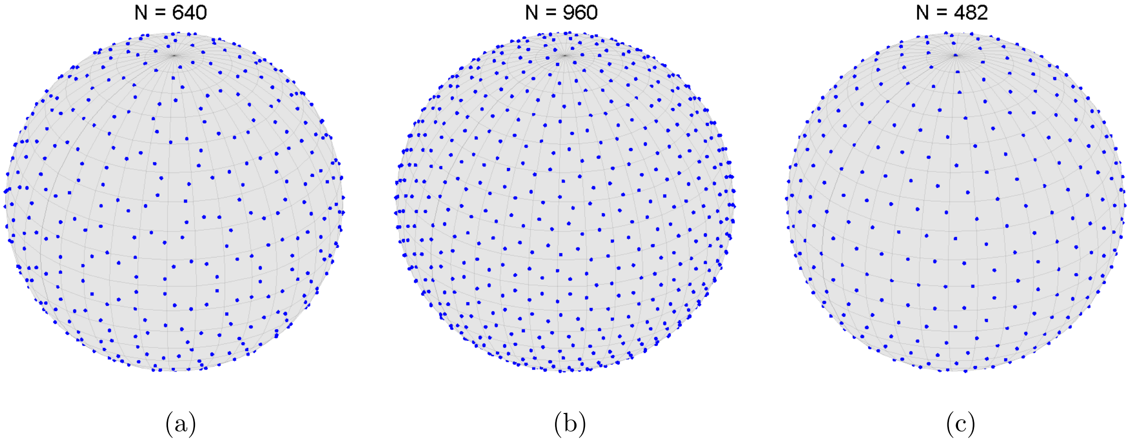

(a) (b) (c)

Figure 2.11: Visual results of various algorithms (level 5). (a) Original equal area subdivision algorithm with centers of the triangles. (b) Quasi-equal area subdivision algorithm with centers of the triangles. (c) Quasi-equal area subdivision algorithm with vertices.

2.4.4 Smale's Validation

The problem of uniform distribution of points on the sphere emerged from complexity theory in a paper by Smale and Shub [30]. Smale himself provided a mathematical tool to quantify the uniform distribution of points on a sphere. For any given distribution of points (unit-vectors), $\hat{\boldsymbol{x}}_1, \cdots, \hat{\boldsymbol{x}}_N \in \mathbb{S}$, it is possible to evaluate the function V

$$V = \sum_{1 \le i < j \le N} \log \frac{1}{\|\hat{\boldsymbol{x}}_i - \hat{\boldsymbol{x}}_j\|} \tag{2.11}$$

Let $V_{\min}$ be the minimum possible value of V. The problem asks for an algorithm that, for an assigned value of N, finds a sequence of points $\hat{\boldsymbol{x}}_1, \cdots, \hat{\boldsymbol{x}}_N$ on the unit sphere such that

$$0 < V - V_{\min} \le c \log N \tag{2.12}$$

where c is a positive constant that depends only on the algorithm provided. Rakhmanov, Saff, and Zhou [31] provide numerical evidence that their generalized spiral points algorithm supports Eq. (2.12) for $N \le 12,000$, with $c = 114$.

Smale provided [19] the following approximated (truncated) formula to evaluate $V_{\min}$

$$\tilde{V}_{\min} = -\frac{1}{4} \log\left(\frac{4}{e}\right) N^2 - \frac{1}{4} N \log(N) + O(N) \tag{2.13}$$

Equation (2.11) through Eq. (2.13) will be used to compare and quantify the uniformity of points distributions as generated by different algorithms.

The approach to measure uniformity of a set directions generated by an algorithm is to evaluate the difference between the value of V for the points obtained, as provided by Eq. (2.11), and the optimal value of $\tilde{V}_{\min}$, as evaluated by Eq. (2.13). This approach is suggested by Smale [19]. The comparison results are shown in Fig. 2.12. Note that the algorithm using vertices with even number of bisections provides best performance since even number of bisections make generated triangles almost equilateral triangles as illustrated in Fig. 2.7.

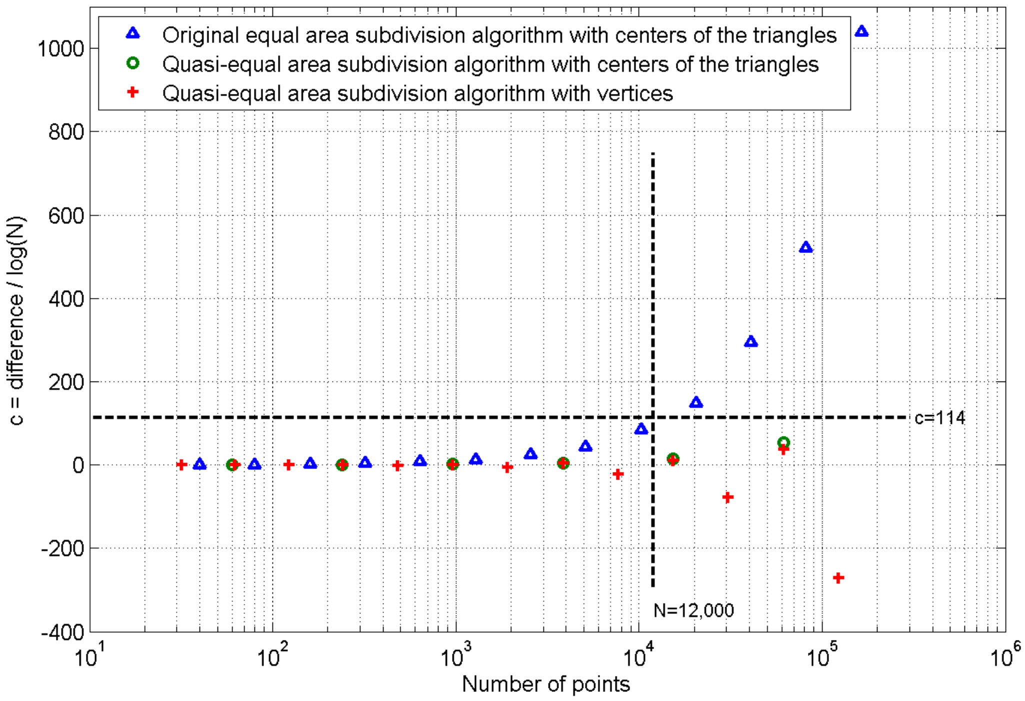

Figure 2.12: Comparison of V_N

2.5 Applications to Geographical Data

Various kinds of geographical grid data sets are used in many fields such as, scientific, economic, politic, etc. For example, Gross National Product (GNP) and a worldwide population distribution map are used to estimate market demand for satellite [32]. In the case of a global mission, the fitness function for a constellations design is computed in globally distributed points [33] and [12]. Most of grid data sets are provided with a fixed step in latitude and longitude. Therefore, conventionally computed points [25] are distributed with a fixed step in latitude and longitude as shown in Fig. 2.13a. Since this is certainly not a uniform distribution of points on the Earth, mainly due to the increase of point density at high latitude regions as illustrated in Fig. 2.13b, the need to convert these data into an "equivalent" distribution of points (with different weights) is needed. This will dramatically decrease to small amount data sets with appropriate values. Consequently, computational burden is then reduced using "equivalent" uniformly distributed points.

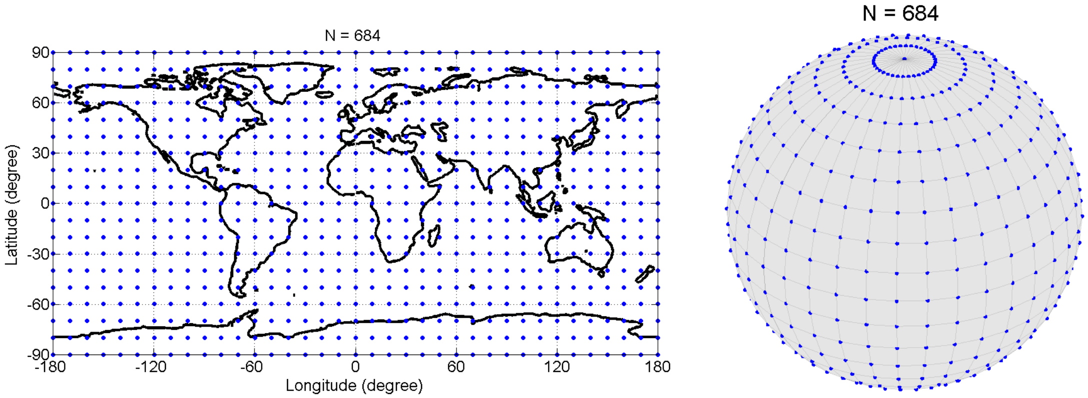

(a) (b)

Figure 2.13: Conventional scheme to distribute points (10 degree resolution, 684 points)

The following subsections show how to determine which data points are observed. [25] suggested overlapped pentagonal and hexagonal bins. In this research, triangular and aperture cones methods have been used since suggested algorithms provide equivalent areas.

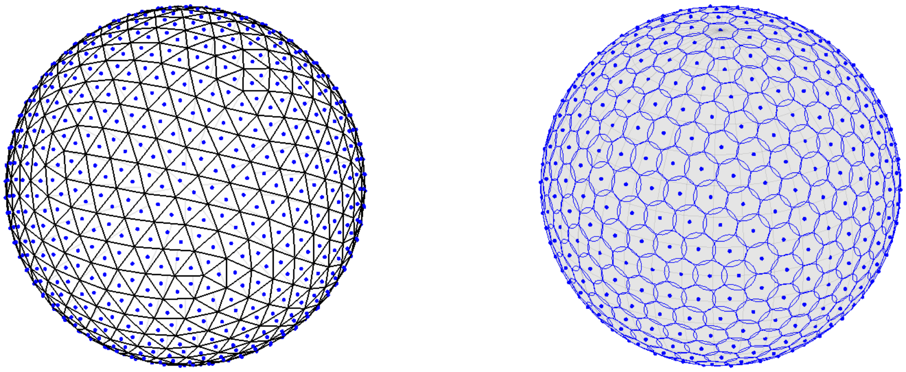
(a) (b)

Figure 2.14: Triangular and aperture cones for binning of data

2.5.1 Observation Check for Geographical Data

2.5.1.1 Triangular Method

One method to convert this geographical data set into equivalent quasi-uniform data set is using triangles. Many equal area triangles are provided by equal area spherical subdivision algorithms. Therefore, checking if geographical data points are inside or outside a triangle can determine if points are observed or not. Figure 3.12 shows the geometry of observation and non-observation cases. In the case of observation (left), the sum of the areas of the three sub-triangles is equal to the area of the original triangle while the non-observation case (right) is experienced if the total area is greater than the area of the original triangle.

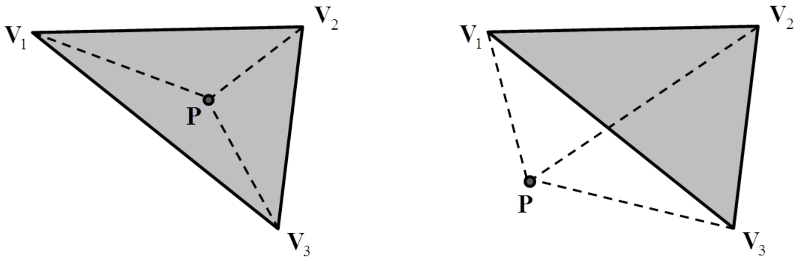

Figure 2.15: Geometry of observation and non-observation cases

In order to check observation condition, all uniformly distributed points are transformed to topocentric-horizon coordinate system with mid-point of triangle as origin, and then projected to surface as all points of quadrilateral are transformed. Equation to check whether the point $\boldsymbol{P}_v$ is observed is given by Ref. [34].

$$A(\boldsymbol{P}\boldsymbol{V}_1\boldsymbol{V}_2) + A(\boldsymbol{P}\boldsymbol{V}_2\boldsymbol{V}_3) + A(\boldsymbol{P}\boldsymbol{V}_3\boldsymbol{V}_1) = A(\boldsymbol{V}_1\boldsymbol{V}_2\boldsymbol{V}_3) \tag{2.14}$$

2.5.1.2 Aperture Cones Method

Triangular method can be applied to only algorithms using center of triangles. Therefore, a different method is required in order to use algorithm with vertices which provide best performance. This is aperture cones method which is explained in previous section, and it can be used for all algorithms since distributed points are required for this method. The following two subsections which show two examples for geographical data application demonstrate observation check methods together.

2.5.2 Example 1: Building a Uniform Sampled Data with Regional Grid Data

The first example is a case with regional grid data. The Nitrogen Fertilizer Application data set of the Global Fertilizer and Manure, Version 1 Data Collection represents the amount of nitrogen fertilizer nutrients applied to croplands. The data were compiled by Potter et al. [35] and are distributed by the Columbia University Center for International Earth Science Information Network (CIESIN). Data are provided at 0.5 deg resolution in latitude by longitude.

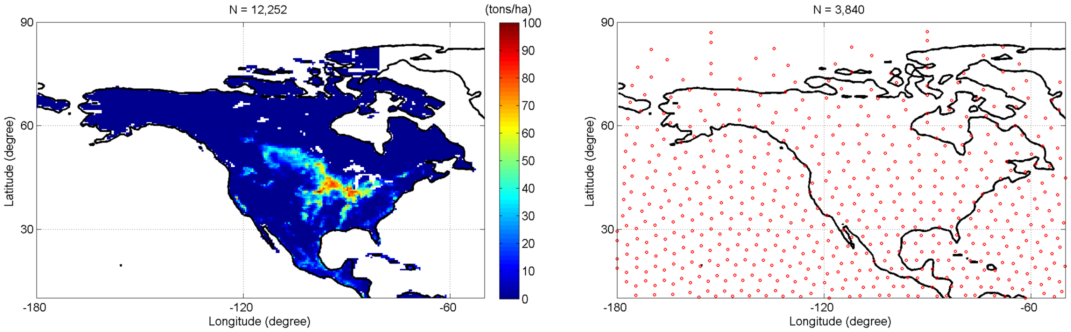

(a) Nitrogen fertilizer application (0.5 degrees resolution): 12,252 points

(b) Uniformly distributed points: 3,840 user points

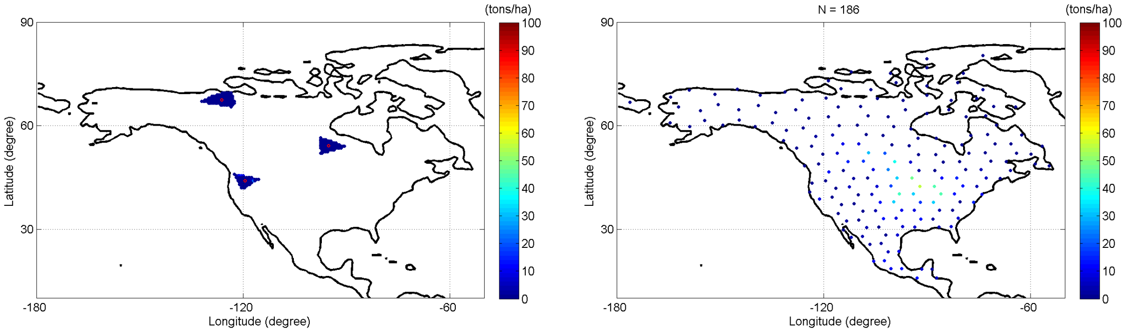

(c) Observed data for specific points (Triangular method)

(d) Nitrogen fertilizer application (Uniformly distributed) : 186 points

Figure 2.16: Regional weight point description (varying values)

In this example quasi-area subdivision algorithm with centers of triangles has been applied and triangular method has been used for observation check as shown in Fig. 2.16c. Note that each triangle area is same, but it looks larger near the pole. Compare to Fig.2.16a, final data set is expressed in very small number of points as shown in Fig.2.16d.

2.5.3 Example 2: Building a Uniform Sampled Data with Global Grid Data

The second example is case with global grid data. Gridded Population of the World, Version 3 (GPWv3), Future Estimates consists of estimates of human population for the year 2015 by 0.25 degree grid cells. A proportional allocation gridding algorithm, utilizing more than 300,000 national and sub-national administrative units, is used to assign population values to grid cells. The population density grids are derived by dividing the population count grids by the land area grid and represent persons per square kilometer [36].

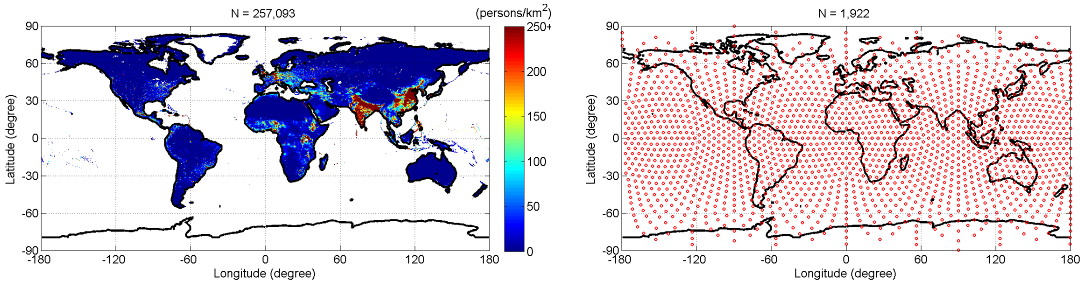

(a) Population density (0.25 degrees resolution): 257,093 points

(b) Uniformly distributed points: 1,922 user points

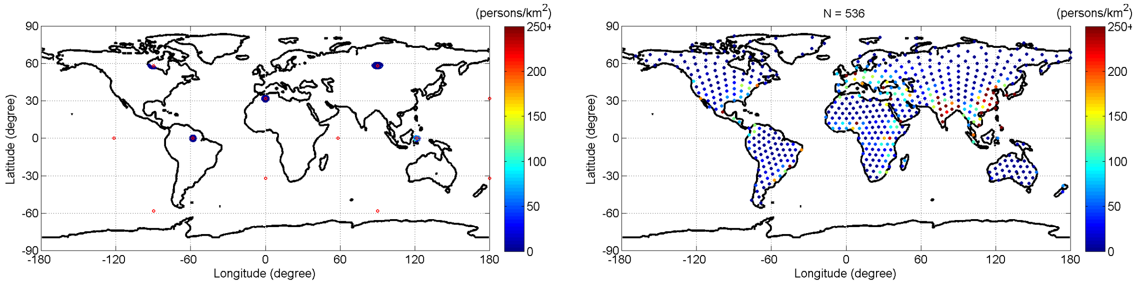

(c) Observed data for specific points (Aperture cones method)

(d) Population density (Uniformly distributed) : 536 points

Figure 2.17: Global weight point description (varying values)

Quasi-area subdivision algorithm with has been used in this example. Therefore aperture cones method has been used for observation check as illustrated in Fig. 2.17c. Finally $257,093$ geographical points in Fig.2.17a are reduced to 536 points as illustrated in Fig.2.17d.

2.6 Conclusions

This paper provides quasi-equal area subdivision algorithm based on equal area spherical subdivision to obtain uniform distribution of points on a sphere. The algorithm adopts the theory of the original equal area subdivision algorithm, which is to perform subsequent bisections of spherical triangles. By subsequent subdivisions the whole sphere which is made of N equal area spherical triangles can be obtained. As the number of divisions increases, the center of these spherical N triangles well approximates uniform distribution of N points on a 2-dimensional sphere. The main feature of the proposed algorithm is to share common vertices between adjacent triangles. This is accomplished by initial division allows generated triangles to be deployed symmetrically. Therefore, reshaping can be applied to triangles, and vertices can be used for uniform points. It has been found that the proposed quasi-equal area subdivision algorithm provides good performance with validation.

After generating uniformly distributed points, two methods for observation check have been proposed. These observation check methods have been used successfully in two examples which demonstrate geographical data applications. These examples also demonstrate that suggested algorithms decrease huge numbers of geographical data sets to smaller amounts in order to reduce computational burden.

3. LATTICE FLOWER CONSTELLATION OPTIMIZATION*

3.1 Constellation Design Considerations

3.1.1 Genetic Algorithms

Genetic Algorithms, which were invented by John Holland, his colleagues, and students at the University of Michigan in the mid-1970s, are adaptive heuristic search algorithms that mimic the natural selection/mutation process[37]. These are actually search processes and useful method for finding optimum solutions[38]. Although there is no guarantee that Genetic Algorithms will provide optimum solutions (and this is true for most optimization methods), Genetic Algorithms are most appropriated in highly nonlinear multi-parameter problems[39]. Since constellation design is a highly nonlinear problem, Genetic Algorithms have been chosen to discover the optimum parameters for constellation.

The outline of Genetic Algorithms is as follows:

1. Start: Generate random population of N chromosomes
2. Fitness: Evaluate the fitness function for each chromosome x in the population
3. Selection: Select the parents according to their fitness to generate the new population
4. Crossover: Combine genes of parents to form the offspring. If no crossover was performed, offspring is an exact copy of parents
5. Mutation: With a mutation probability mutate new offspring at each locus
6. Accepting: Place new offspring in the new population

---

*Part of this section is reprinted with permission from "2-D Lattice Flower Constellations for Radio Occultation Missions" by Sanghyun Lee and Daniele Mortari, 2013. *Frontiers in Aerospace Engineering*, Vol.2, Issue.2 (2013), pp. 79–90. Copyright © 2013 by Sanghyun Lee and Daniele Mortari.

7. Loop: Go to Step 2 and repeat until the maximum iterations or minimum error criteria is not attained

For the simulation, the population size is chosen to be 150 and the maximum number of generations as 100. The crossover rate and mutation rate are selected to be 0.6 and 0.2, respectively.

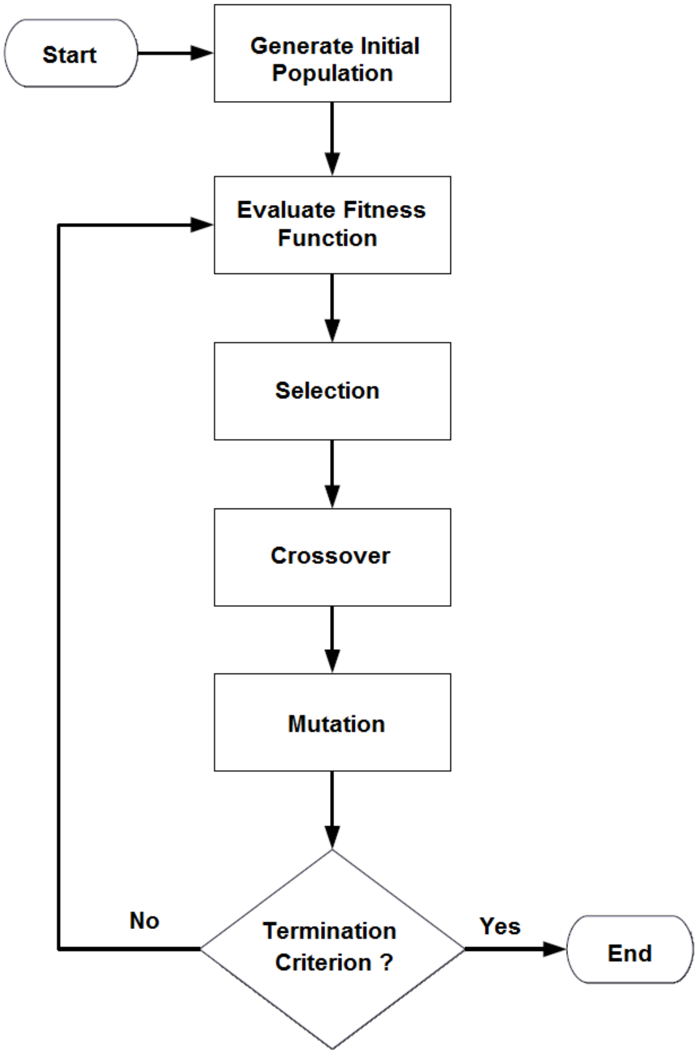

Figure 3.1: Flowchart for a GA implementation

3.1.2 Uniform Distribution of Points on a Sphere

In the case of a global mission, the fitness function for a constellations design is computed in globally distributed points [33, 12]. Most of grid data sets are provided with a fixed step in latitude and longitude. Therefore, conventionally computed points are distributed with a fixed step in latitude and longitude [25]. Since this is certainly not a uniform distribution of points on the Earth, mainly due to the increase of point density at high latitude regions as illustrated in Fig. 3.2a, uniform distribution of points on a sphere is required. This will dramatically decrease to small amount data sets and computational burden is then reduced. The creation of uniform distribution of points is generated by modification of the method presented in Ref. [40]. The algorithm start by applying cuts with an icosahedron (20 identical equilateral triangular faces) and performing 1 trisection and then 5 sequential bisections in identical spherical triangles, $20 \cdot 3 \cdot 2^4 = 960$ triangles with quasi-identical spherical areas are obtained whose vertices approximate 482 uniformly distributed points on a sphere. Before performing trisection, the initial icosahedron is rotated around specific axis, $[1, \quad 1, \quad 0]^{\mathrm{T}}$ by 30° in order to avoid final distributed points having latitudinal and longitudinal symmetry.

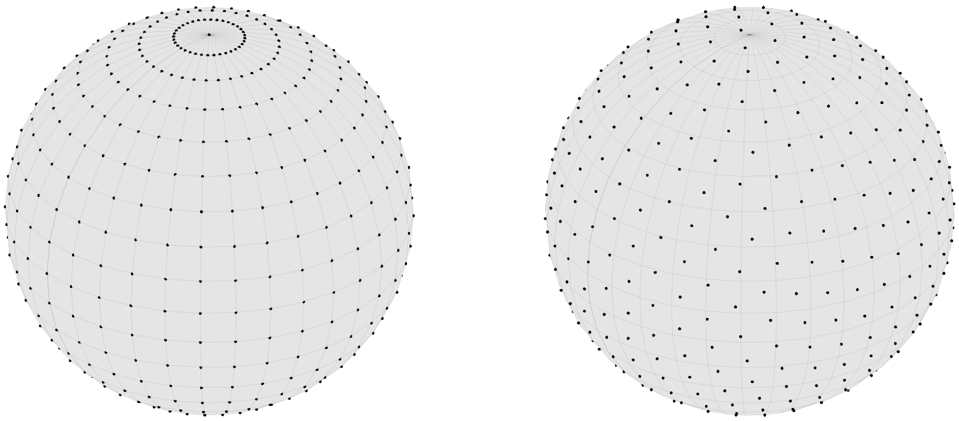

(a) Gridded distributed points (10 degree resolution, 684 points)

(b) Uniformly distributed points (482 points)

Figure 3.2: Distributed points on a sphere

3.1.3 Fitness Function with Weight

As constellation design using Genetic Algorithms, defining a fitness function to drive the optimization process is the key issue. Therefore, the fitness function should be defined In the mathematical expression of the fitness function the parameters to be optimized are calculated in a set of N_t times N_x user grid points distributed on the Earth surface. This formula allows us to control the fitness function by giving more weight to interested user grid points. In this research, 3 different types of weight are used for interested regions. Interested areas and corresponding weight are as follows:

1. global : locationally fixed weight,
2. technographic : locationally fixed value weight in specific area, and
3. demographical : locationally varying weight (global population density), and
4. economic : locationally varying weight (gross domestic product) in land area.

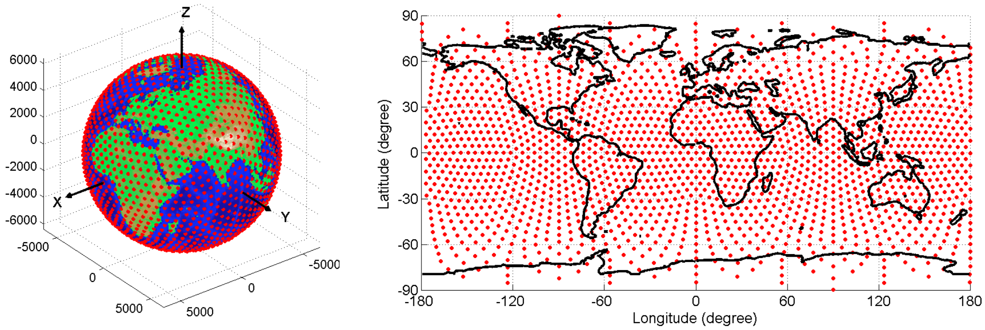

(a) (b)

Figure 3.3: Global weight point description (fixed values) : 1,922 user points

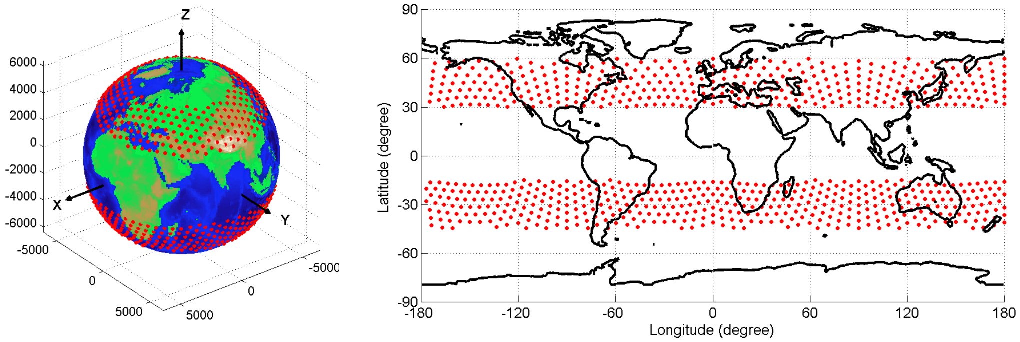

(a) (b)

Figure 3.4: Technographic weight point description (fixed values): 531 user points

Gridded Population of the World, Version 3 (GPWv3) consists of estimates of human population for the years 2000 by 2.5 arc-minute grid cells and associated data sets dated circa 2000. A proportional allocation gridding algorithm, utilizing more than 300,000 national and sub-national administrative units, is used to assign population values to grid cells. The population density grids are derived by dividing the population count grids by the land area grid and represent persons per square kilometer. [41]

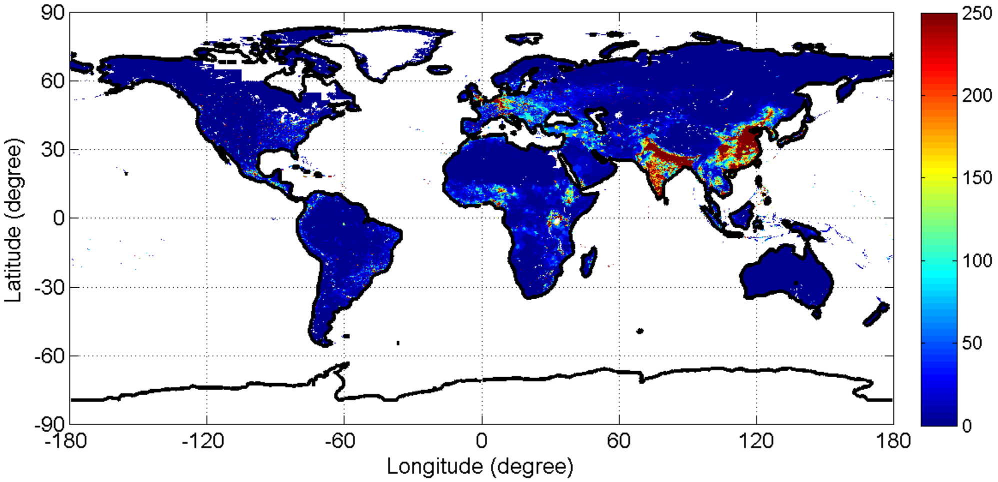

(a) Population density (2.5 arc-minutes resolution): 29,652,480 user points

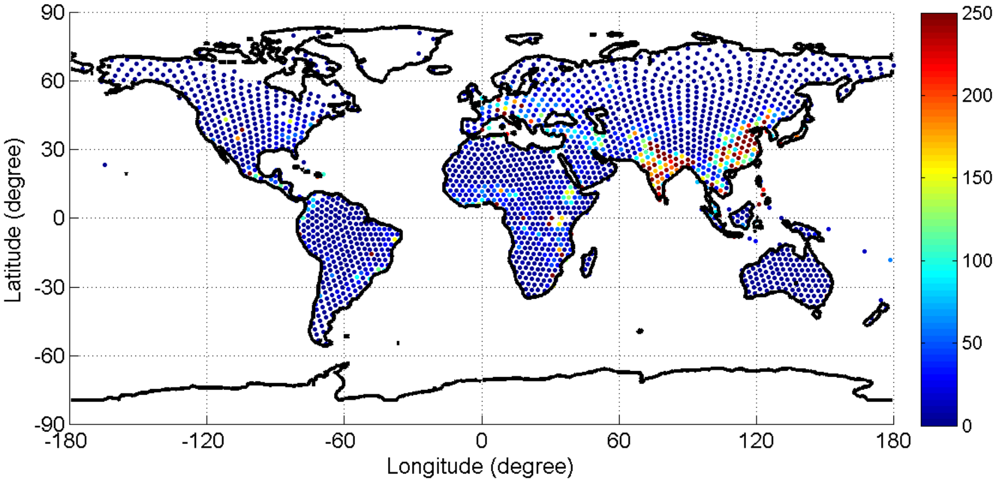

(b) Population density (Uniformly distributed) : 1,983 user points

Figure 3.5: Demographic weight point description (varying values)

Gridded country-level GDP of the World, based on the SRES B2 Scenario, consists of estimates of global domestic product for the years 2025 by 0.25 degree grid cells. Gross Domestic Product (GDP) per unit area in millions of US dollars is derived from the IPCC Emission Scenario data. [42]

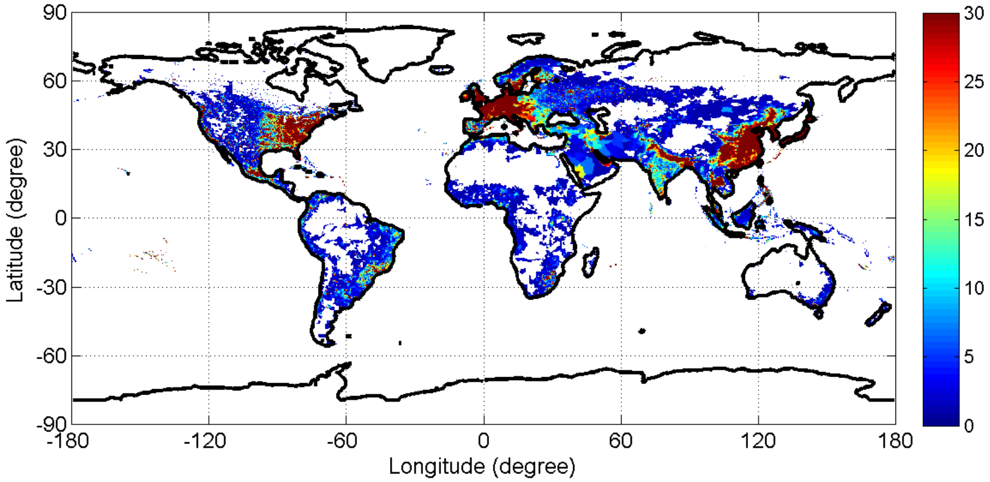

(a) Gross domestic product density (0.25 degree resolution)

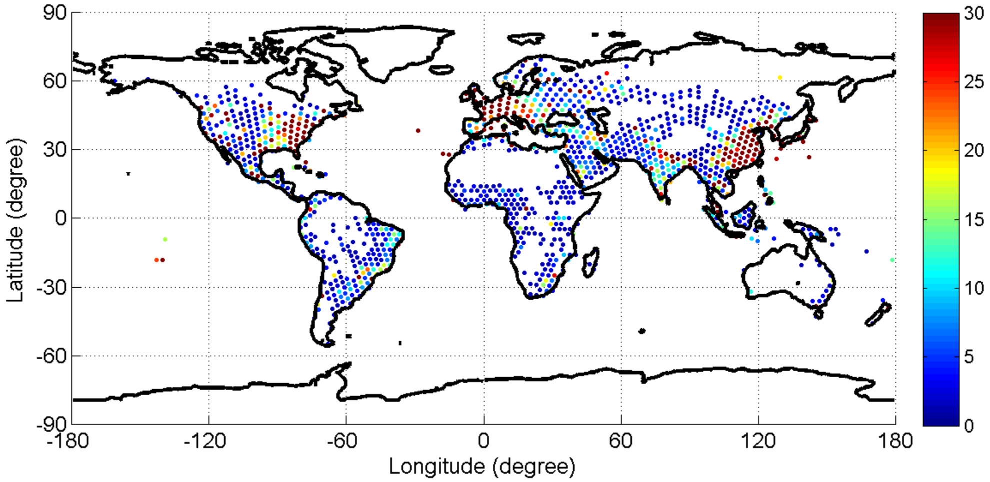

(b) Gross domestic product density (Uniformly distributed) : 1,177 user points

Figure 3.6: Economic weight point description (varying values)

3.1.4 Design Parameters Ranges for Low Earth Orbits

In order to run the optimization process, the design parameters space should be first defined. Acceptable orbit radius for low earth orbit should be bounded by the maximum atmosphere altitude and the inner Van Allen radiation belt. Considering lower boundary of the inner Van Allen Radiation belt, the maximum altitude is set to $h_{\max} = 1,500$ km [43]. The minimum altitude is set to $h_{\min} = 300$ km because that would be impractical due to the larger atmospheric drag[44]. Using these two altitude constraints the maximum and minimum periods are $T_{\min} = 2\pi\sqrt{\dfrac{(R_\oplus + h_{\min})^3}{\mu}}$ and $T_{\max} = 2\pi\sqrt{\dfrac{(R_\oplus + h_{\max})^3}{\mu}}$, where $R_\oplus$ is the Earth's radius.

3.1.5 Minimum Distance Constraint for Collision Avoidance

To avoid the design of constellations with satellites colliding the results provided by Ref. [45] is adopted. In that analytical study, the closest approach between the two satellites ($\rho_{\min}$) in two circular orbits with the same radius and inclination, is analytically expressed by the following equation

$$\rho_{\min} = 2\left|\sqrt{\frac{1+\cos^2 i + \sin^2 i\,\cos\Delta\Omega}{2}}\,\sin\left(\frac{\Delta F}{2}\right)\right| \tag{3.1}$$

where

$$\Delta F = \Delta M - 2\tan^{-1}\left[-\cos i\,\tan\left(\frac{\Delta\Omega}{2}\right)\right]$$

and where ΔM and $\Delta\Omega$ are the differences in mean anomaly and right ascension of ascending node, respectively. Note that $\rho_{\min}$ must be scaled by the orbit radius to find the actual value of the minimum approach distance. Due to the regular pattern (lattice) of the LFC, it is not necessary to evaluate the minimum distance using all pairs of satellites. It is sufficient to evaluate the minimum distance between the first satellite $[\Omega_{11}, M_{11},]$ with all the other satellites staying on different orbital planes. This greatly simplifies the effort in the optimization to avoid constellations affected by satellite conjunctions (sometime common for symmetric distribution). Constraint that no two satellites are ever closer than half the distance between two consecutive satellites in the same orbit has been used. For the specific case of $N_{so} = 1$ (just one satellite per orbit), the constraint adopted is that the minimum distance between any pair of satellites is greater than ten percent of optimal distance of constellation. N_s satellites are equally spaced if

$$S = \frac{4\pi}{N_s} = 2\pi(1 - \cos\theta) \tag{3.2}$$

Therefore, the optimal distance of constellation is obtained by

$$\rho_{opt} = 2R\sin\theta \tag{3.3}$$

where R is orbit radius and θ is the Earth central angle.

3.2 2-D Lattice Flower Constellations for Radio Occultation Missions

3.2.1 Introduction

Radio Occultation (RO) is a recently proposed remote sensing technique to measure, in real time, physical parameters of the atmosphere, such as density and water vapor. The technique requires at least two satellites, one transmitting an electromagnetic signal and the other receiving it. The signal arrives to the receiver refracted as it travels through the atmosphere, and the refraction magnitude is a function of the density and water vapor. Detailed information on radio occultation can be found in Ref. [46]. Since the GPS satellites already provide this electromagnetic (radio) signal, techniques known as GPSRO are proposed for LEO satellites [47, 48]. For GPSRO missions the signal bending (due to the atmosphere refraction) is measured by detecting Doppler shift. In particular, it is possible to retrieve information on temperature and pressure using an Abel transform [49] for atmosphere altitudes below the ionosphere.

The name, *radio occultation*, comes from the chance for two satellites to see each other just before they are *occulted* by the Earth during the relative orbital motion. In that short time, when they can see each other through the atmosphere, the electromagnetic signal is sent and the radio occultation measurement can be performed. In general, for two satellites having different orbital periods, the RO measurement time happens only once per orbit. In this paper, we propose three different satellite constellations where a subset of satellite pairs sees each other for almost all the orbital period. In particular, these constellations, which are using circular orbits only, are analyzed and compared in term of *atmosphere coverage* by considering no atmospheric refraction. When considering the actual atmospheric refraction, the radius of the optimal orbit is slightly changed but the atmospheric coverage remains substantially identical.

When a radio signal from a transmitter passes through the atmosphere its phase is perturbed in a way related to the atmospheric refractivity along the electromagnetic signal path. In general, the refraction angle is obtained by phase measurements from a receiver. Then, atmospheric quantities such as density, temperature, pressure, and moisture can be derived from it.

Radio Occultation missions can be classified in the following three categories:

1. two (or more) satellites on the same orbit (forming "string-of-pearls"),
2. geostationary satellites with Low Earth Orbit (LEO) satellites, and
3. Global Navigation Satellite System (GNSS) with LEO satellites [50].

The first RO experiment was performed during the occultation of the Mariner V spacecraft by Venus on 19 October 1967 after theoretical studies [51, 52]. RO investigation using geostationary satellite with LEO satellite was made by radio link between two satellites in 1974 [53]. The first was the Applications Technology Satellite (ATS-6) and the second was Geodetic Earth Orbiting Satellite (GEOS-3). Because these approaches provide limited data, many satellites are required for Earth's atmosphere global coverage, leading to unaffordable costs. This situation changed when Global Positioning System (GPS) signals were proposed of being used for RO. The RO technique has been applied to GPS signals as observed by LEO satellites in order to monitor the Earth's atmosphere with acceptable costs. The first experiment of GNSS-LEO was the GPS/MET (METeorology) experiment using the Microlab-1 satellite in 1995 [54, 47]. Then, several other RO experiments have been conducted using GPS signals, notably CHAMP (CHAllenging Minisatellite Payload), GRACE (Gravity Recovery And Climate Experiment), and the FORMOSAT-3/COSMIC (Constellation Observing System for Meteorology, Ionosphere, and Climate) constellation [55, 56]. Also, several RO missions using GNSS-LEO technique have been designed for the Russian GLONASS and the European Galileo constellations. With the advent of more efficient technologies, the use of cost-effective small satellites allows LEO-to-LEO links to provide global coverage with acceptable mission costs.

Optimal constellation design is a difficult problem because of the high dimensionality of the problem as each orbit depends of six parameters. However, it is possible to design different configurations of LEO satellites (LEO constellations) able to obtain high RO active times and global coverage. The optimal design of such constellations can be done using existing, well-proven, satellite constellation frameworks (e.g., Streets-of-coverage [6, 7] and Walker's [8, 9]) as well as the recently proposed 2-D Lattice Flower Constellations (LFC) [11]. The goal is to obtain a reasonable reduced problem dimensionality without cutting out potential useful solutions. This research study shows how to derive these parameters in order to maximize the atmosphere coverage. Reasonable initial radius ranges can be obtained by limiting the atmospheric drag and by avoiding the inner Van Allen belt.

This section is organized as follows. The first part briefly describes the radio occultation mission. Then, we then discuss design considerations and parameters for 2-D LFC and optimize the design of the constellations. Finally, the performance of three selected constellations for radio occultation mission are presented.

3.2.2 Radio Occultation Mission

3.2.2.1 Mission Needs

The fitness function defining the optimal RO constellation for global coverage of the Earth's atmosphere requires to maximize the occurrences that pairs of satellites can see each other through the atmosphere (active or observation time). Next section defines the basic geometry of two satellites during the RO active time.

3.2.2.2 Geometry of Radio Occultation

The simplest optimal RO constellation is made of satellites on the same circular orbit of radius R. Figure 3.7 shows how the maximum central angle ($\alpha_{\max}$) between two satellites for RO mission depends on the minimum atmosphere radius ($R_{\min}$) while minimum central angle ($\alpha_{\min}$) depends on maximum atmosphere radius ($R_{\max}$). In this study we consider the atmosphere altitude ranging from 20 km to 200 km. Two satellites on the same circular orbit see each other through atmosphere if

$$\cos\alpha_{\max} \leq \frac{\boldsymbol{R}_i \cdot \boldsymbol{R}_j}{R^2} \leq \cos\alpha_{\min} \tag{3.4}$$

where $\alpha_{\max} = 2\cos^{-1}\left(\frac{R_{\min}}{R}\right)$, $\alpha_{\min} = 2\cos^{-1}\left(\frac{R_{\max}}{R}\right)$, and where $\boldsymbol{R}_i$ and $\boldsymbol{R}_j$ are the position vectors of the i-th and the j-th satellite, respectively.

3.2.3 Atmosphere Coverage

3.2.3.1 Linear Swath Geometry of Two Satellites at a Specific Time

Linear swath between two satellites at a given instant time is as shown in Fig. 3.8. The satellites are located at orbital positions $\boldsymbol{S}_i$ and $\boldsymbol{S}_j$, while the Earth's center is indicated by the point $\boldsymbol{O}$. The distance between the two satellites is L and the angles α and α^* are the central angles $\angle\boldsymbol{S}_i\mathbf{O}\mathbf{S}_j$ and $\angle\boldsymbol{S}_i^*\mathbf{O}\mathbf{S}_j^*$, respectively.

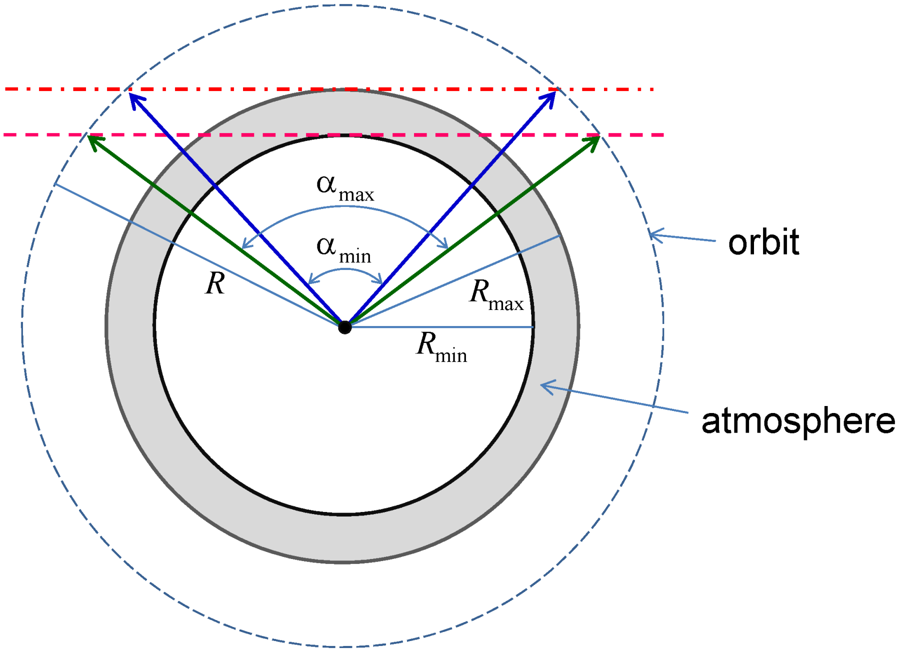

Figure 3.7: Two satellite geometry during radio occultation active time

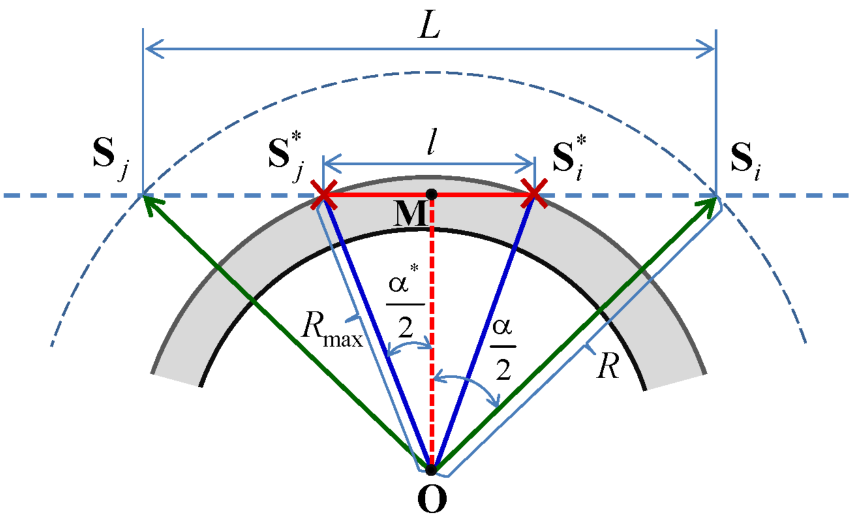

Figure 3.8: Linear swath geometry for two satellites at a given time

To analyze the coverage, let us assume the radio signal is a line segment passing through the atmosphere with no refraction (which is practically very small). The end points of this segment are indicated by $\boldsymbol{S}_i^*$ and $\boldsymbol{S}_j^*$, respectively. Midpoint of the segment is point $\boldsymbol{M}$. The length l of the linear swath is simply given by

$$l = 2R_{\max} \sin\left(\frac{\alpha^*}{2}\right) = 2R_{\max}\sqrt{1 - \cos^2\left(\frac{\alpha^*}{2}\right)} \tag{3.5}$$

where $R_{\max}$ is maximum atmosphere height. Considering the two triangles, $\triangle\mathbf{OMS}_j^*$ and $\triangle\mathbf{OMS}_i$, we can write

$$\overline{\mathbf{OM}} = R\cos\left(\frac{\alpha}{2}\right) = R_{\max}\cos\left(\frac{\alpha^*}{2}\right) \tag{3.6}$$

Then, using Eq. (3.6), we obtain

$$\begin{aligned} l &= 2R_{\max}\sqrt{1 - \left[\frac{R}{R_{\max}}\cos\left(\frac{\alpha}{2}\right)\right]^2} \\ &= 2\sqrt{R_{\max}^2 - R^2\frac{\cos\alpha + 1}{2}} \end{aligned} \tag{3.7}$$

where R is orbital radius.

3.2.3.2 Planar Swath Geometry of Two Satellites During a Time Interval

Fig. 3.9 shows planar swath geometry for two satellites during a time step $(t_{k+1} - t_k)$. Considering two satellites in time t_k and t_{k+1}, we have 4 position vectors of satellites $[\boldsymbol{S}_i(t_k),\ \boldsymbol{S}_j(t_k),\ \boldsymbol{S}_j(t_{k+1}),\ \boldsymbol{S}_i(t_{k+1})]$.

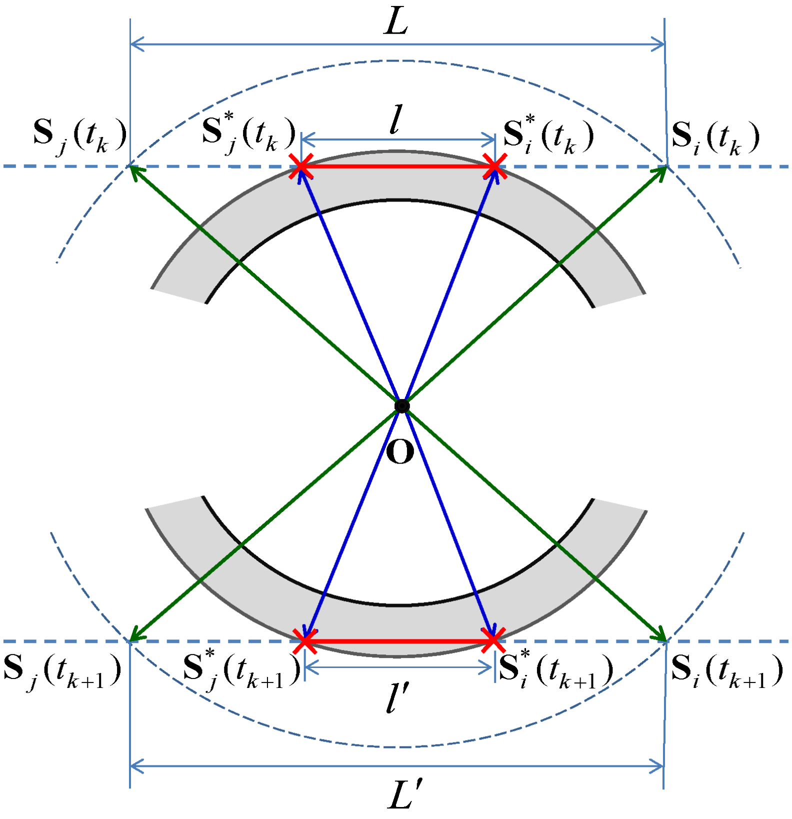

Figure 3.9: Planar swath geometry for two satellites during a time step

These position vectors indicate 4 vertices of planar swath that can be obtained as follows.

$$\begin{aligned}
\boldsymbol{S}_i^*(t_k) &= \boldsymbol{S}_i(t_k) + \frac{\boldsymbol{S}_j(t_k) - \boldsymbol{S}_i(t_k)}{|\boldsymbol{S}_j(t_k) - \boldsymbol{S}_i(t_k)|}\frac{L-l}{2} \\
\boldsymbol{S}_j^*(t_k) &= \boldsymbol{S}_j(t_k) + \frac{\boldsymbol{S}_i(t_k) - \boldsymbol{S}_j(t_k)}{|\boldsymbol{S}_i(t_k) - \boldsymbol{S}_j(t_k)|}\frac{L-l}{2} \\
\boldsymbol{S}_j^*(t_{k+1}) &= \boldsymbol{S}_j(t_{k+1}) + \frac{\boldsymbol{S}_i(t_{k+1}) - \boldsymbol{S}_j(t_{k+1})}{|\boldsymbol{S}_i(t_{k+1}) - \boldsymbol{S}_j(t_{k+1})|}\frac{L'-l'}{2} \\
\boldsymbol{S}_i^*(t_{k+1}) &= \boldsymbol{S}_i(t_{k+1}) + \frac{\boldsymbol{S}_j(t_{k+1}) - \boldsymbol{S}_i(t_{k+1})}{|\boldsymbol{S}_j(t_{k+1}) - \boldsymbol{S}_i(t_{k+1})|}\frac{L'-l'}{2}
\end{aligned} \tag{3.8}$$

These 4 points, $\left[\boldsymbol{S}_i^*(t_k),\ \boldsymbol{S}_j^*(t_k),\ \boldsymbol{S}_j^*(t_{k+1}),\ \boldsymbol{S}_i^*(t_{k+1})\right]$, identify a quadrilateral planar swath. The time step is small enough to assume that satellites move in straight line. Since this quadrilateral is skew, these points are transformed to topocentric-horizontal coordinate system with projection to surface.

3.2.3.3 First Coverage Estimation: Sum of Areas of Simple and Complex Quadrilaterals

There are two quadrilateral cases as shown in Fig. 3.10. The first one is simple quadrilateral while the other is a complex (self-intersecting) quadrilateral.

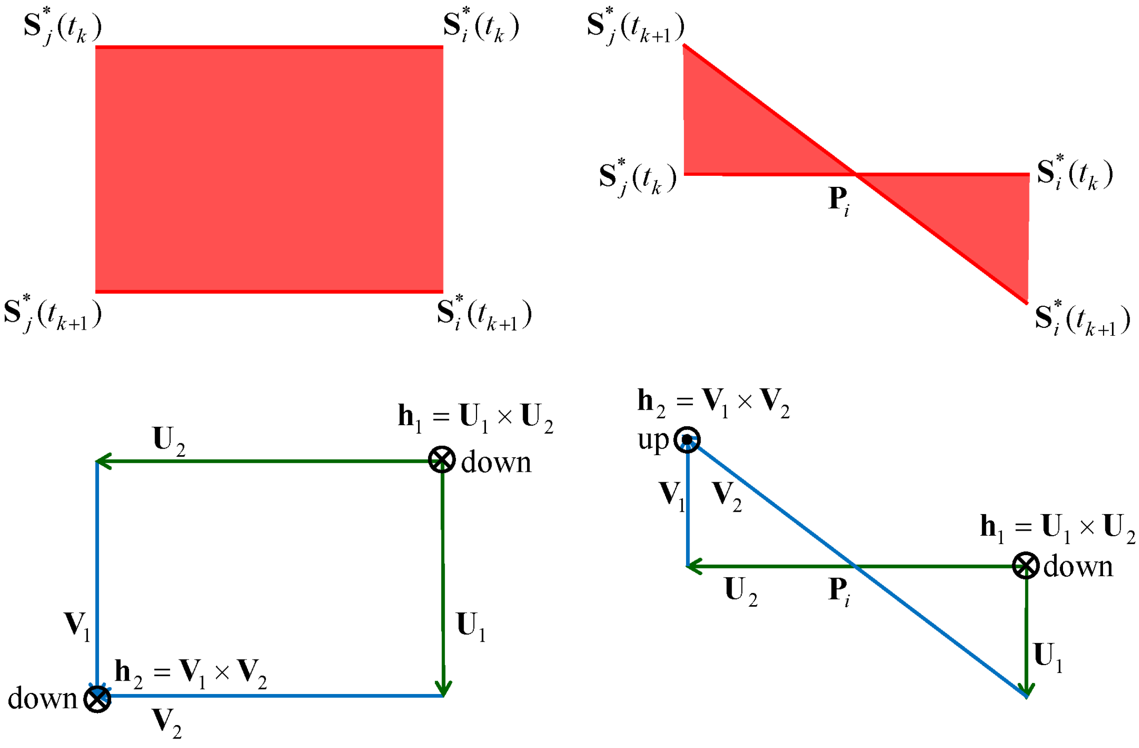

Figure 3.10: Simple and complex quadrilaterals

Using position vectors which are given by Eq. (3.8) we can get vectors such as $\boldsymbol{U}_1$, $\boldsymbol{U}_2$, $\boldsymbol{V}_1$ and $\boldsymbol{V}_2$. Then, vectors $\boldsymbol{h}_1$ and $\boldsymbol{h}_2$ can be obtained by cross products as shown in Fig. 3.10. The condition associated with a simple quadrilateral is

$$\boldsymbol{h}_1 \cdot \boldsymbol{h}_2 > 0 \tag{3.9}$$

Because all quadrilaterals consist of two triangles regardless of shape, area of simple or complex quadrilaterals can always be obtained by summing the areas of two triangles. Area for simple case is obtained by

$$A_{\text{simple}} = \frac{|\boldsymbol{h}_1|}{2} + \frac{|\boldsymbol{h}_2|}{2} \tag{3.10}$$

In complex case, there are some additional processes because we find intersecting point ($\boldsymbol{P}_i$) and then define related vectors as follows.

$$\begin{aligned} \boldsymbol{U}_2' &= \boldsymbol{P}_i - \boldsymbol{S}_i^*(t_k) \\ \boldsymbol{V}_2' &= \boldsymbol{S}_j^*(t_k) - \boldsymbol{P}_i \\ \boldsymbol{h}_1' &= \boldsymbol{U}_1 \times \boldsymbol{U}_2' \\ \boldsymbol{h}_2' &= \boldsymbol{V}_1 \times \boldsymbol{V}_2' \end{aligned} \tag{3.11}$$

Similarly, area for complex case is given by

$$A_{\text{complex}} = \frac{|\boldsymbol{h}_1'|}{2} + \frac{|\boldsymbol{h}_2'|}{2} \tag{3.12}$$

The total coverage is obtained by summing all planar swaths by all satellites pairs combinations. For instance, by summing all planar swaths by all satellite combinations during one quart of the period gives a quarter period coverage. However, net coverage cannot be obtained this way because of the existing overlapping areas. In order to estimate the net coverage, methods to count overlapping area are required.

3.2.3.4 Second Coverage Estimation: Using Uniform Distributed Points on a Sphere

The creation of uniform distribution of points on a sphere can be used to estimate net coverage by checking the number of overlapping times. Among all the existing methods to generate uniformly distributed points on a sphere the method presented in Ref. [21] is adopted here. Starting with an icosahedron (20 identical equilateral triangular faces) and performing 8 sequential divisions in identical spherical triangles, $20 \cdot 2^8 = 5,120$ triangles with same spherical areas are obtained whose centers approximate 5,120 uniformly distributed points on a sphere, as shown in Fig. 3.11.

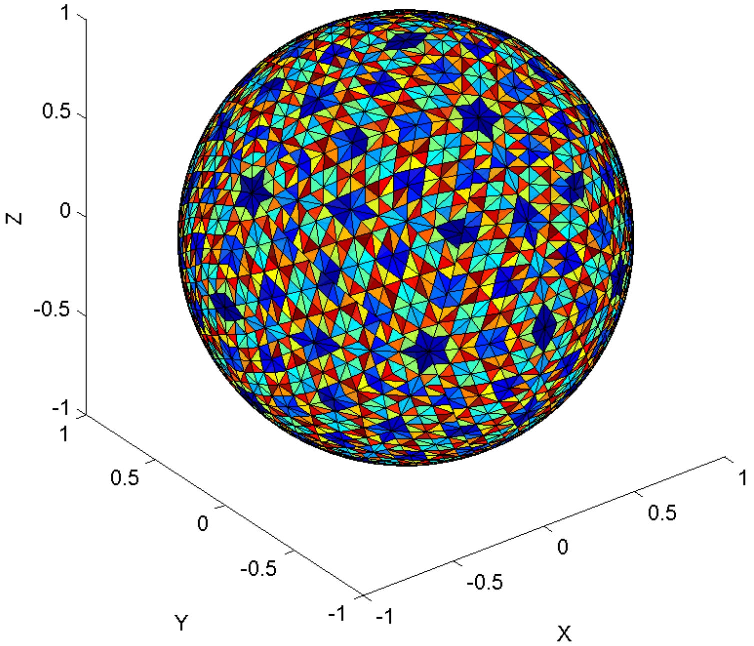

Figure 3.11: Icosahedron split by 8 divisions

Because every planar swath is quadrilateral, it can be divided into two triangles.

Therefore, checking if points are inside or outside triangle can determine if points are observed or not. Figure 3.12 shows the geometry of observation and non-observation cases. In case of observation (left), the sum of the areas of the three sub-triangles is equal to the area of the original triangle while the non-observation case (right) is experienced if the total area is greater than the area of the original triangle.

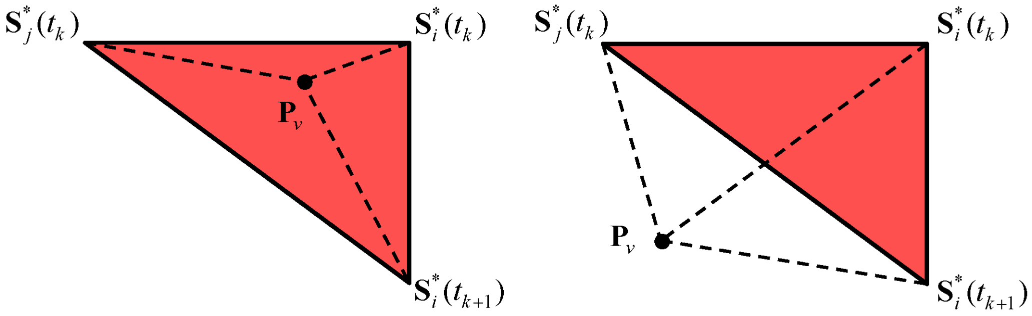

Figure 3.12: Geometry of observation and non-observation cases

In order to check observation condition, all uniformly distributed points are transformed to topocentric-horizon coordinate system with mid-point of triangle as origin, and then projected to surface as all points of quadrilateral are transformed. Equation to check whether the point $\boldsymbol{P}_v$ is observed is given by

$$\begin{gathered}A(\boldsymbol{P}_v\boldsymbol{S}_i^*(t_k)\boldsymbol{S}_j^*(t_k)) + A(\boldsymbol{P}_v\boldsymbol{S}_j^*(t_k)\boldsymbol{S}_i^*(t_{k+1}))+ \\ +A(\boldsymbol{P}_v\boldsymbol{S}_i^*(t_{k+1})\boldsymbol{S}_i^*(t_k)) = A(\boldsymbol{S}_i^*(t_k)\boldsymbol{S}_j^*(t_k)\boldsymbol{S}_i^*(t_{k+1}))\end{gathered} \tag{3.13}$$

3.2.4 LFC Optimization

3.2.4.1 Fitness Function

The fitness function utilized to drive the optimization process is designed to maximize the percentage of active time with respect to a reference time. Fitness function has been implemented to count the times that pairs of satellites see each other through the atmosphere. This is simply determined by the geometric conditions expressed by Eq. (3.4). For computation of the percentage of active time, geometric conditions for all the i-j satellite combinations should be considered. Thus, the optimality is defined by the minimization of the following function

$$L = \left(\frac{K\Delta t}{T}\right)^{-1} \tag{3.14}$$

where K is the number of times satisfying geometric conditions, Δt is the time step, and T is the orbital period.

3.2.4.2 Ranges of Design Parameters

The ranges of design parameters are given in Table 3.10.

Table 3.1: Ranges of design parameters for optimization with N_s=12

Parameters	**Ranges**
$[N_o, N_{so}]$	[1,12] [2,6] [3,4] [4,3] [6,2] [12,1]
N_c	[1, N_o], integer
T	[1.51 hr, 1.93 hr]
i	[0, 180 deg]

3.2.4.3 Re-Oriented Constellations

Any constellation can be re-oriented just by using rigid rotation matrix with free selection of axis and angle of rotation in order to provide desired performance in specific region. In Fig. 3.13, $\hat{\boldsymbol{n}}_k$, $\hat{\boldsymbol{e}}_k$ and $\hat{\boldsymbol{h}}_k$ are node, eccentricity, and angular momentum vectors of k-th orbit in the constellation, respectively.

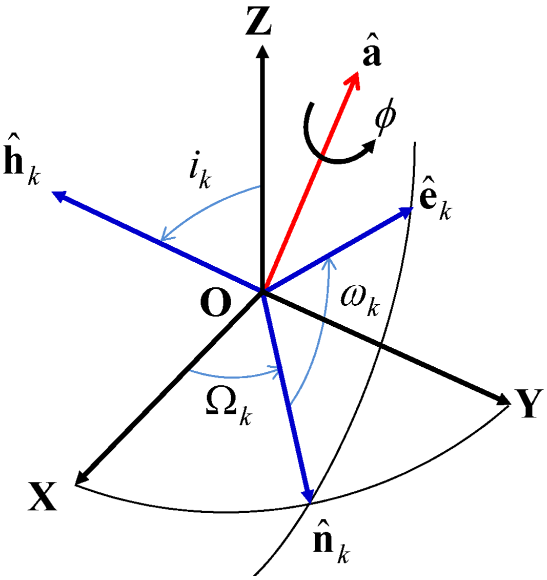

Figure 3.13: Rigid rotation matrix with free selection of axis and angle of rotation

Node vector and eccentricity vector of each orbit in the constellation can be expressed in terms of orbit elements as follows.

$$\begin{aligned} \hat{\boldsymbol{h}}_k &= f_1(i_k, \Omega_k) \\ \hat{\boldsymbol{e}}_k &= f_2(i_k, \Omega_k, \omega_k) \end{aligned} \tag{3.15}$$

where i_k, Ω_k, ω_k are the inclination, the right ascension of the ascending node and the argument of perigee of k-th orbit, respectively. Then, considering rotating-plane lattice flower constellations with circular orbits and same orbit inclination, we obtain

$$\begin{aligned} \hat{\boldsymbol{h}}_k &= f_1(i, \Omega_k) \\ \hat{\boldsymbol{e}}_k &= f_2(i, \Omega_k) \end{aligned} \tag{3.16}$$

Rigid rotation matrix is given by

$$\boldsymbol{R}(\hat{\boldsymbol{a}}, \phi) = I_{3\times3} \cos\phi + (1 - \cos\phi)\hat{\boldsymbol{a}}\hat{\boldsymbol{a}}^{\mathrm{T}} + [\hat{\boldsymbol{a}}\times] \sin\phi \tag{3.17}$$

where $\hat{\boldsymbol{a}}$ and ϕ are axis and angle of rotation, respectively [57].

Using the rigid rotation matrix, angular momentum and eccentricity vectors can be obtained as follows

$$\begin{aligned} \hat{\boldsymbol{h}}'_k &= \boldsymbol{R}(\hat{\boldsymbol{a}}, \phi)\hat{\boldsymbol{h}}_k = g_1(i'_k, \Omega'_k) \\ \hat{\boldsymbol{e}}'_k &= \boldsymbol{R}(\hat{\boldsymbol{a}}, \phi)\hat{\boldsymbol{e}}_k = g_2(i'_k, \Omega'_k) \end{aligned} \tag{3.18}$$

3.2.5 Results: Optimal Radio Occultation Constellations

3.2.5.1 String-Of-Pearls Polar Constellatio

The first constellation analyzed for radio occultation mission is a single-orbit, conventional, string-of-pearls constellation whose design parameters are given in Table 3.11. There is no single unique optimal solution because inclination (i) is independent of the active time when there is one orbital plane in constellation. In order to provide global coverage the orbit inclination is set to 90° (polar orbit).

Table 3.2: LFC parameters of string-of-pearls polar constellation

Parameters	**Optimal values**
$[N_o, N_{so}]$	[1,12]
N_c	N_o
T	1.51 (hr)
i	90 (deg)

Fig. 3.14 illustrates the satellite trajectories of the string-of-pearls polar constellation as seen from the Earth-Centered Inertial (ECI) frame. All satellites of this constellation have same orbital plane and all two consecutive satellites see each other, as shown in the figure. This polar orbit constellation provides global coverage due to the rotation of the Earth. However, long time is required to complete the global coverage and the coverage density is strongly latitudinal dependent with maximum observation at poles.

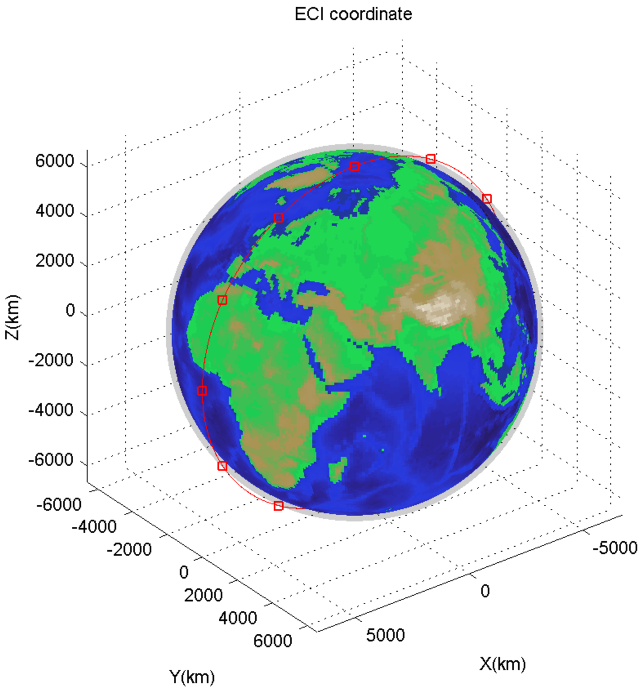

Figure 3.14: String-of-pearls polar constellation

3.2.5.2 Plane Lattice Flower Constellations

Although all satellites of a constellation don't have same orbital plane, it is possible to design constellations whose satellites lie on the same plane using different orbital planes. Compared with conventional string-of-pearls polar constellation, these constellations have advantage of relatively short time to cover global area although they can not provide global coverage. The disadvantage is that the deployment of this constellation may require more than a single launch. These constellations are called *plane lattice flower constellations.* The LFC parameters of designed plane lattice flower constellations are provided in Table 3.3. First one is called *rotating-plane lattice flower constellation* because axis of plane is coning about a fixed axis. The other is called *fixed-plane lattice flower constellation* because the plane where the satellites do not change its orientation.

Table 3.3: LFC parameters of plane lattice flower constellations

Parameters	**Rotating-plane LFC**	**Fixed-plane LFC**
$[N_o, N_{so}]$	[6,2]	[12,1]
N_c	1	0
T	1.51 (hr)	1.51 (hr)
i	21.78 (deg)	76.94 (deg)

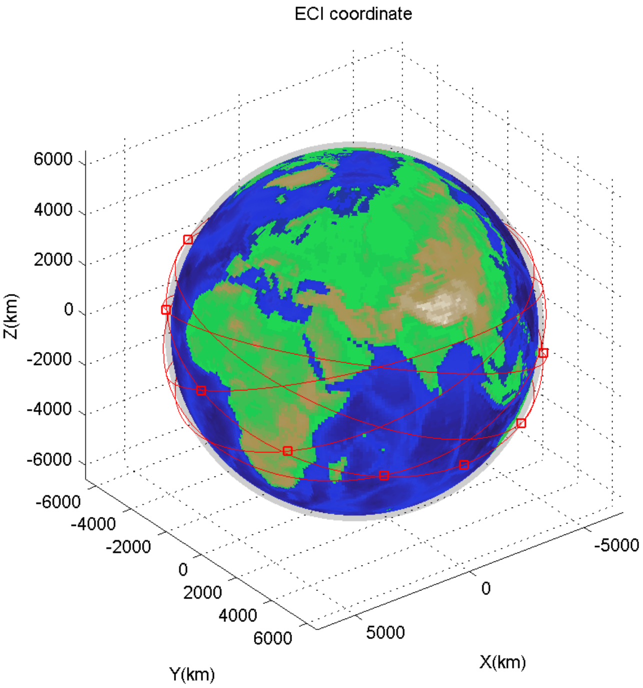

Figure 3.15: Rotating-plane lattice flower constellation

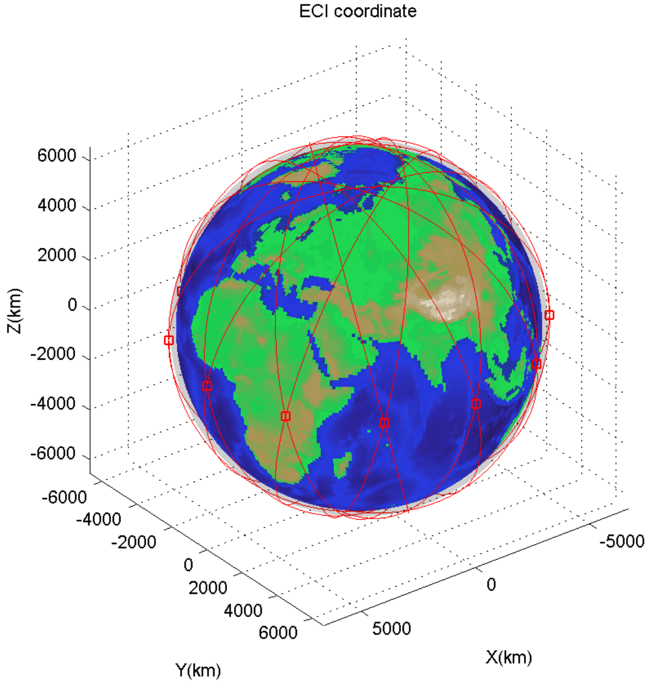

Figure 3.16: Fixed-plane lattice flower constellation

Figs. 3.29a - 3.29b show the satellite trajectories of plane lattice flower constellations as seen from the ECI frame.

When all satellites of a constellation lie in the same plane, then the rank of a matrix made of the position vectors must be 2. This position matrix is given by Eq. (3.19).

$$\boldsymbol{M} = [\hat{\boldsymbol{r}}_1 \quad \hat{\boldsymbol{r}}_2 \quad \cdots \quad \hat{\boldsymbol{r}}_n] \tag{3.19}$$

where n is the total number of satellites. Since the rank of a matrix is equal to the number of non-zero singular values, the singular values of a quadratic form of the matrix have been computed. Minimum singular values of the position matrix for various inclinations, $[N_o, N_{so}, N_c] = [6, 2, 1]$ and $T = 1 : 51(\text{hr})$ are shown in Fig. 3.17 for the rotating-plane LFC. Note that, using designed conditions, rotating-plane

LFC can be used for low inclinations. In case of fixed-plane LFC, minimum singular values for various inclinations are always zero as we expected.

Figure 3.17 shows that the rotating-plane LFC is really planar for low inclinations. Of course, for fixed-plane LFC, the rank of the position matrix is always 2, as we expected.

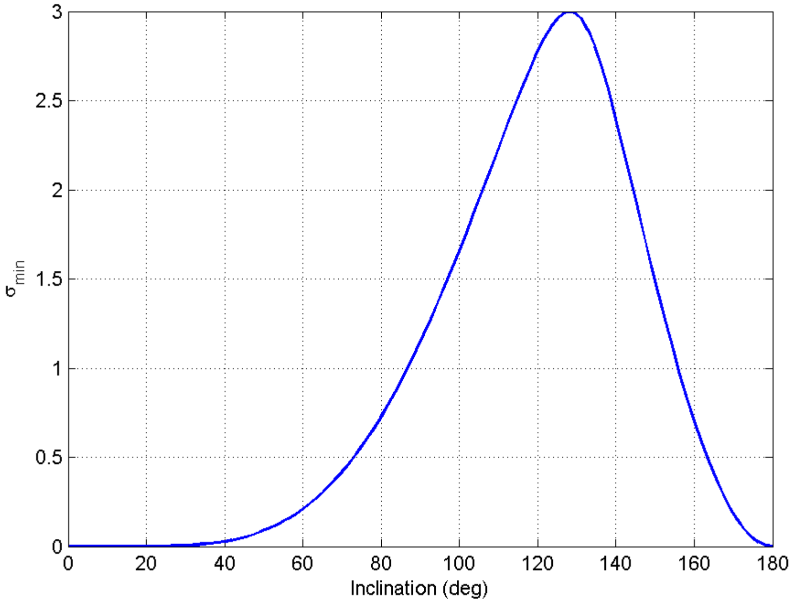

Figure 3.17: Minimum singular values for various inclinations, $[N_o, N_{so}] = [6, 2], N_c = 1$ and $T = 1.51$(hr) in rotating-plane lattice flower constellation

3.2.6 Two Coverage Performance Evaluations

3.2.6.1 First Coverage Estimation Result: Sum of Areas of Simple and Complex Quadrilaterals

In this simulation, we set a time step to $\dfrac{T}{100}$. Single planar swath by two satellite of rotating-plane lattice flower constellation with single time step is displayed in Fig.

3.18. Quarter period coverage can be estimated by summing all planar swaths by all satellite combinations during a quarter period. However, the estimated coverage is not net coverage because there are overlapping areas as shown in Fig. 3.19.

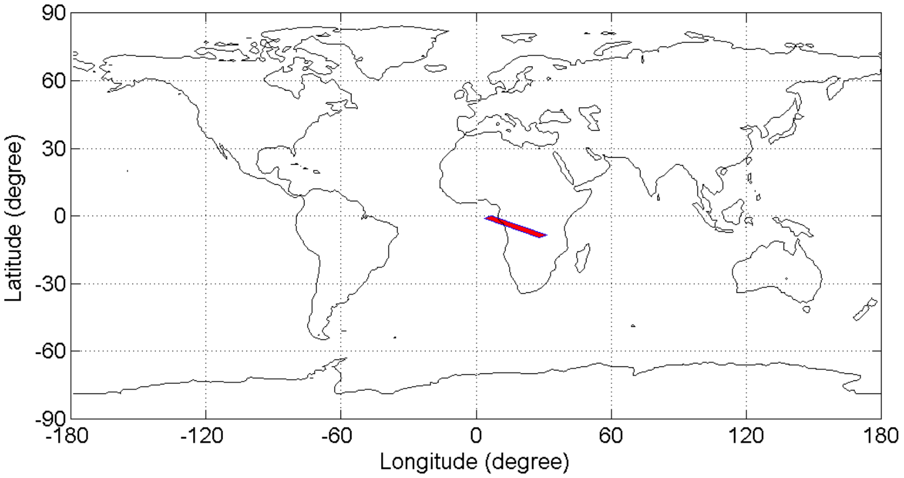

Figure 3.18: Single planar swath by two satellites with single time step

3.2.6.2 Second Coverage Estimation Result: Using Uniform Distributed Points on a Sphere

In order to verify method using uniform distribution of point on a sphere, total coverage are estimated using various number of uniform distributed points on a sphere. Single period coverage percent and errors obtained with different number of points on string-of-pearls polar constellation are in Table 3.4. Because single planar swath of string-of-pearls polar constellation is narrower than other constellations, two coverage estimation methods have most significant difference in this constellation. Therefore, two coverage estimation methods are applied to string-of-pearls polar

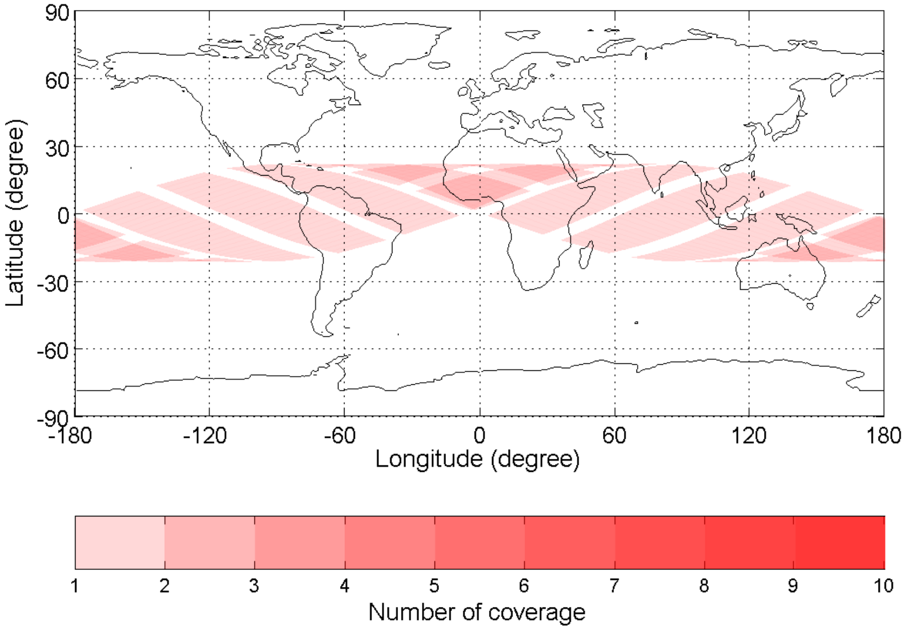

Figure 3.19: A quarter period coverage of rotating-plane lattice flower constellation

constellation. Errors are calculated by comparing with result which is obtained by sum of quadrilaterals (8.64%).

Table 3.4: Comparison of total coverage obtained with different number of points

Number of points	**Total coverage** (%)	**Error** (%)
2,560	15.24	76.4
5,120	11.56	33.8
10,240	9.65	11.7
20,480	8.96	3.7
81,920	8.86	2.6
163,840	8.67	0.3
1,310,720	8.65	0.1

From these results, we can conclude that method using uniform distribution of point on a sphere needs appropriate number of points to give accurate results. Simulation with $1,310,712$ points was performed in order to estimate net coverage. Single period simulation results of all designed constellations are shown in Figs. 3.20 - 3.22. Results by uniform distribution of point on a sphere are shown in Earth-Centered Earth-Fixed (ECEF) frame and have good agreement with 2-D view results of first coverage estimation method.

3.2.6.3 Comparison of Coverage Performances

As mentioned above, net coverage can be obtained by method with uniform distribution of points in sphere. Comparison of coverage performances by designed constellations are provided in Table 3.5. Plane lattice flower constellations provides global coverage with relatively short time while string-of-pearls polar constellation require long time to cover global area. As shown in Fig. 3.21 and Fig. 3.22, rotating-plane lattice flower constellation provide good performance in a low latitude region while fixed-plane lattice flower constellation is suitable in a high latitude region.

Table 3.5: Comparison of coverage performances (net coverage, %)

Time	**String-of-pearls polar**	**Rotating-plane LFC**	**Fixed-plane LFC**
1 period	8.63	36.20	77.27
0.5 day	68.95	36.90	87.87
1 day	90.32	36.92	88.09

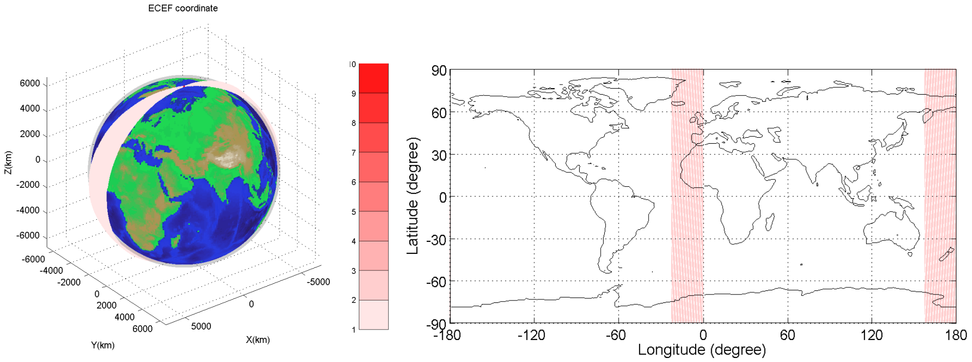

Figure 3.20: Single period coverage of string-of-pearls polar constellation

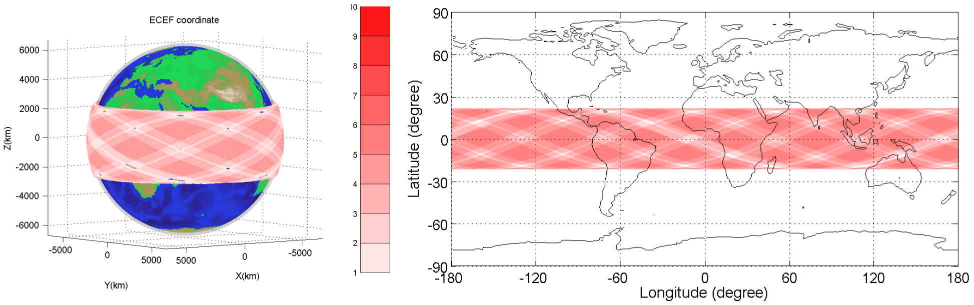

Figure 3.21: Single period coverage of rotating-plane lattice flower constellation

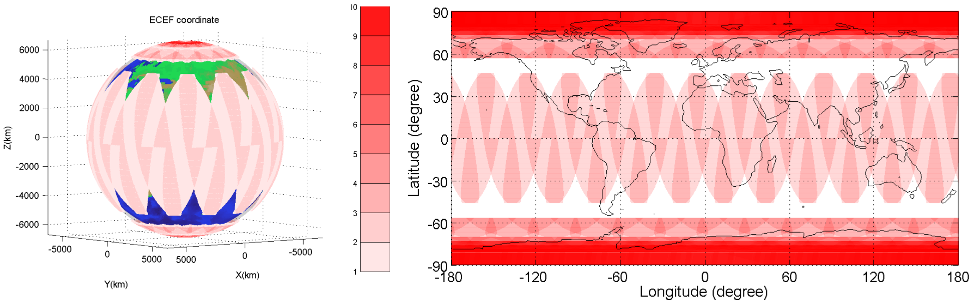

Figure 3.22: Single period coverage of fixed-plane lattice flower constellation

3.2.6.4 Re-Oriented Rotating-Plane Lattice Flower Constellations

Using the relationship Eq. (3.18), we obtain orbit elements of the re-oriented constellation. Note that, re-oriented constellation has different inclination while original plane lattice flower constellation has identical inclination.

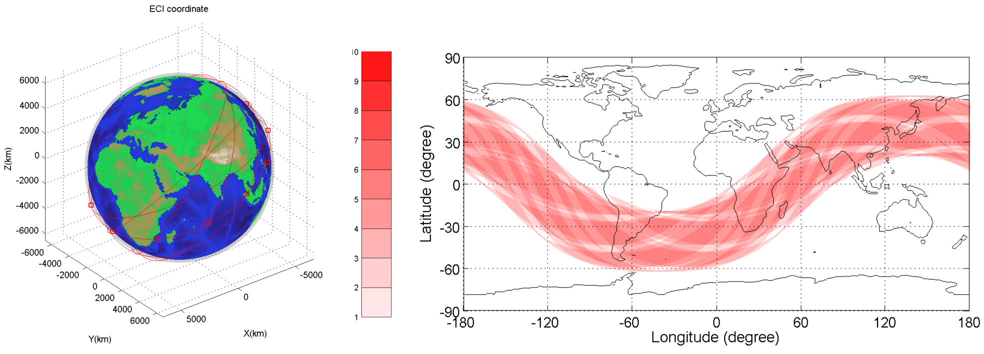

(a) (b)

Figure 3.23: Re-oriented rotating-plane lattice flower constellation (a) The satellite trajectories (b) Single period coverage in 2-D view

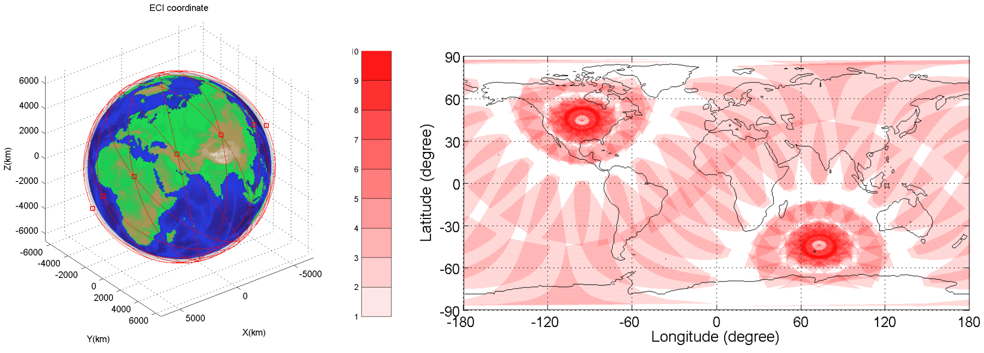

(a) (b)

Figure 3.24: Re-oriented fixed-plane lattice flower constellation (a) The satellite trajectories (b) Single period coverage in 2-D view

Figs. 3.23 and 3.24 show the satellite trajectories and single period coverage of the re-oriented plane lattice flower constellations. Note that the re-oriented plane lattice flower constellations provide service in specific regions. The re-oriented fixed-plane flower constellation provides good performance in mid latitudes areas including highly populated regions such as the United States, Europe and Northeast Asia.

3.2.7 Conclusions

In this work, we analyzed and designed constellations for radio occultation mission of the Earth atmosphere. The Genetic Algorithms technique with 2-D Lattice Flower Constellation theory has been used to find the best constellation for the mission. Three different satellite constellations are found by maximizing active time with minimum distance constraint. Optimal solutions have not only conventional string-of-pearls polar constellation but also novel plane lattice flower constellation which have good coverage characteristics. In order to evaluate coverage performance, geometries of linear and planar swaths have been investigated and total coverage has been estimated. To count overlapping areas, uniform distribution of points on a sphere is introduced and net coverage of three different satellite constellations have been estimated by checking observation conditions of all uniformly distributed points on the sphere. It has been found that the proposed plane lattice flower constellations provide good performance for time to cover global area although they can't provide coverage for entire Earth. The rotating-plane lattice flower constellation and the fixed-plane lattice flower constellation have good coverage characteristics in low and high latitude region, respectively. In addition, the re-oriented plane lattice flower constellations provide good coverage performance in specific regions.

3.3 Optimization of Lattice Flower Constellations for Intensity Correlation Interferometric Missions

3.3.1 Introduction

Several space missions have used optical interferometry for astronomy to characterize distant galaxies, search for extra-solar planets, and identify black holes[58, 59]. Since the Earth's atmosphere absorbs certain wavelengths, it limits the brightness of the observed objects. Therefore, observations from space are ideal to perform optical interferometry for astronomy[60]. However, very large instrument dimensions are required to obtain high resolution images using a monolithic telescope because the accessible resolution is directly proportional to the diameter of the telescope dish and inversely proportional to the distance between the telescope and the object to be observed[61]. It would be impractical to build a single giant telescope as the cost increases faster than the second power of the mirror diameter[62].

Technological advances in high angular resolution astronomy have been obtained using arrays of more modest-sized telescopes to produce a resolution equal to that provided by a large monolithic telescope[63, 64]. Since this resolution can be performed by multi-satellites interferometric imaging systems, the possibility of using these systems has gained great interest during the past several decades. Interferometric imaging can be implemented by evaluating differences in signal phases taken from different positions. Unfortunately, traditional methods for interferometric imaging have severe constraints in both position and attitude accuracies. Therefore, tremendous effort has been dedicated to controlling satellites effectively[65, 66, 67].

With these limitations on traditional systems, *Intensity Correlation Interferometry* (ICI) has seen renewed interest since the 1950s when it was conceived[68, 69]. Alternative approaches using ICI allow interferometric imaging to be performed by measuring only signal intensities. This approach does not have severe constraints on position and attitude accuracies, but it requires a phase retrieval process and an on-board atomic clock. These constraints do not constitute difficult problems since they can be solved. This innovative concept of multi-satellite intensity correlation interferometry imaging implies a constellation design for high resolution images. This is accomplished by evaluating the signal intensities from several sources. To reconstruct the source image with high accuracy, the design of such systems requires spacecraft in orbits whose relative motion covers, as much as possible, the image frequency content, which is identified by the resolution disc on the frequency plane.

From previous studies, we can find optimized sparse aperture arrays such as the Golay Configurations[70] or free-flying telescopes on string-of-pearl configurations[71]. In the Golay Configurations, the satellites are rigidly connected in order to maintain the desired configuration. In this paper we intend the opposite: we want the inter-satellite distances to be continuously changing and to obtain the coverage of the resolution disc. The String of Pearls is an optimized spacecraft formation that is composed of a string of free-flying telescopes, all orbiting in the same orbit, and all pointing toward the object to be observed at different values of mean anomaly. The optimality here is to select the mean anomalies to avoid repeating baselines configurations. In particular, the distances between the satellites have to be a multiple value of the scaled diameter of the (frequency) paintbrush that paints the resolution disk. When the satellites orbit around the Earth, the paintbrush is able to sufficiently cover the resolution disk. With this configuration, the imaging time is equal to a half orbital period. This research study shows how to derive these parameters in order to maximize the resolution disc coverage. Reasonable initial ranges of constellation parameters can be determined by the Earth's atmospheric altitude and internal Van Allen belts altitude.

Flower constellation theory was first studied for use in optical interferometry in Refs. [72] and [73], where the Flower Formation Flying[10] was introduced for multi-spacecraft interferometric systems and optimized using Genetic Algorithm (GA) and Particle Swarm Optimization (PSO). The main limitation of this research was the selection of Keplerian orbits only. In this study, the newly proposed 3-D Lattice Flower Constellations (3D-LFC) theory[12], which includes the J_2 gravitational perturbation, is adopted to design constellations to fulfill mission requirements.

This section is organized as follows. The first part briefly describes the Optical Interferometry. We then provide general design considerations, define the LFC parameter constraints, and proceed with the constellation design optimization. Then, the performances of some selected constellations for ICI optical interferometry missions are presented.

3.3.2 Intensity Correlation Interferometry

Interferometry measures fringes that arise because of the wave nature of light, and it contains information on the structure and position of the object to be observed. When light passes through an aperture, it is diffracted and forms an interference pattern of light on a viewing screen. Optical interferometry collects two or more light rays arriving from different observation points and then coherently combines them to form an interference pattern[72]. Evaluating the visibility (contrast of the fringe pattern) and phase of these fringes gives the mutual intensity required to reconstruct the image. The light beams are collected, transmitted to a combiner, and then Fourier transformed by using the Modulation Transfer Function (MTF)[74] because there is a relationship between the inference pattern and Fourier transformation. While traditional optical interferometry requires a magnitude and a phase of the interference pattern, an ICI system can only detect the magnitude of the interference pattern. The phase of interference pattern should be recovered through various computational methods which have been previously developed.

One of the most important factors of optical interferometry is the image's resolution level to achieve. The angular resolution is defined as a quantitative measure of the ability to produce the minimum angle between two point sources such that the system is able to distinguish two sources, not one. For a circular aperture of diameter D_T, an empirical limit for the resolution angle θ_r is given by the Rayleigh's criterion[75]

$$\theta_r = 1.22\,\frac{\lambda}{D_T} \tag{3.20}$$

where λ is the wavelength of light. The angular resolution is related to the resolution ε through the distance H between the telescope mirror and the observed object

$$\theta_r = \tan^{-1}\left(\frac{\varepsilon}{H}\right) \simeq \frac{\varepsilon}{H}. \tag{3.21}$$

Therefore, for a given wavelength, the size of objects that can just be discerned is determined by the aperture diameter D_T

$$D_T = 1.22\,\frac{\lambda H}{\varepsilon}. \tag{3.22}$$

From Eq. (3.22), it is evident that the larger the mirror, the better resolution obtained, but there is an effective limit to telescope size. Consequently, a multi-spacecraft interferometric imaging system is a very good solution for this problem. If the telescopes are spread out over a large area, it is possible to observe very small objects at close distances or large objects at far distances.

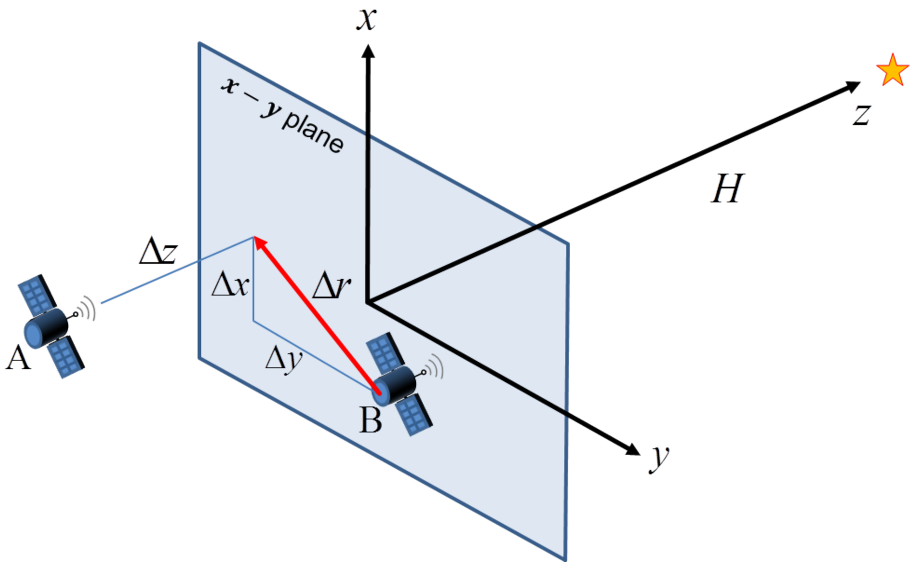

Figure 3.25: Physical plane

As shown in Fig. 3.25, there is a star located at distance H from $x-y$ observation plane. The physics is the same regarding Young's double slit interference experiment[76] where the star is the light source, the satellites are the slits, and the separation of the slits is the baseline. Let Δr be the projection of the baseline between satellites A and B onto a (x, y) plane perpendicular to the line of sight direction, and Δx and Δy the components of Δr on the observation plane[77]. A two dimensional plane of spatial frequencies called the Fourier wave-number plane or the (u, v) plane is defined where each unit is the number of wavelengths between the apertures. The (u, v) plane has components

$$(u,\, v) = \left(\frac{\Delta x}{\lambda},\, \frac{\Delta y}{\lambda}\right) \tag{3.23}$$

The MTF $M(\mathbf{u})$ is

$$M(\mathbf{u}) = \int A_T(\mathbf{u}+\mathbf{v})\, A_T(\mathbf{v})\, d\mathbf{v} \tag{3.24}$$

where A_T is the aperture function. From Eq. (3.24), it is evident that the MTF is the correlation of the aperture function. For a monolithic circular aperture telescope with diameter D_T, the A_T is

$$A_T(\mathbf{x}) = \begin{cases} 1 & \text{if } |\mathbf{x}| \leq D_T/2 \\ 0 & \text{otherwise} \end{cases} \tag{3.25}$$

If the (u, v) plane is not totally covered, the imaging system is blind to corresponding frequencies and information associated to the unexplored frequency subset ranges. Although complete coverage is not required to reconstruct the image, larger coverage provides a better performance.

Images of celestial objects are reconstructed through different measurements taken in successive time instants. While moving relative to each other, the spacecrafts' configuration changes with time and this creates different projections of the baseline onto a plane perpendicular to the line of sight to the object to observe. A simultaneous measurement of the coherence for all the baselines is assumed. If each satellite has one telescope and N_s is the total number of satellites, there are $N_s(N_s-1)/2$ baselines[78]. The light beams are collected by each telescope, split in (N_s-1) ways, transmitted to a combiner and then Fourier transformed in the (u, v) plane. For every point in this plane there is a symmetrical one with respect to the origin. The challenge is to obtain a wide variety of baseline lengths and orientations for covering the (u, v) plane in an optimal way.

The maximum angular radius of the resolution disk is related to the maximum inter-satellites distance D, and it is defined as

$$R_{\max} = \frac{D}{\lambda} = \frac{1.22\,H}{\varepsilon} \tag{3.26}$$

where Eqs. (3.23) and (3.22) have been used. Every point covers the (u, v) plane with a ball of diameter

$$\rho = 2\,\frac{R_{\max}}{N} \tag{3.27}$$

where N is the number of pixels on a side that we desire for the final image.

Let the number of satellites, N_s, be equal to 4 as indicated in Fig. 3.26a showing the physical plane orthogonal to the observing direction. This will result in $N(N-1) = 12$ coverage balls [79], which is twice the total number of different inter-satellite baselines.

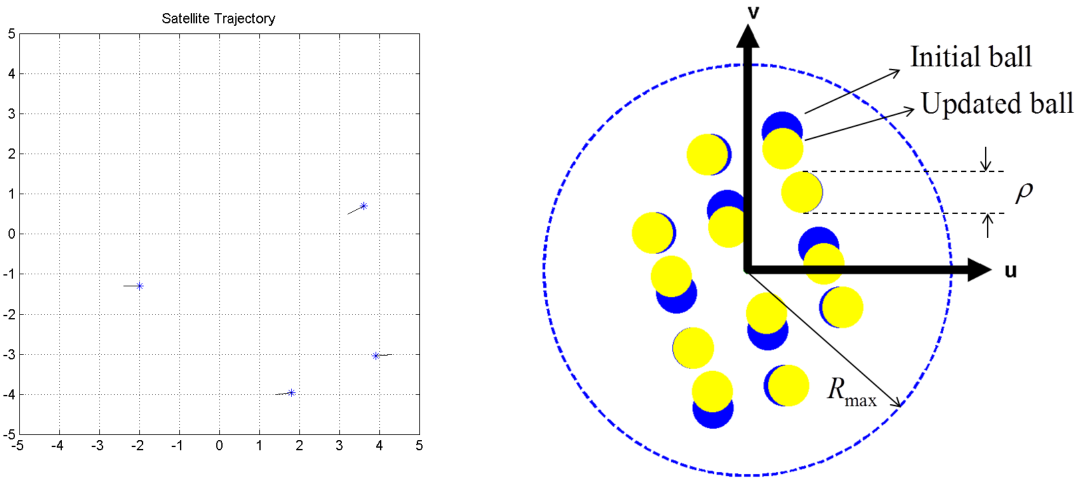

(a) Initial and updated locations of satellites

(b) (u, v) plane

Figure 3.26: Satellite trajectory and spatial frequency plane

Equation (3.23) gives initial and updated coverage balls whose diameter is ρ as shown in Fig. 3.27a. The outer circle is the resolution disc to be covered.

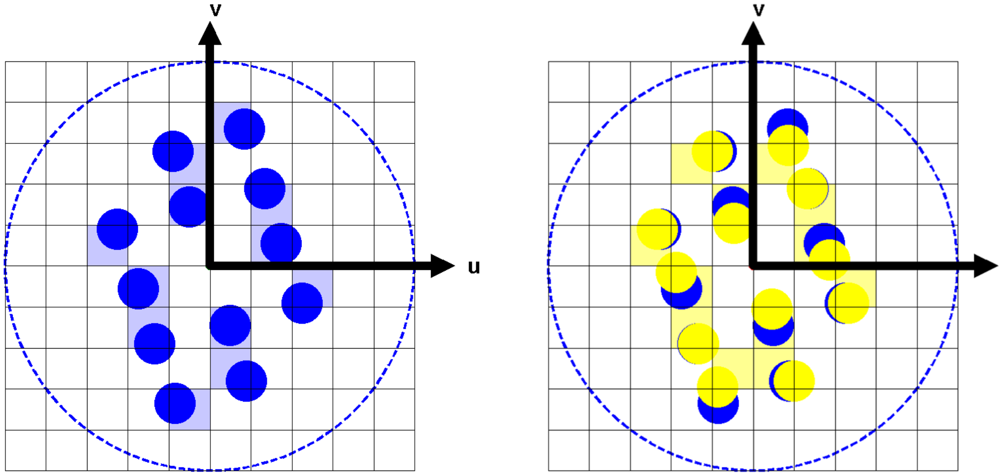

(a) Pixels plane for initial location (b) Pixels plane for updated location

Figure 3.27: Pixels plane

The interferometric measurements are made between a pair of telescopes. Therefore, more measurements are collected simultaneously with more satellites. We desired only the set of measurements $(u, v) : \sqrt{u^2 + v^2} \leq R_{\max}$, provided by Eq. (3.26). For an optimal coverage we are interested in having the resolution disk completely painted by the balls with the smaller number of spacecrafts.

Every point covered in the (u, v) plane represents a specific frequency and a specific direction, and this point can then be related to a pixel as shown in Fig. 3.27. The filled fraction of the u-v plane within the resolution disk indicates the quality of the resulting image.

3.3.2.1 Fitness Function

As constellation design for ICI missions using GA, defining a fitness function to drive the optimization process is the key issue. Since resolution disc coverage is closely related to ICI missions performance, two types of fitness functions using resolution disc coverage are utilized. They are compared in the results section, where it is shown how its election conditions the final obtained solution. The proposed fitness functions are:

- Type I: The first fitness function is designed to maximize the covered area of resolution disc. It has been implemented to count the number of covered pixels. Thus, the optimality is defined by the minimization of the following function

  $$L = -\sum_{i=1}^{N}\sum_{j=1}^{N} NZ(P_{i,j}) \tag{3.28}$$

  where N is the number of pixels, $P_{i,j}$ is entry of pixel matrix and defined by number that each pixel covered, and

  $$NZ(\mathbf{x}) = \begin{cases} 1 & \text{if } \mathbf{x} > 0 \\ 0 & \text{otherwise} \end{cases} \tag{3.29}$$

  Therefore, this fitness function is number of nonzero matrix elements and not considered overlapping time.

- Type II: The second fitness function considered corresponds with the total number of overlapped coverage. It is evaluated as follows:

  $$L = -\sum_{i=1}^{N}\sum_{j=1}^{N} \sqrt{P_{i,j}} \tag{3.30}$$

Since number of overlapped coverage is considered, designed constellation based on this fitness function is expected to have better performance in aspect of the signal to noise ratio.

3.3.2.2 Ranges of Design Parameters

The ranges of design parameters for optimization with $N_s = 4$ are given in Table 3.10.

Table 3.6: Ranges of design parameters for optimization with N_s=4

Parameters	**Ranges**
$[N_o, N_{so}, N_\omega]$	[1,1,4] [1,2,2] [1,4,1] [2,1,2],[2,2,1],[4,1,1]
N_{c1}	[1, N_o], integer
N_{c2}	[1, N_ω], integer
N_{c3}	[1, N_o], integer
$h_{\min}$ (km)	300
$h_{\max}$ (km)	1,500
i (deg)	[0, 180]

Optimization for various number of satellites cases with various No constraints have been performed. The ranges of other design parameters are the same as the values in Table 3.10.

3.3.3 Results

A study applying the 3-D LFC theory to the space interferometric imaging system has been performed. In this simulation, time step is set to $\dfrac{T}{100}$ and each satellite has one telescope. Considered specific objects to be observed is a star with a resolution $\epsilon = 100$ km. Distance from object plane to the observation region is 30 pc and the wavelength of visible light $\lambda = 500$ nm. This section is organized as follows: (i) designed constellation for Type I fitness function is shown as well as resolution disc coverage for various pixels sizes and number of satellites, and (ii) results using Type II fitness function have been provided comparing with result using Type I fitness function.

3.3.3.1 Designed constellation using Type I fitness function

Imagine a star with 10 × 10 pixels and 4 satellites. The optimal parameters of designed constellation are provided in Table 3.7. This constellation has good coverage performance. However, this is not a single unique solution, because the number of pixels is very small. Since all satellites of a constellation don't have an identical orbital plane, this constellation may require more than a single launch. Constellations that have a small number of orbital planes provide worse coverage performance.

Table 3.7: Optimal parameters of 3-D LFC using 4 satellites

Parameters	optimal values
$[N_o, N_\omega, N_{so}]$	[4,1,1]
N_{c1}	3
N_{c2}	0
N_{c3}	1
a (km)	7,911
e	0.05
i (deg)	114.7
T (hr)	1.945
Coverage (%)	100

Figure 3.28 illustrates the satellite trajectories of designed lattice flower constellations as seen from the Earth-Centered Inertial (ECI) frame.

Spatial frequency plane and pixels plane coverage for this constellation are shown in Fig. 3.29. It is clear that whole resolution disc is covered.

Several simulations for various number of satellites have been done with 100×100 pixels in order to investigate influence of large number of pixels on resolution disc coverage. The optimal parameters of each case are obtained in Table 3.8. In case of $N_s = 4$, coverage of optimal constellation is much lower than one of the 10×10 case as expected. Regarding the percentage of coverage greater than 95% is considered very good[72], we can conclude that 25 satellites are required in case of 100×100 pixels.

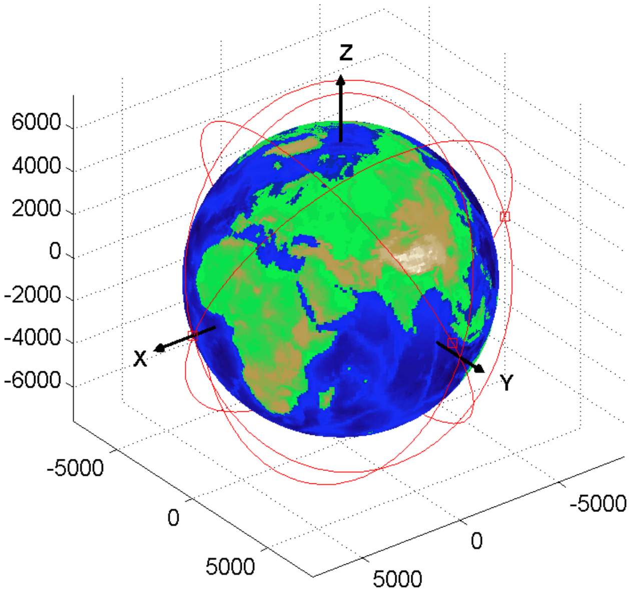

Figure 3.28: The satellite trajectories of designed lattice flower constellation

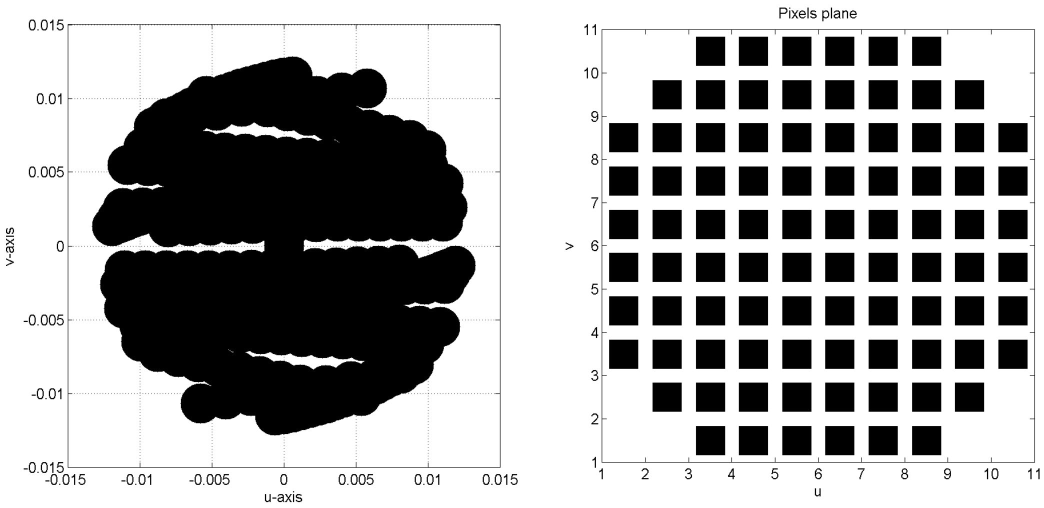

(a) u-v plane

(b) Pixels plane

Figure 3.29: Example of imaging Stars with 3-D lattice flower constellation using 4 satellites

Table 3.8: Optimal parameters of 3-D LFC using various number of satellites and 100×100 pixels

Parameters	$N_s = 4$	$N_s = 6$	$N_s = 10$	$N_s = 20$	$N_s = 25$
$[N_o, N_\omega, N_{so}]$	[4,1,1]	[6,1,1]	[10,1,1]	[20,1,1]	[25,1,1]
N_{c1}	3	1	7	11	23
N_{c2}	0	0	0	0	0
N_{c3}	2	4	4	8	3
a (km)	7,936	7,704	7,589	7,536	7,525
e	0.05	0.08	0.10	0.11	0.11
i (deg)	10.1	171.22	11.61	168.37	10.83
T (hr)	1.954	1.869	1.828	1.809	1.805
Coverage (%)	2	9	19	84	95

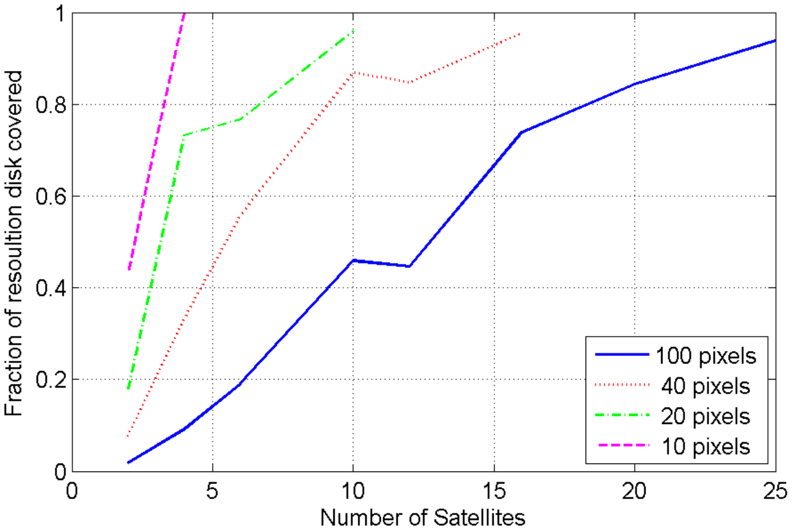

Figure 3.30: Coverage vs. number of satellites for various number of pixels

It is clear that the number of pixels affect the number of satellites required in Table 3.8. Simulations for various number of satellites and various number of pixels have been done as shown in Fig. 3.30.

3.3.3.2 Designed constellation using Type II fitness function

Optimization with two types of fitness functions has been performed for 20 × 20 pixels. 10 satellites have been used in simulation since at least 10 satellites are required for 20 × 20 pixels as shown in Fig. 3.30. The parameters of designed constellation are given in Table 3.9. Although Type II constellation had worse net coverage performance, it had better overlapped coverage as shown in Fig. 3.31. Since these characteristics can provide better a signal to noise ratio, this type of constellation can be selected for specific mission. In addition, Type II constellation is more economic because it has relatively fewer orbital planes.

Table 3.9: Optimal parameters of 3-D LFC using 10 satellites

Parameters	Type I	Type II
$[N_o, N_\omega, N_{so}]$	[10,1,1]	[5,1,2]
N_{c1}	1	1
N_{c2}	0	1
N_{c3}	0	1
a (km)	7,727	7,656
e	0.06	0.09
i (deg)	64.2	9.5
T (hr)	1.877	1.852
Coverage	96	91

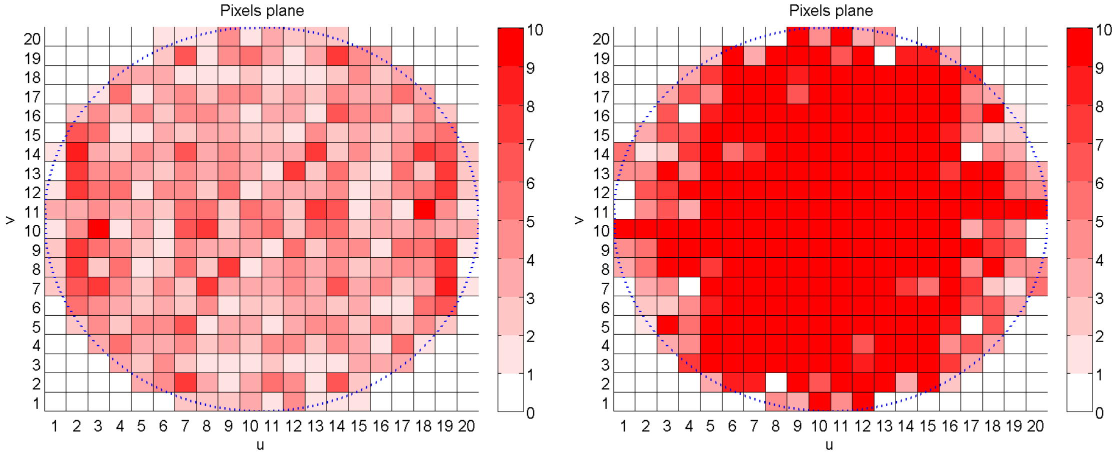

(a) Type I (b) Type II

Figure 3.31: Star imaging with 3-D lattice flower constellation using 10 satellites

3.3.4 Conclusions

This work proposes a method for preliminary design of optimal constellations for *intensity correlation interferometry* missions. Genetic Algorithms have been used to optimize constellations generated by the 3-D Lattice Flower Constellation theory. Two different types of fitness functions, Type I and Type II, are used for optimization and both of them provide good and comparable solutions. Constellations obtained using the Type I fitness function are characterized by good net coverage performance, while those generated using the Type II fitness function provide better overlapped coverage. Several simulations are performed in order to investigate the influence of the number of pixels on resolution disc coverage. It has been found that more than 25 satellites are required to cover 100 × 100 pixels for good image observation of a far star, while only 4 satellites are required to completely cover 10 × 10 pixels. These results are useful for constellation designers to select the most economical, or the most efficient fitness function.

3.4 Design of Constellations for Earth Observation with Inter-Satellite Links

3.4.1 Introduction

The constellations of multiple satellites equipped with SAR (Synthetic Aperture Radar) devices and high resolution optical instruments for Earth observation are required to have a design that provides fast revisit times and short response times [80]. Earth observation missions usually use repeating ground track orbits that allow for specific observations to be scheduled every certain amount of time or with the same observing conditions [81]. One of the most reliable and efficient methods for generating a repeat ground track is the Flower Constellations (FC) theory [10]. FC was studied for use in the Earth observation in Ref. [82] where 4 satellites were used at an altitude of 740 km for a revisit time of 6 days. However, the repeating ground track feature is not necessary in case of the constellation which consists of a large group of satellites. The FC theory has been recently expanded with the Lattice Flower Constellations (LFC) theory which encompasses all possible symmetric solutions [13]. Also, since the LFC theory decouples the compatibility condition and the shape parameters, it is useful to design a large constellation of satellites for the Earth observation mission.

Most Earth observation systems have space and ground segments connected by a complex network of communications to manage the operations of the constellation [80]. Many current constellations use inter-satellite links (ISL) for transmission of information between mutually visible satellites, because ISL networks enhance the autonomy of the constellations without the expense of a global ground-station network and reduce atmospheric transmission loss. ISL are direct communication paths along which a signal is transmitted from one satellite to another without ground station links [83]. ISL can be classified in the following two categories:

1. Intra-Orbit ISL are connections between satellites in the same orbital plane. Each satellite in the orbital plane connects a satellite orbiting ahead or behind itself. Because of invariant relative motion between the satellites in the same orbital plane, the antenna pointing angles for these ISL are constant and antenna steering is not required.

2. Inter-Orbit ISL connect satellites in adjacent orbital planes. Since the relative position of two satellites in adjacent orbital planes is changed over time, antenna steering is necessary [84]. Moreover, the distances between satellites in adjacent orbits vary within a large range and the Earth may eclipse their mutual line of sight. When the distance or viewing angle between two satellites changes too fast for the steerable antennas to follow, ISL can be temporarily switched off at certain intervals [85].

Radio frequency (RF) and optical link are the two types of links that can be considered for ISL. Optical link is several orders shorter than RF link. Therefore, it has some advantages such as high data capacity, small antenna size, and narrowness of the beam. The narrowness of the beam is several orders of magnitude less than that of RF. It provides the additional advantage of eliminating susceptibility to space-based or ground-based jammers. However, it is also a disadvantage since advanced pointing devices are necessary due to narrow beamwidth [86, 87]. The choice between RF and optical links depends on the mass, power consumed, and required capacity of the system.

This section is organized as follows. The first part examines observation mission and ISL communication in the constellation. We then discuss design considerations and parameters for 2D-LFC and optimize the design of the constellation. Finally, the performance of designed constellations for observation with ISL is presented.

3.4.2 Earth Observation Mission with ISL

3.4.2.1 Quality of Observation Mission

There are various ways to measure the quality of coverage to evaluate the observation performance as follows [5]:

1. The percent coverage for any point on the grid is simply the number of times that point was covered by one or more satellites divided by the total number of simulation time steps.

2. The mean coverage gap is the average length of breaks in coverage for a given point on the simulation grid.

3. The Mean Response Time (MRT) is the average time from when we receive a random request to observe a point until we can observe it [5].

Among these, the percent coverage is easily used since it shows directly how much of time a given point or region is covered. However, it does not consider gap statistics. Similarly, the mean coverage gap cannot evaluate performance correctly because it does not take coverage aspect into account. Therefore, MRT is required to evaluate the observation performance because it considers both the percent coverage and gap statistics.

3.4.2.2 Geometry of ISL

The establishment of ISL is mainly affected by the azimuth angle, elevation angle and transmission distance between satellites. The smaller the ranges of azimuth angle, elevation angle and transmission distance of ISL, the better the performance of ISL. Obviously, the ISL in the same orbital plane are more stable than those between adjacent orbital planes. An example of geometry for ISL is given in Fig.

3.32. Sat i and Sat j are defined as two satellites in the orbit I, and Sat k denotes the satellite in the orbit II. R denotes the orbit radius of satellites.

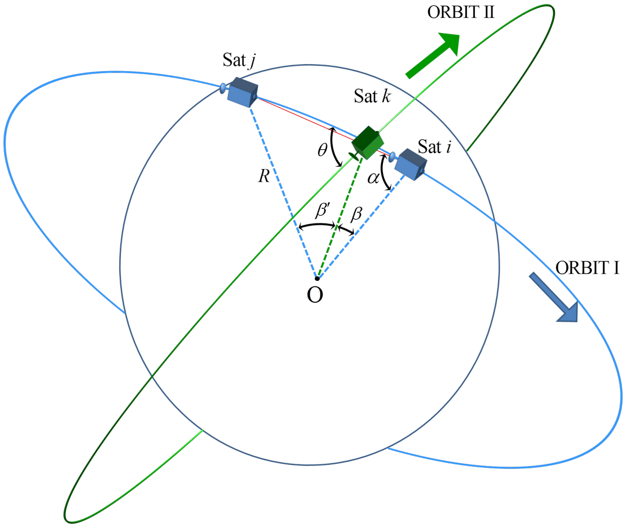

Figure 3.32: Geometry for ISL in the constellation

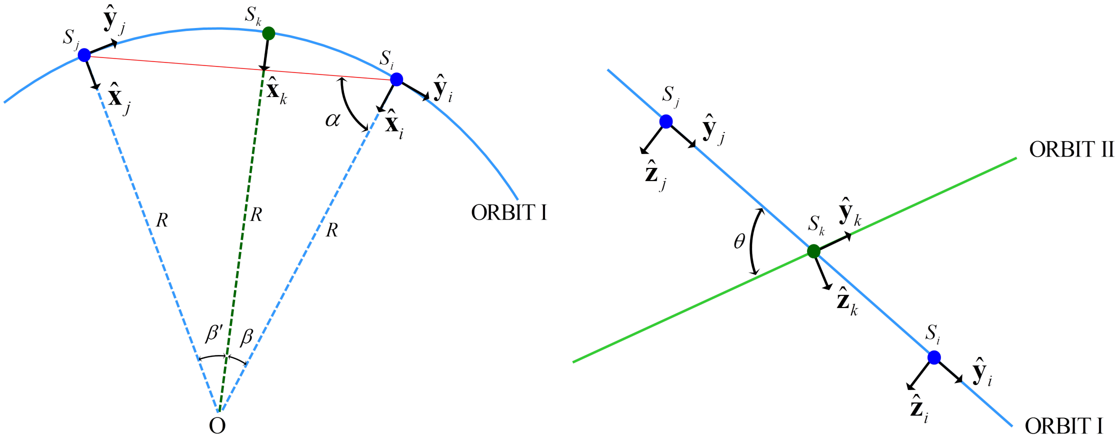

(a) View in $\hat{\boldsymbol{x}}_i$-$\hat{\boldsymbol{y}}_i$ plane

(b) View in $\hat{\boldsymbol{y}}$-$\hat{\boldsymbol{z}}$ plane

Figure 3.33: Geometry for intra-orbit and Inter-orbit ISL

3.4.2.3 Intra-Orbit ISL Angle

The geometry for intra-orbit ISL is illustrated in Fig. 3.33a. Considering isosceles triangle $\triangle OS_iS_j$, the intra-orbit ISL angle α is related to the angle between adjacent two satellites, S_i and S_j, in the orbit I as follows.

$$2\alpha = \pi - (\beta' + \beta) \tag{3.31}$$

Since the angle between adjacent two satellites, $\beta + \beta'$, is

$$\beta' + \beta = \frac{2\pi}{N_{so}} \tag{3.32}$$

then α becomes

$$\alpha = \frac{\pi}{2} - \frac{\pi}{N_{so}} \tag{3.33}$$

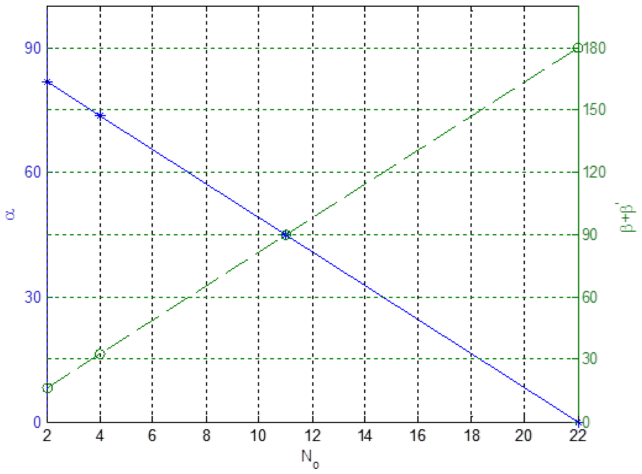

Figure 3.34: α and $\beta + \beta'$ vs N_o for $N_s = 44$ constellation

Figure 3.34 shows α and $\beta + \beta'$ as function of N_o. As N_o increases, α decreases whereas $\beta + \beta'$ increases.

3.4.2.4 Inter-Orbit ISL Angle

The inter-orbit ISL angle θ is defined as the angle between two orbital planes as illustrated in Fig. 3.33b.

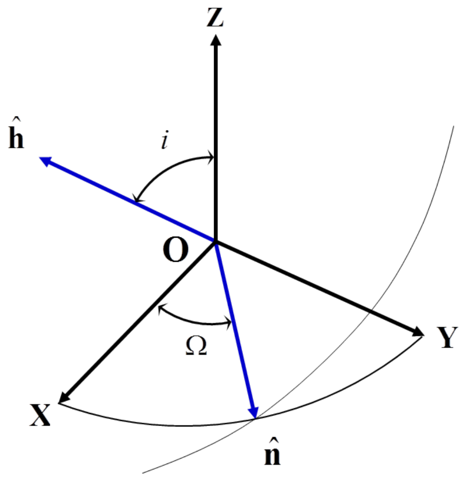

Figure 3.35: Orbital elements

In Fig. 3.35, $\hat{\boldsymbol{n}}$ and $\hat{\boldsymbol{h}}$ are node and angular momentum vectors of the orbit in the constellation, respectively. Considering constellations with circular orbits and same orbit inclination, we obtain angular momentum vectors of i-th orbit and k-th orbit in the constellation as follows.

$$\hat{\boldsymbol{h}}_i = \begin{Bmatrix} \sin i \sin \Omega_i \\ -\sin i \cos \Omega_i \\ \cos i \end{Bmatrix} \qquad \text{and} \qquad \hat{\boldsymbol{h}}_k = \begin{Bmatrix} \sin i \sin \Omega_k \\ -\sin i \cos \Omega_k \\ \cos i \end{Bmatrix} \tag{3.34}$$

where i and Ω are the inclination and the right ascension of the ascending node of the orbit, respectively.

The cosine of the angle, θ, between two vectors is found by scalar product. Since $\hat{\boldsymbol{h}}_i \cdot \hat{\boldsymbol{h}}_k = \cos\theta$

then

$$\begin{aligned}\cos\theta &= \cos^2 i + \sin^2 i(\sin\Omega_i \sin\Omega_k + \cos\Omega_i \cos\Omega_k) \\ &= \cos^2 i + \sin^2 i \cos\Delta\Omega\end{aligned} \tag{3.35}$$

θ is given by

$$\theta = \cos^{-1}\left(\cos^2 i + \sin^2 i \cos\frac{2\pi}{N_o}\right) \tag{3.36}$$

Figure 3.36 shows θ provided by Eq. (3.36) in terms of i and N_o.

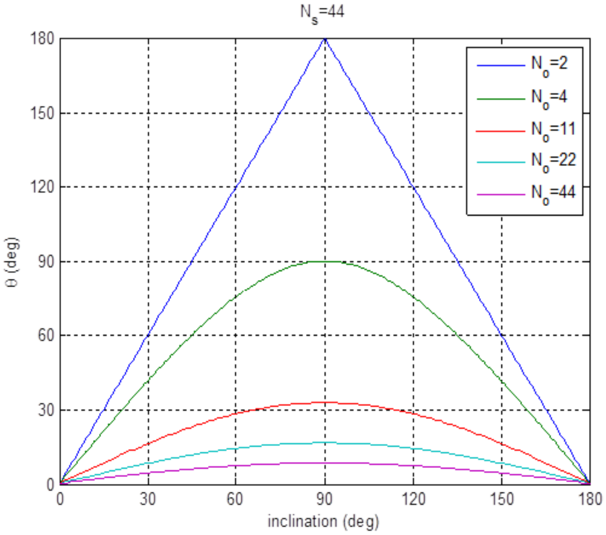

Figure 3.36: θ vs inclination for $N_s = 44$ constellation

3.4.2.5 Communication Time for Inter-Orbit ISL

Figure 3.37 shows the geometry of communication time for inter-orbit ISL where λ_1, λ_2 and λ_3 are angular lengths of the sides of the triangle (in radians) and γ is inter-orbit azimuth.

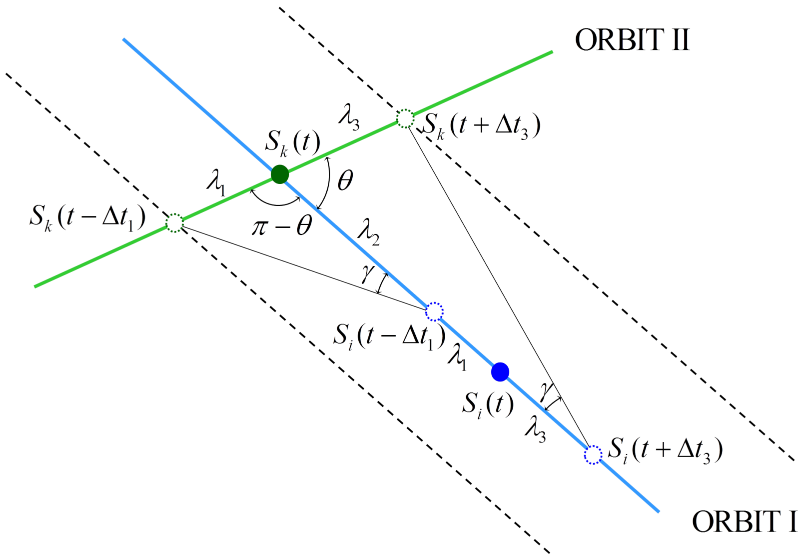

Figure 3.37: Communication time for inter-orbit ISL

Applying spherical trigonometry to two spherical triangles $\triangle S_k(t-\Delta t_1)S_k(t)S_i(t-\Delta t_1)$ and $\triangle S_k(t)S_k(t+\Delta t_3)S_i(t+\Delta t_3)$ gives us

$$\frac{\sin(\theta-\gamma)}{\sin\lambda_2}=\frac{\sin\gamma}{\sin\lambda_1} \qquad \text{and} \qquad \frac{\sin(\pi-\theta-\gamma)}{\sin(\lambda_1+\lambda_2+\lambda_3)}=\frac{\sin\gamma}{\sin\lambda_3} \tag{3.37}$$

Considering $\beta'+\lambda_1+\lambda_2=\frac{2\pi}{N_{so}}$ and Eq. (3.37), λ_1 and λ_3 can be identified as

$$\lambda_1=f(\theta,\gamma,N_{so},\beta') \qquad \text{and} \qquad \lambda_3=f(\theta,\gamma,N_{so},\beta') \tag{3.38}$$

Communication time can be obtained by

$$\lambda = n\Delta t \tag{3.39}$$

where $n = \sqrt{\mu/a^3}$ is the mean motion, and $\mu = 3.986 \cdot 10^5 \mathrm{km}^3/\mathrm{s}^2$ is the Earth's gravitational constant [15].

Since θ is depend on i and N_o, communication time can be written as

$$\Delta t = f(i, \gamma, N_{so}, \beta') \tag{3.40}$$

Figure 3.38 shows the communication time for inter-orbit ISL.

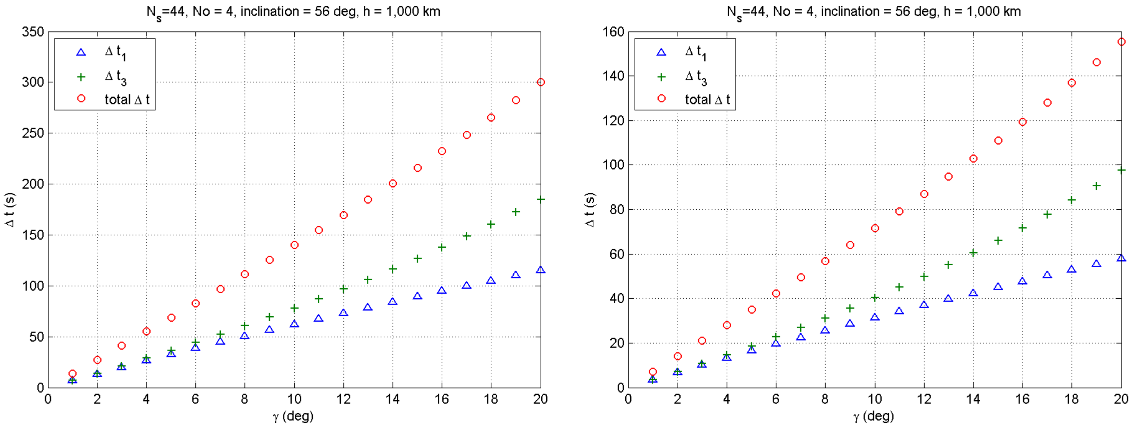

(a) Case I: $\beta = 2\beta'$ (b) Case II: $2\beta = \beta'$

Figure 3.38: Communication time for inter-orbit ISL

Figure 3.38b indicates that $\gamma \geq 9°$ is required to provide communication time for more than 1 minute. In case of low RF link, γ greater than 9° is achieved by beamwidth. A rule of thumb for estimating the beamwidth is given by [88]

$$3 \text{ dB beamwidth} = 70(\lambda/D)(\text{degrees}) \tag{3.41}$$

where λ is the wavelength and D is the antenna diameter. The beamwidth is usually measured between 3 dB points because gain falls off rapidly beyond them [89]. When RF beam forms a cone-type beam, the size and shape of a cone-type beam is depending on height of the satellite and the performance of the antenna. However, optical link requires antenna steering because of the narrowness of beam.

3.4.2.6 Analysis of Global Connectivity

In the constellation, the relative position of two adjacent satellites in the same orbit is steady. However, the relative position of two satellites in adjacent orbits varies. If the constellation can be connected by the ISL as a whole, the constellation provides global connectivity. Han, Gui and Li introduced the graph theory to the analysis of the global connectivity of ISL [90]. The adjacency matrix of graph theory is given by [91, 92]

$$A = \begin{bmatrix} a_{11} & a_{12} & \cdots & a_{1N_s} \\ a_{21} & a_{22} & \cdots & a_{2N_s} \\ \vdots & \vdots & & \vdots \\ a_{N_s1} & a_{N_s2} & \cdots & a_{N_sN_s} \end{bmatrix} \tag{3.42}$$

where N_s is the number of satellites in the constellation, and a_{ij} is connectivity between *i-th* transmitting satellite and *j-th* receiving satellite. All elements of the adjacency matrix are either 0 or 1. In case of bi-directional communication the adjacency matrix is symmetric. The adjacency matrix can be used to determine connectivity of ISL as follows.

1. Evaluation of the matrix $R = A + A^2 + \cdots + A^{N_s - 1}$

2. The necessary and sufficient condition for the connectivity (any satellite is connected to any other) is that all elements of the matrix R are not zero. In particular the value of R_{ij} tells you how many different way the i and j satellites can be linked.

Since intra-orbital ISL maintain permanent connectivity between satellites on the same orbital plane, modified adjacency matrix considering only inter-orbital ISL can be used as follows.

$$M = \begin{bmatrix} m_{11} & m_{12} & \cdots & m_{1N_o} \\ m_{21} & m_{22} & \cdots & m_{2N_o} \\ \vdots & \vdots & & \vdots \\ m_{N_o1} & m_{N_o2} & \cdots & m_{N_oN_o} \end{bmatrix} \tag{3.43}$$

where N_o is the number of orbital planes in the constellation, and m_{ij} is connectivity between transmitting satellites in *i-th* orbital plane and receiving satellites in *j-th* orbital plane. Using modified adjacency matrix instead of original adjacency matrix reduces computational burden and enhances optimization performance. Evaluation of the matrix $R' = M + M^2 + \cdots + M^{N_o - 1}$ can easily determine the connectivity.

Investigating the geometry of constellation, topological periodicity of constellation is given by $\dfrac{T_p}{N_{so}}$. Consequently, evaluation for connectivity is required during only $\dfrac{T_p}{N_{so}}$.

3.4.3 Optimization

3.4.3.1 Fitness Function

As constellation design for the Earth observation using Genetic Algorithms, defining a fitness function to drive the optimization process is the key issue. The first fitness function is designed to minimize MRT. It has been implemented to root mean square of MRT of uniformly distributed points on the Earth. Thus, the optimality is defined by the minimization of the following function

$$L = \sqrt{\frac{1}{N}\sum_{i=1}^{N} x_i^2} \tag{3.44}$$

where x is the MRT for each point on the Earth. In the mathematical expression of the fitness function the parameters to be optimized are calculated in a set of N grid points distributed on the Earth surface.

Since lower elevation angle decreases quality of signal, the minimum grazing angle for observation is set to 8.2°. This minimum grazing angle is typical for this type of missions [93].

3.4.3.2 Ranges of Design Parameters

The ranges of design parameters are given in Table 3.10.

Table 3.10: Ranges of design parameters for optimization with N_s=44

Parameters	**Ranges**
$[N_o, N_{so}]$	[1,44] [2,22] [4,11] [11,4] [22,2] [44,1]
N_c	[1, N_o], integer
h (km)	[300,1500]
T_p (hr)	[1.51,1.93]
i (deg)	[0, 180]

3.4.4 Results

In this subsection a study applying the 2-D LFC theory has been done. In this simulation, the constellation was propagated with 5° steps in mean anomaly. The simulation results show that topological periodicity and dynamics of ISL is available and feasible.

3.4.4.1 Designed LFC

At an altitude of 1477.97 km above the Earth, 44 satellites are arranged in four orbital planes which are 57.88 ° inclined with reference to the equatorial plane. Eleven operational satellites are equally distributed by 32.72° in each orbital plane as illustrated in Fig. 3.39.

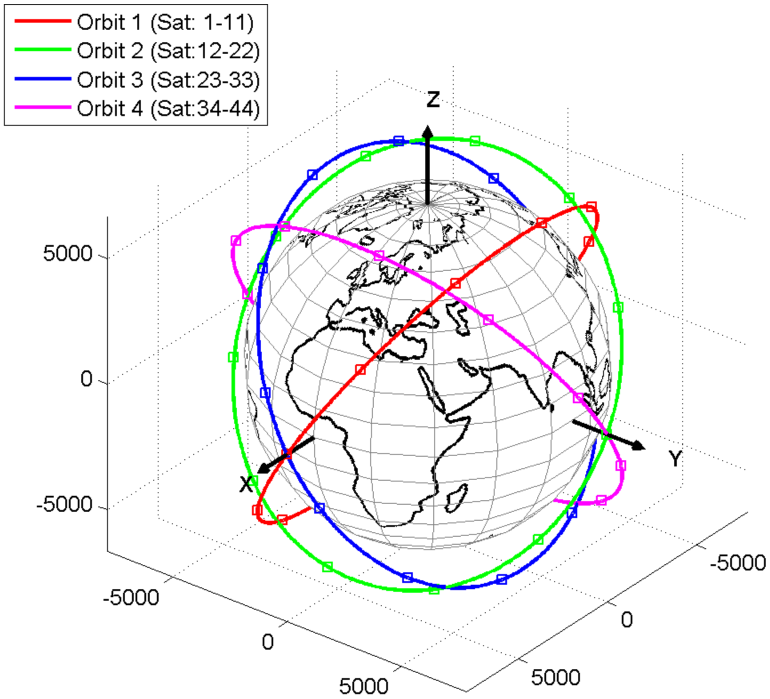

Figure 3.39: Designed constellation

Designed constellation can be entirely expressed with LFC parameters given in Table 3.11. The minimum distance of designed constellation is 632.18 km. Satellites do not approach one another within 632.18 km.

Table 3.11: LFC parameters of designed constellation

Parameters	Optimal values
$[N_o, N_{so}]$	[4,11]
N_c	0
h (km)	1477.97
T_p (hr)	1.92
i (deg)	57.88

Figure 3.40 illustrates the ISL topology of designed LFC at initial time. Solid lines denote the Intra-Orbit ISL and dashed lines denote Inter-Orbit ISL. With respect to observation, footprints of all satellites are visualized. Note that highly latitude and part of equatorial regions have not been covered.

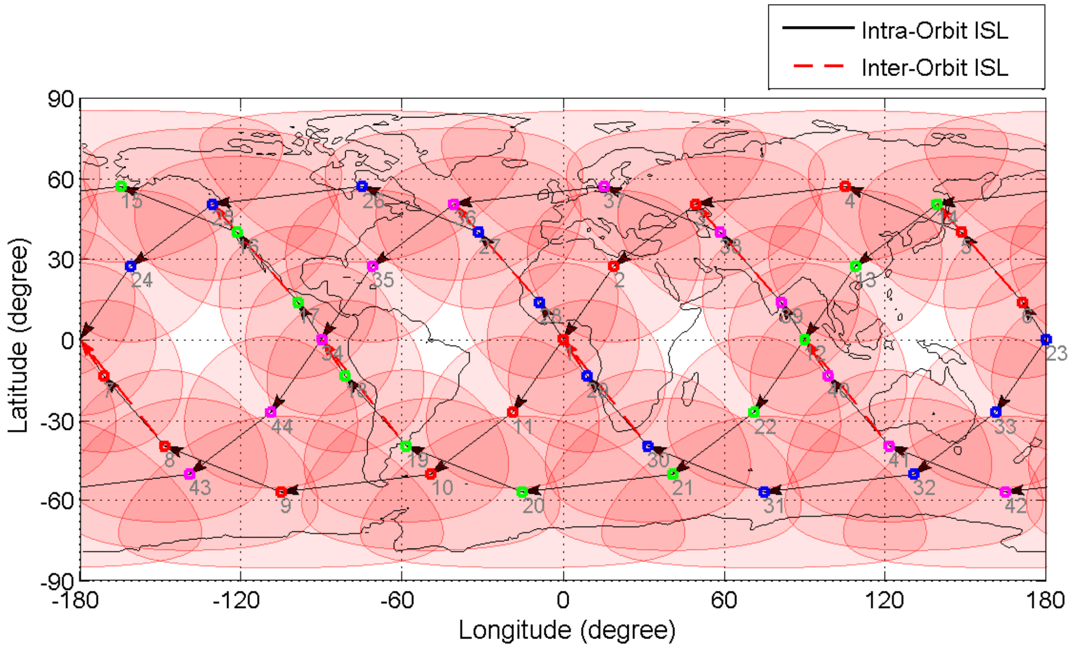

Figure 3.40: Designed constellation ISL topology at $t = 0$ (8.2° grazing angle)

3.4.4.2 Observational Performance

Figure 3.41 demonstrates simulation result of designed constellation in 1 day. Histogram shows the distribution of MRT in Fig. 3.41a. As shown in Fig. 3.41b, designed constellation provide very good observation performance in the most of regions except polar and equatorial areas.

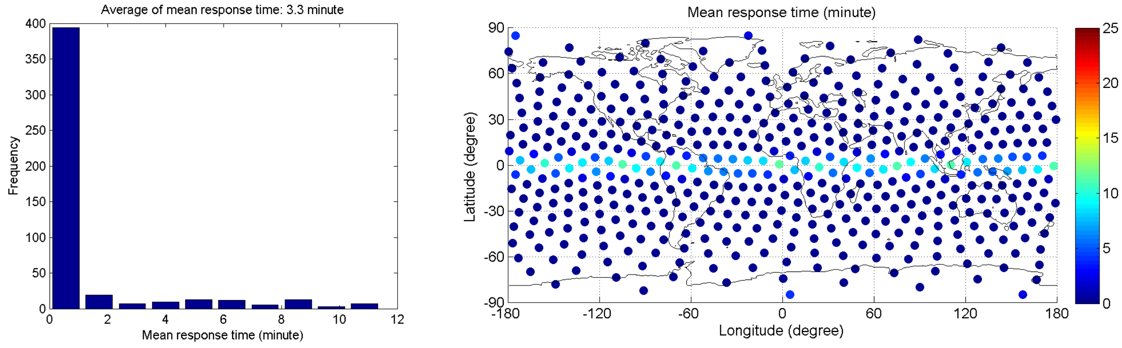

(a) (b)

Figure 3.41: Mean response time in 482 points

Figure 3.42 shows the distribution of MRT using 7, 682 points. Note that there are some unobserved points denoted unfilled circles in polar regions.

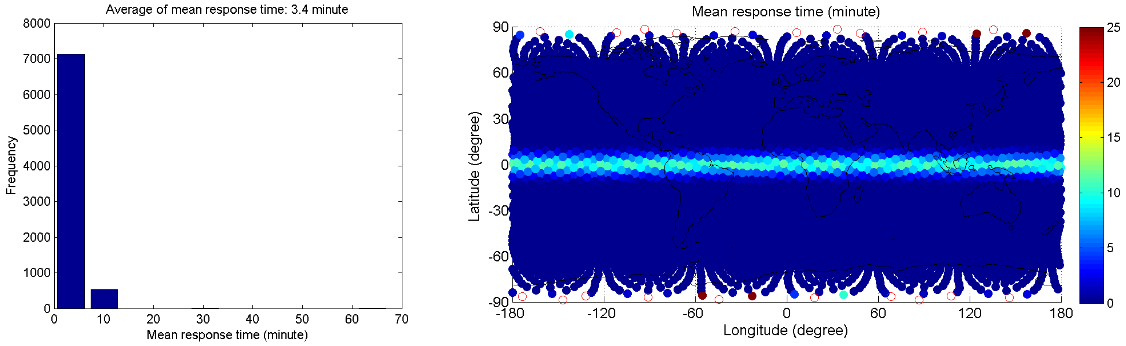

(a) (b)

Figure 3.42: Mean response time in 7, 682 points

3.4.4.3 Connectivity Analysis

This constellation guarantee continuous global connectivity. Time history of connectivity between orbits are repeated every $\frac{T_p}{N_{so}}$ as shown in Figure 3.43.

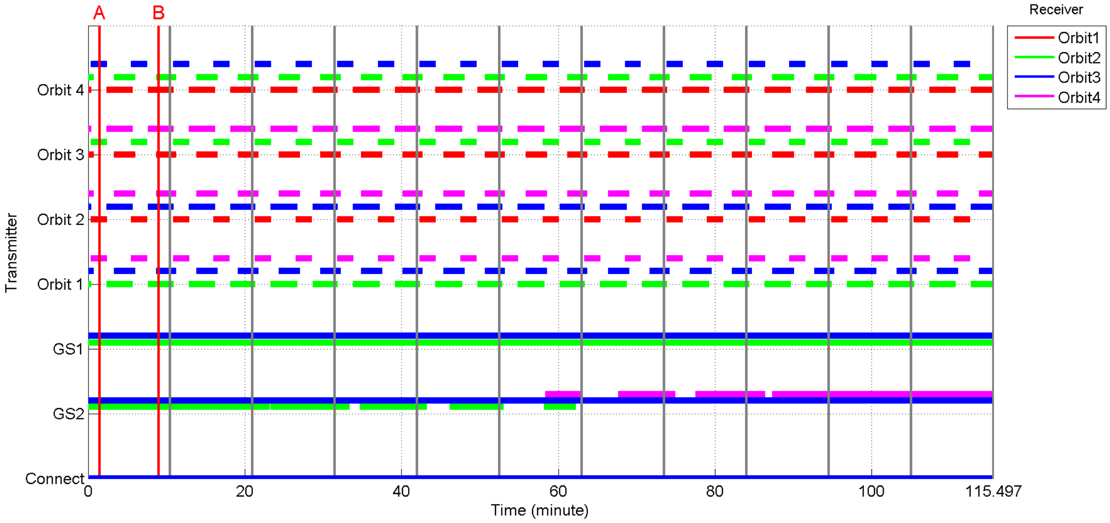

Figure 3.43: Time history of connectivity

The coordinates of the ground stations were (61.13°N, 149.54°W) and (61.13°N, 104.50°W). The simulation showed that within the orbital period the satellite is above at least one of the on-ground stations.

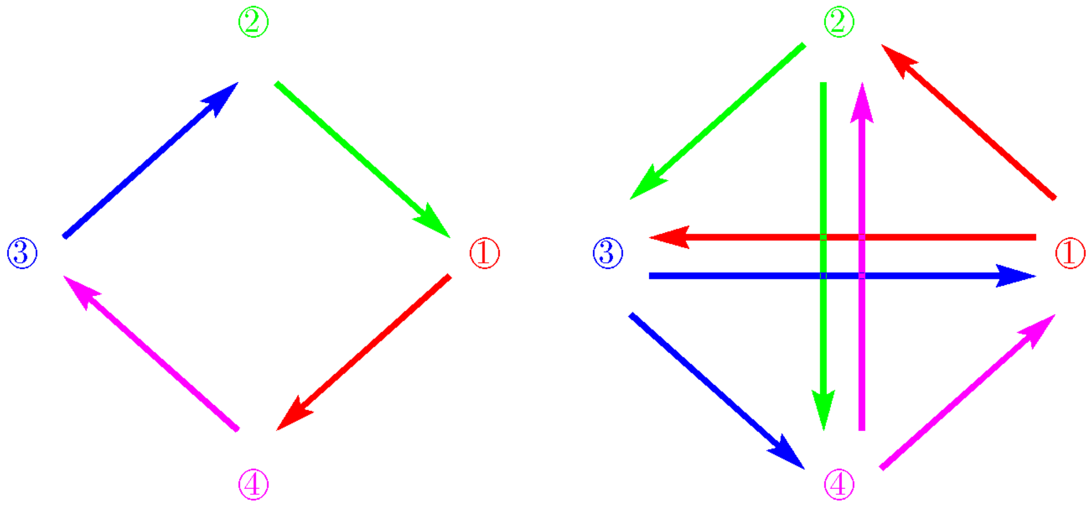

(a) Flow of information at time A (b) Flow of information at time B

Figure 3.44: Flow of information

3.4.5 Conclusions

In this work, we analyzed and designed constellations for the Earth observation mission with ISL. Before optimization process, the geometric characteristics of ISL have been investigated to check the feasibility of the system and find suitable values for inter-orbit azimuth, γ. The Genetic Algorithms technique with 2-D Lattice Flower Constellation theory has been used to find the best constellation for the mission. Optimal satellite constellation has been found by minimizing mean response time with global continuous connectivity and minimum distance constraint. We propose the fast and efficient algorithm using the modified adjacency matrix based on the graphic theory, which can simplify the evaluation of connectivity through investigating only Inter-Orbit ISL. In order to perform the optimization process efficiently, mean response time based on quasi-uniform distribution points has been evaluated. It has been found that the proposed constellation provides good observational performance with global continuous connectivity.

4. J_2-PROPELLED ORBITS AND CONSTELLATIONS*

4.1 Introduction

During the past decades, substantial efforts have been dedicated to minimize the fuel consumption for station-keeping maneuvers due to the orbital perturbations [94, 95, 96]. For Medium Earth Orbits (MEOs) and Low Earth Orbits (LEOs) the most important effect is caused by oblateness of the Earth [5]. The gravitational term describing the Earth's oblateness, known as the J_2 term, is the second zonal harmonic coefficient of the Earth's gravitational field series expansion [97, 98, 99]. Since the terms contributed by higher-order zonal, sectorial, and tesseral harmonics are thousand times smaller than J_2, except for special circumstances such as geosynchronous orbit [100], for LEOs and MEOs, it is sufficient to consider the J_2 effect for many space missions [101].

Molniya and Tundra orbits are located at critical 63.4° (prograde) or 116.6° (retrograde) inclinations to obtain no rotation of the perigee in the orbital plane. On the contrary, sun-synchronous orbits use the J_2 effect to obtain a nodal regression rate that matches the Earth's mean motion, so that the orbital plane is rigid with respect to the direction of the sun's light [102].

Compatible orbits (also called resonant orbits or repeating ground track orbits) have been extensively studied [103, 104, 105, 106, 81]. Compatible orbits are usually proposed to periodically repeat a three-dimensional trajectory in an Earth-Centered Earth-Fixed (ECEF) reference frame. At first approximation, a compatible orbit is built by synchronizing the orbital period with the Earth's rotational period. This

---

*Part of this chapter is reprinted with permission from "J_2-Propelled Orbits and Constellations" by Daniele Mortari, Martín Eugenio Avendaño Gonzales, and Sanghyun Lee, 2014. *Journal of Guidance, Control, and Dynamics*, Vol.37, No.5 (2014), pp. 1701–1706. Copyright © 2014 by Daniele Mortari, Martín Eugenio Avendaño Gonzales, and Sanghyun Lee.

kind of orbit is useful for Earth-referenced missions such as Earth observation, as it allows specific Earth locations to be periodically observed.

In this research, a shifting perspective is considered: the focus is not at the synchronization of the satellite with the Earth's rotation but at the synchronization of the orbit motion (due to the J_2 perturbation) in inertial space as well as in ECEF reference frame. In other words, the dynamic of the orbit and not the dynamic of the satellite is considered here. This study analyzes a new class of orbits called "J_2-Propelled", for which dynamics are periodic in the inertial frame and/or in the Earth rotating frame [107]. Motivation of developing these kinds of orbits originates from the need to design orbits for which the natural dynamics (J_2 is here used as "propellant") provides access to a wide three-dimensional space (between perigee and apogee radii) to measure physical quantities. The onboard fuel of the satellite is then limited to compensate the non J_2 perturbations, that are usually smaller for MEOs and LEOs.

This chapter is organized as follows: In Section 4.2, the linear J_2 perturbation model is briefly outlined, whereas in Section 4.3 compatibility condition is formulated in terms of perturbation to define compatible orbits. Section 4.4 presents the J_2-propelled orbits for the two cases of circular and elliptical orbits, and then the additional compatibility with the Earth's rotation is considered in Section 4.5 which present the Earth-compatible J_2-propelled orbits. Finally, conclusions and some examples are provided in Section 4.6.

4.2 Linear J_2 Perturbation

The J_2 gravitational perturbation on the orbital elements can be averaged over one orbital period. These averages highlight whether or not the orbital elements experience persistent (secular) changes. In particular, the average effects on the semi-major axis (a), eccentricity (e), and orbit inclination (i) orbital elements are [108] $\frac{da}{dt} \approx 0$, $\frac{de}{dt} \approx 0$, and $\frac{di}{dt} \approx 0$, while the right ascension of the ascending node (Ω) and the argument of perigee (ω) are linearly changing according to

$$\begin{aligned} \frac{d\omega}{dt} &= \frac{3}{4} J_2 \left(\frac{R_\oplus}{p}\right)^2 n \left(5\cos^2 i - 1\right), \quad \text{and} \\ \frac{d\Omega}{dt} &= -\frac{3}{2} J_2 \left(\frac{R_\oplus}{p}\right)^2 n \cos i \end{aligned} \tag{4.1}$$

where $R_\oplus = 6,378.137$ km (World Geodetic System 1984, WGS-84) is the Earth's radius, $p = a(1 - e^2)$ is the orbital semi-parameter, $J_2 \approx 1.08263 \cdot 10^{-3}$ is the second zonal harmonic coefficient (non-dimensional) of the Earth gravitational field, $n = \sqrt{\frac{\mu}{a^3}}$ is the mean motion, and $\mu = 3.98600441 \cdot 10^5 \text{km}^3/\text{s}^2$ is the Earth's gravitational constant [14, 15].

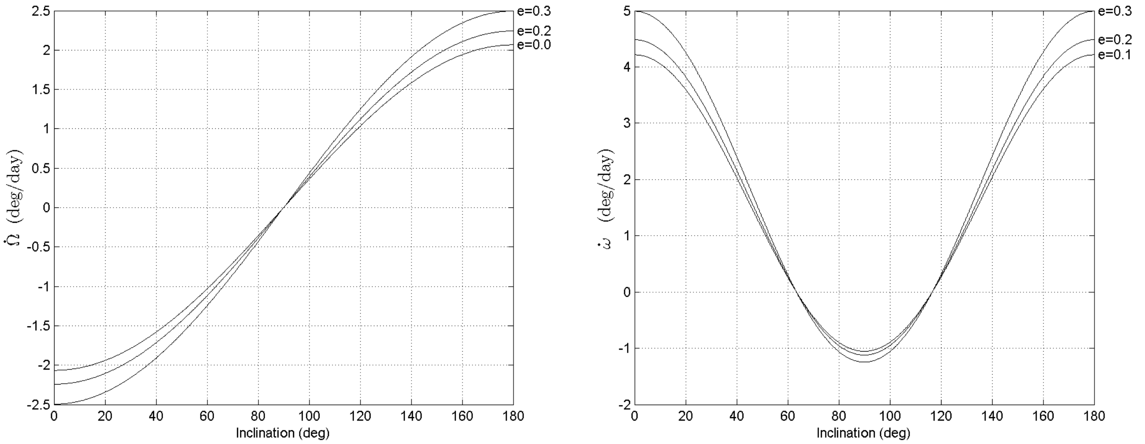

(a) Nodal regression rate

(b) Perigee rotation rate

Figure 4.1: Nodal regression (left) and perigee rotation (right) rates for $a = 10,000$ km and and some values of eccentricity.

Equation (4.1) shows that nodal regression rate, $\dot{\Omega}$, and perigee rotation rate,

$\dot{\omega}$, depend only on the semi-major axis, eccentricity, and inclination. To provide quantitative insight of Eq. (4.2), the $\dot{\Omega}$ and $\dot{\omega}$ values are provided in Figs. 4.1a and 4.1b for an orbit with $a = 10,000$ km and for various values of eccentricity. The absolute values of $\dot{\Omega}$ and $\dot{\omega}$ increase as the eccentricity increases under the fixed semi-major axis (same orbital period). In particular, node lines move clockwise for orbital inclinations lower than 90°, and counter-clockwise for inclinations greater than 90°. $\dot{\Omega}$ is maximum for equatorial orbits (where the node line is not defined!) and no nodal regression occurs for polar orbits, as shown in Fig. 4.1a.

The nodal regression can be compensated by a proper selection of the semi-major axis while the perigee rotation rate cannot be compensated the same way. As shown in Fig. 4.1a the perigee rotation is eliminated at the two critical inclinations, $i = 63.4°$ and $i = 116.6°$. Note that the perigee moves counterclockwise if $i < 63.4°$ or $i > 116.6°$, and clockwise for $63.4° < i < 116.6°$.

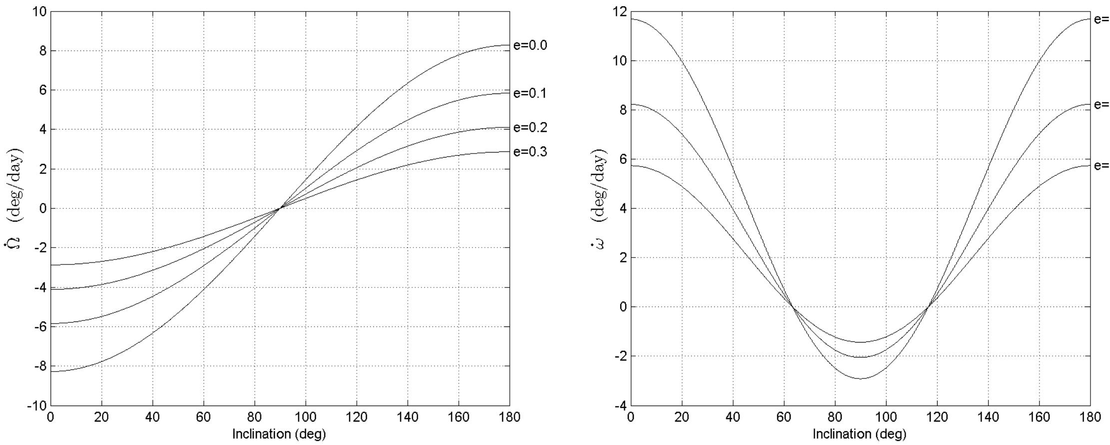

(a) Nodal regression rate

(b) Perigee rotation rate

Figure 4.2: Nodal regression (left) and perigee rotation (right) rates for 350 km perigee altitude and some values of eccentricity.

Figures 4.2a and 4.2b illustrate $\dot{\Omega}$ and $\dot{\omega}$ versus inclination for an orbit of which perigee altitude is maintained fixed at 350 km and for various values of eccentricity. Nodal regression is zero for polar orbits and greatest for orbits of which inclination is 0° or 180° . Note that the absolute values of $\dot{\Omega}$ and $\dot{\omega}$ decrease as the eccentricity increases.

Even if higher-order analytical theories for J_2-perturbed motion have been developed [109, 110], the theory presented in this study is kept linear to provide a simple way for initial design of orbits and/or constellations as, for accurate design, all perturbations must be considered (third body, solar pressure, drag, etc).

4.3 Compatible Orbits

Based on Eqs. (4.1) Carter [111] defined the condition for a satellite to "repeat" the ground track. This condition involves synchronizing the *orbit nodal period* (time between two subsequent equator crossings in ascending node, T_n) with the *nodal period of Greenwich* (time for Greenwich longitude to cross the orbit ascending node line, T_g)

$$N_n\, T_n = N_n\, \frac{2\pi}{n + \dot{\omega}} = N_g\, T_g = N_g\, \frac{2\pi}{\omega_\oplus - \dot{\Omega}} \tag{4.2}$$

where $N_n \in \mathbb{Z}$ and $N_g \in \mathbb{Z}$ are two positive coprime integers and $\omega_\oplus \approx 7.292 \cdot 10^{-5}$rad/s is the Earth's rotation rate. Equation (4.2) is not correct for elliptical orbits. While the nodal period of Greenwich, $\dfrac{2\pi}{\omega_\oplus - \dot{\Omega}}$, is consistently defined (the angles $\omega_\oplus \Delta t$ and $\dot{\Omega}\Delta t$ are both longitudinal variations) the orbit nodal period, $\dfrac{2\pi}{n + \dot{\omega}}$, is correct just for circular orbits because the angle $n\Delta t$ is a variation of mean anomaly while the angle $\dot{\omega}\Delta t$ is a variation of true anomaly. Adding n with $\dot{\omega}$ makes sense for circular orbits, only. However, Eq. (4.2) provides sufficiently approximated solutions for small eccentric orbits where the difference between variations of true and mean anomalies are small.

Orbits for which nodal period satisfy Eq. (4.2) are called *compatible* or *resonant*[*] with respect the Earth.

4.4 Compatible J_2-Propelled Orbits

According to Eq. (4.1) the linear J_2 effect rotates the orbit around the angular momentum direction and simultaneously, around the Earth's spin axis. The two angular velocities defined in Eq. (4.1) can be synchronized through a *compatibility* equation

$$N_\omega \, T_\omega = N_\omega \, \frac{2\pi}{\dot\omega} = N_\Omega \, T_\Omega = N_\Omega \, \frac{2\pi}{\dot\Omega}, \tag{4.3}$$

where $N_\omega \in \mathbb{Z}$ and $N_\Omega \in \mathbb{Z}$ are two co-prime integers ($N_\omega \perp N_\Omega$). The values of N_ω and N_Ω can be negative integers as $\dot\omega$ and $\dot\Omega$ can also be negative. Orbits satisfying Eq. (4.3) are called "J_2-propelled orbits." The dynamics of these orbits are periodic in the inertial reference frame.

To derive potential reasonable values for N_ω and N_Ω, consider the ratio between $\dot\Omega$ and $\dot\omega$. Since the J_2-propelled orbits satisfy $N_\Omega \, \dot\omega = N_\omega \, \dot\Omega$, then for a specific orbit inclination the $\dot\Omega / \dot\omega$ ratio provides us the possibility of quick estimating the admissible values for N_Ω and N_ω, especially when an approximate repetition time is provided. This ratio, which is independent from eccentricity, is

$$\frac{\dot\Omega}{\dot\omega} = \frac{2 \, \cos i}{1 - 5 \cos^2 i} \tag{4.4}$$

and its plot and the plot of the inverse are provided in Fig. 4.3. Note that to satisfy Eq. (4.3), polar ($\cos i = 0$) and critically inclined ($5 \cos^2 i = 1$) orbits must be avoided as they make $\dot\Omega = 0$ and $\dot\omega = 0$, respectively.

---

[*] The "repeating ground track" concept has it's own limitations as *any* two completely different equatorial orbits have the same ground track. More appropriate would be the concept of "repeating space track" indicating the repetition of a three-dimensional trajectory.

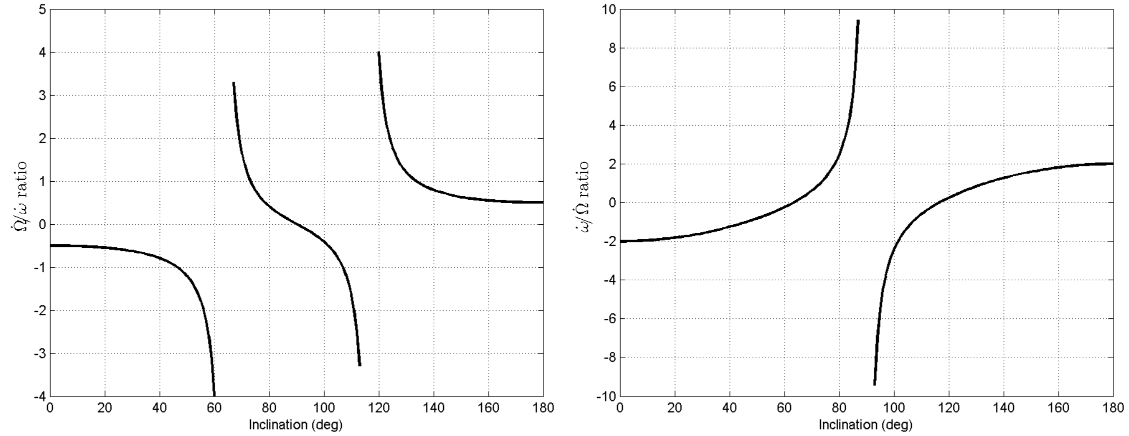

(a) $\dot\Omega/\dot\omega$ ratio vs inclination

(b) $\dot\omega/\dot\Omega$ ratio vs inclination

Figure 4.3: $\dot\Omega/\dot\omega$ and $\dot\omega/\dot\Omega$ ratios

Substituting Eq. (4.4) in Eq. (4.3) the relationship, $N_\Omega\,(5\cos^2 i - 1) + 2N_\omega\,\cos i = 0$, which is quadratic in term of $\cos i$, is obtained. The two solutions are

$$\cos i = \frac{-N_\omega \pm \sqrt{N_\omega^2 + 5N_\Omega^2}}{5N_\Omega}. \tag{4.5}$$

Not all combinations of N_Ω and N_ω satisfy Eq. (4.5) as $\cos i \in [-1, +1]$ also must be satisfied. To satisfy the inclination bounds a simple analysis yields to the two following cases:

- If $N_\omega \geq -2N_\Omega$ or $N_\omega \geq +2N_\Omega$, then

  $$\cos i = \frac{-N_\omega + \sqrt{N_\omega^2 + 5N_\Omega^2}}{5N_\Omega}$$

  is an admissible solution.

- If $N_\omega \leq -2N_\Omega \quad \text{or} \quad N_\omega \leq +2N_\Omega$, then

$$\cos i = \frac{-N_\omega - \sqrt{N_\omega^2 + 5N_\Omega^2}}{5N_\Omega}$$

  is an admissible solution.

This implies that, depending on the $[N_\Omega, N_\omega]$ values, three distinct cases are obtained:

1) Only the positive root is admissible.

2) Only the negative root is admissible.

3) Both roots are admissible.

Equation (4.5) can be written as

$$\pm \cos i = \frac{-x + \sqrt{x^2 + 5}}{5} \tag{4.6}$$

where $x = \dfrac{N_\omega}{|N_\Omega|}$ is a rational number. Therefore symmetric solutions exist for direct and retrograde inclinations as shown in Fig. 4.4.

An interesting case is a J_2-propelled orbit satisfying $N_\omega = N_\Omega = 1$. From the compatibility condition this orbit can be considered "equivalent" to the GEO orbit for which the resonant (compatible) integers are $N_p = N_\oplus = 1$. Retrograde and prograde orbits satisfying $N_\omega = N_\Omega = 1$ can even be designed with the additional synchronization with the Earth's rotation, as shown in the next section.

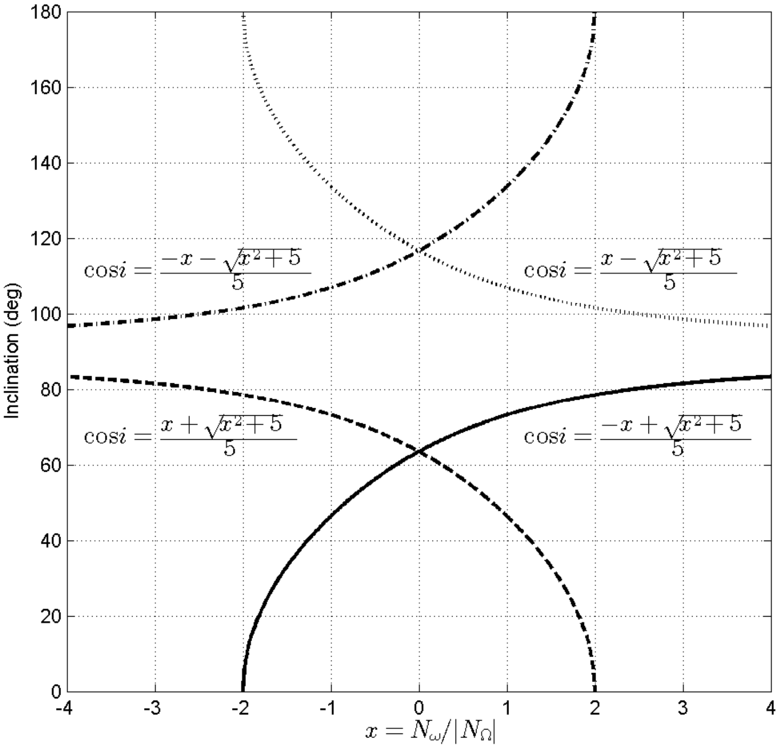

Figure 4.4: Orbit inclination for $N_\omega/|N_\Omega|$

4.5 Earth-Compatible J_2-Propelled Orbits

Equation (4.3) can be further constrained to be Earth-compatible, that is, with the additional synchronization with Earth's rotation. In this case two compatibility equations need to be satisfied

$$N_\omega T_\omega = N_\Omega T_\Omega = N_\oplus T_\oplus \tag{4.7}$$

where $T_\oplus$ is the Earth sidereal period, $N_\oplus \in \mathbb{Z}$, and the integers must satisfy the co-prime properties, $N_\omega \perp N_\oplus$, $N_\omega \perp N_\Omega$, and $N_\Omega \perp N_\oplus$. These conditions avoid obtaining same solution by using a different set of integers, N_ω, N_Ω, and $N_\oplus$. An orbit satisfying Eq. (4.7) is called "Earth-Compatible J_2-propelled." In the next two subsections the two specific cases of circular and elliptical Earth-Compatible J_2-propelled orbits are presented, respectively.

4.5.1 Circular Orbits

For circular orbits ($e = 0$), Eq. (4.7) simply becomes

$$N_\Omega \, T_\Omega = N_\oplus \, T_\oplus \tag{4.8}$$

as the perigee is not defined and, consequently, the rotation of apse line has no meaning. For circular orbits the semi-parameter, semi-major axis, and radius are all equal, $a = p = R$. Therefore, substituting the second of Eq. (4.1) into Eq. (4.8), the relationship

$$N_\Omega = -\frac{3 \, J_2 \, N_\oplus R_\oplus^2 \sqrt{\mu}}{2\omega_\oplus R^{7/2}} \cos i \tag{4.9}$$

is obtained. Figure 4.5 shows the solutions provided by Eq. (4.9) in terms of inclination vs orbit altitude by setting $N_\Omega \in [-1, -2, 1, 2]$ and for $N_\oplus = 90$ and $N_\oplus = 150$. The altitude was bounded to 2,400 km as the J_2 perturbation, provided by Eq. (4.1), strongly decreases with altitude.

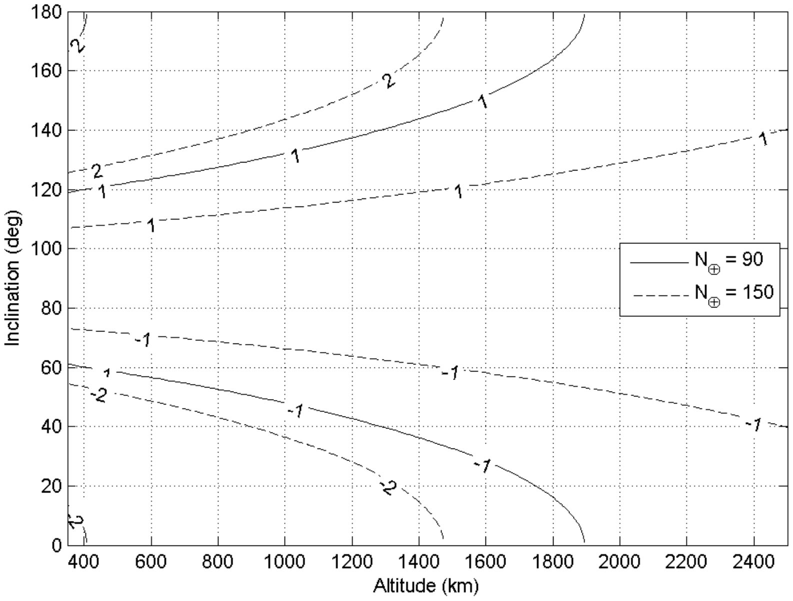

Figure 4.5: Circular orbits: inclination vs altitude for various values of N_Ω

Figure 4.6 shows the solutions provided by Eq. (4.9) in terms of inclination vs orbit altitude by setting $N_\oplus$ to values ranging from 90 to 190 with 20 as step size and for $N_\Omega = -1$ (associated with prograde orbits) and $N_\Omega = +1$ (for retrograde orbits), respectively.

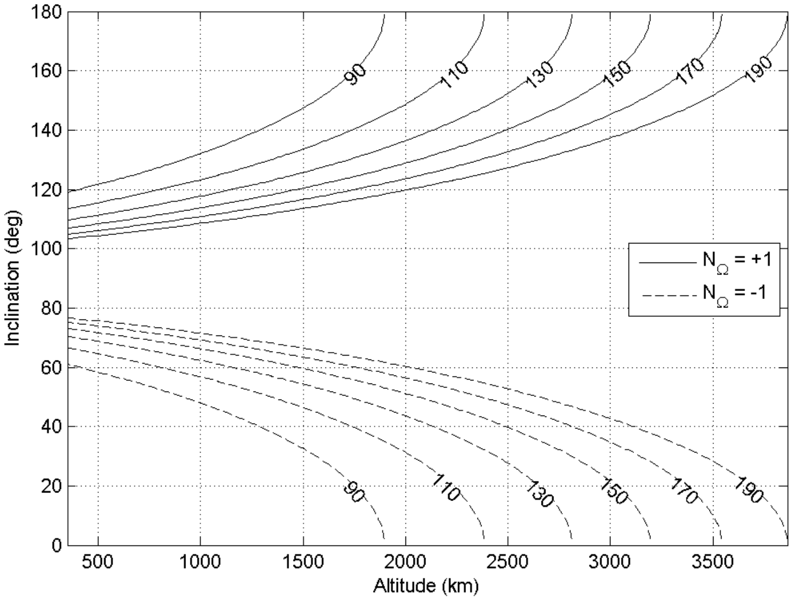

Figure 4.6: Circular orbits: inclination vs altitude for various values of $N_\oplus$

4.5.2 Elliptical Orbits

The elliptical Earth-Compatible J_2-propelled orbits must satisfy the double compatibility condition provided in Eq. (4.7). The first compatibility equation, $N_\Omega \, T_\Omega = N_\omega \, T_\omega$, implies that Eq. (4.3) must be satisfied. In addition, Eq. (4.8) must also be satisfied. To eliminate multiple solutions, all three compatibility integers must be coprime, $N_\Omega \perp N_\oplus$, $N_\omega \perp N_\oplus$, and $N_\Omega \perp N_\omega$. For the elliptical case, Eq. (4.8) becomes

$$N_\Omega = -\frac{3 \, J_2 \, N_\oplus R_\oplus^2 \sqrt{\mu}}{2\omega_\oplus a^{7/2}(1-e^2)^2} \cos i \tag{4.10}$$

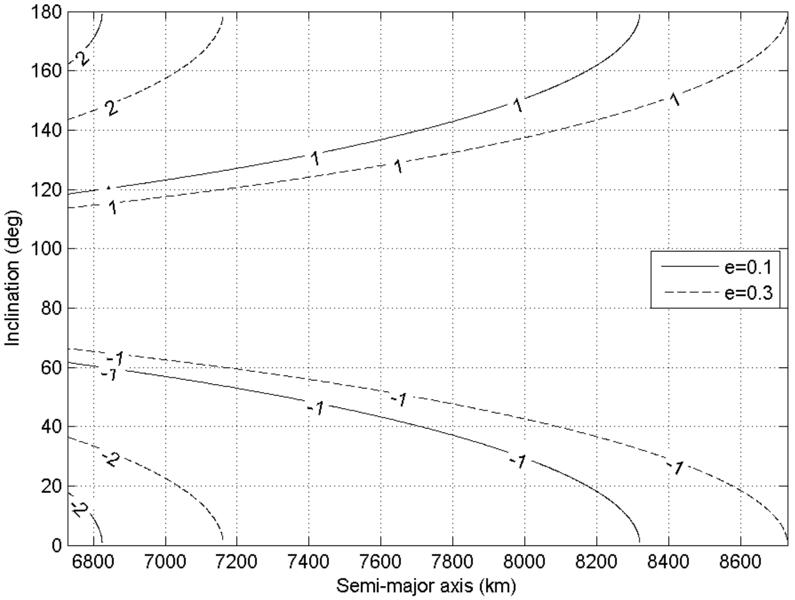

Figure 4.7: Elliptical orbits: inclination vs semi-major axis for various values of N_Ω and $N_\oplus = 90$

Figure 4.7 shows the solutions provided by Eq. (4.10) in terms of inclination versus semi-major axis for $e = 0.1$ and 0.3, respectively. These two figures clearly show that negative values of N_Ω are associated with prograde orbits while positive values with retrograde orbits. Obviously, by changing sign to $N_\oplus$ the negative values of N_Ω will be associated with retrograde orbits while positive values with prograde orbits.

In Eq. (4.10) "$\cos i$" can be replaced by the expression given in Eq. (4.5). Two equations are then obtained depending on the sign selected in Eq. (4.5). These two equations can be identified as

$$f^+(N_\Omega, N_\omega, N_\oplus, a, e) = 0 \qquad \text{and} \qquad f^-(N_\Omega, N_\omega, N_\oplus, a, e) = 0, \tag{4.11}$$

where f^+ indicates the equation obtained by using the positive solution of Eq. (4.5) in Eq. (4.10) while f^- represents the equation obtained using the negative solution.

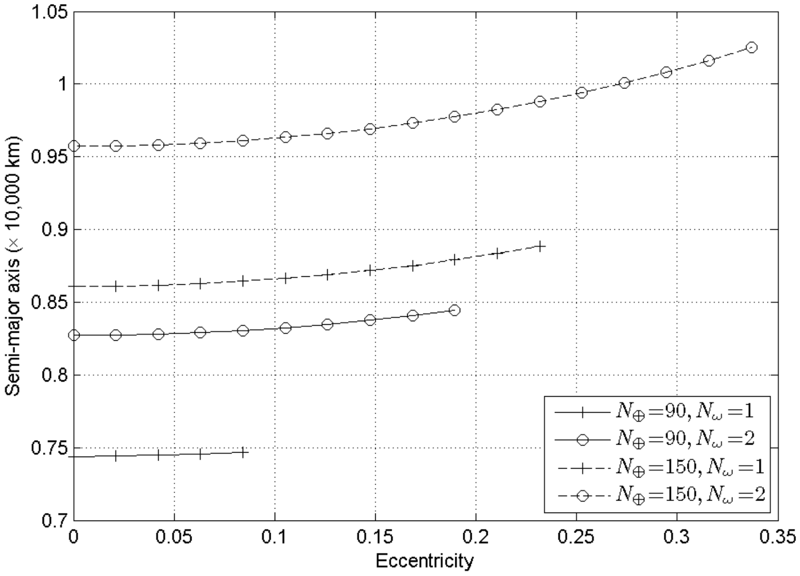

Figure 4.8: Solutions of Eq. (4.11) f^- for various values of N_ω and $N_\Omega = 1$

Note that when using the positive solution of Eq. (4.5), positive values of N_Ω are associated with prograde orbits while negative values of N_Ω are associated with retrograde orbits, as already shown in Fig. 4.4. These results are incompatible with the results provided by Fig. 4.7. This means that f^- can only provide solutions for positive values of $N_\oplus$. Figure 4.8 provides solutions of f^- for various values of N_ω and $N_\oplus = 90, 150$.

Figures 4.9 and 4.11 show examples of "Earth-Compatible J_2-propelled" orbits. For specific values of N_Ω, N_ω, $N_\oplus$, and e, Eq. (4.5) provides the admissible value of inclination. Then, a is obtained by Eq. (4.10). In these figures, the results are plotted in an Earth Centered Inertial (ECI) coordinate frame and the stars and circles markers indicate apogee and perigee, respectively.

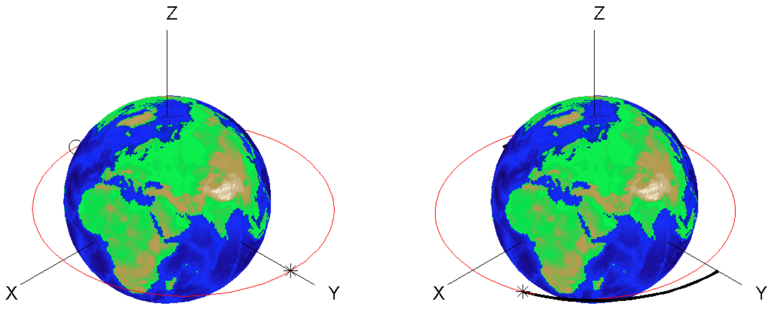

(a) 0 day

(b) 25 days

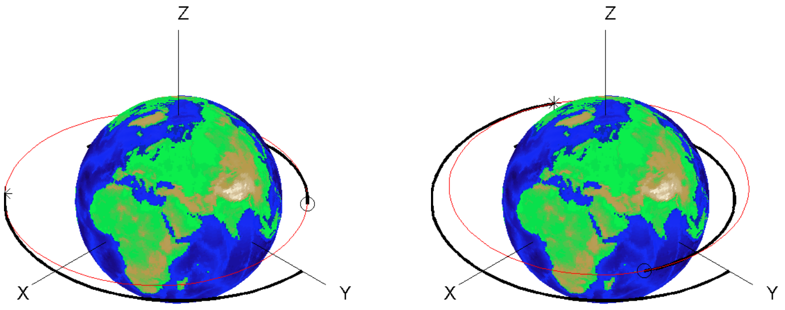

(c) 50 days

(d) 75 days

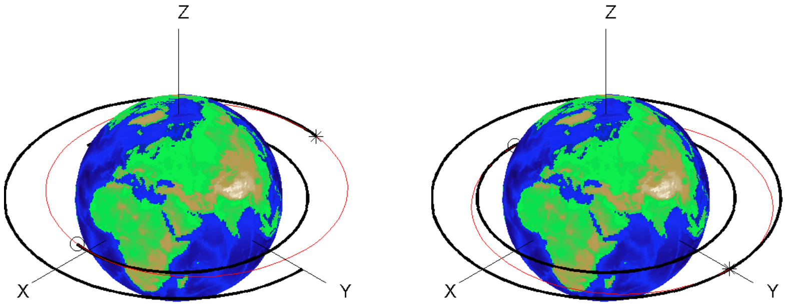

(e) 100 days

(f) 130 days

Figure 4.9: $N_\Omega = 1$, $N_\omega = 2$, $N_\oplus = 130$, $e = 0.15$, $i = 180$, $a = 9,309$ km

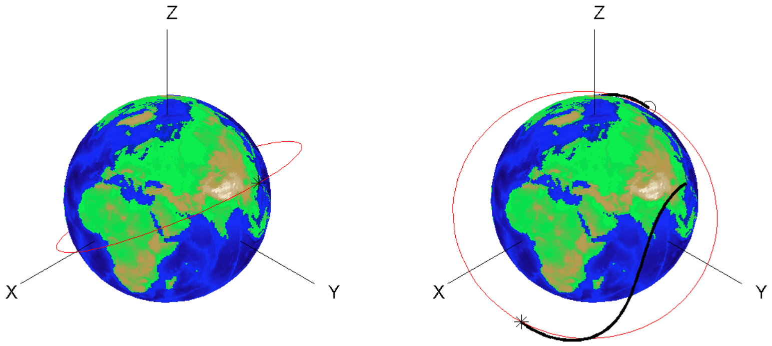

(a) 0 day (b) 40 days

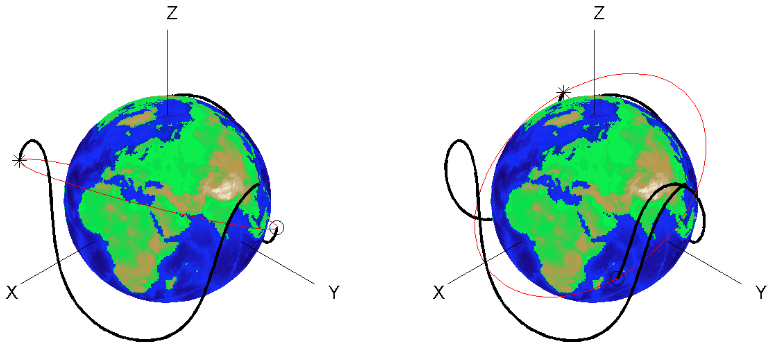

(c) 80 days (d) 120 days

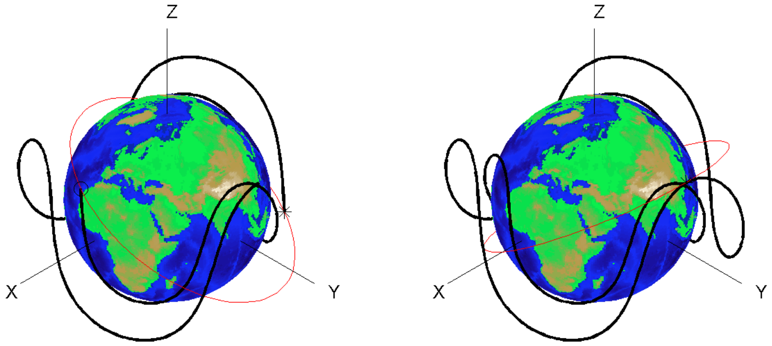

(e) 160 days (f) 200 days

Figure 4.10: $N_\Omega = 2$, $N_\omega = 3$, $N_\oplus = 200$, $e = 0.15$, $i = 147$, $a = 8,212$ km

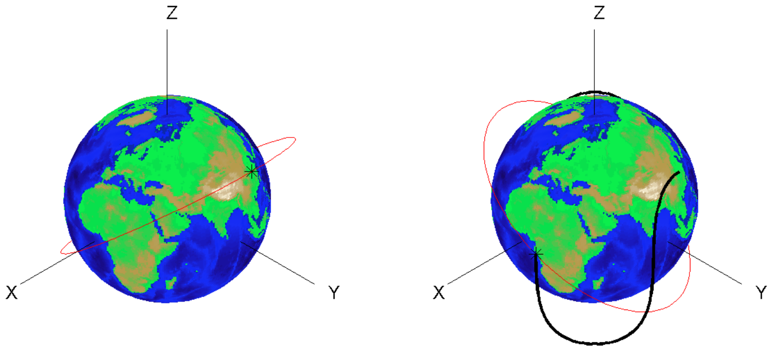

(a) 0 day (b) 60 days

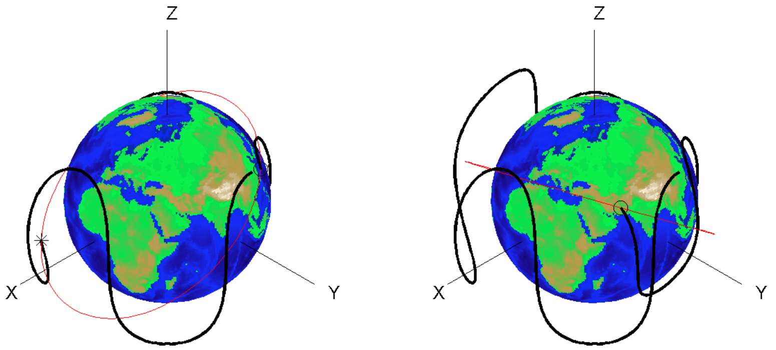

(c) 120 days (d) 180 days

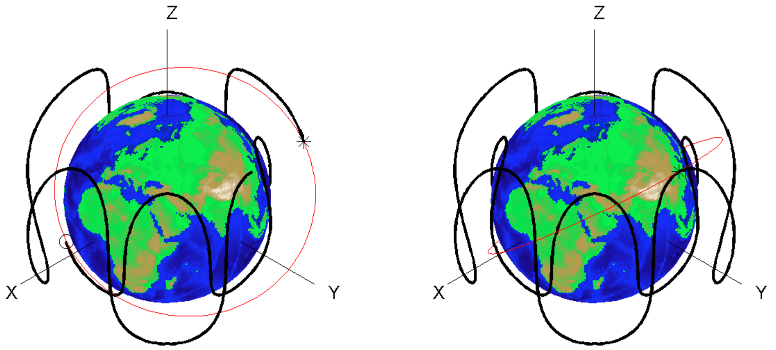

(e) 240 days (f) 300 days

Figure 4.11: $N_{\Omega} = 3$, $N_{\omega} = 4$, $N_{\oplus} = 300$, $e = 0.15$, $i = 142$, $a = 8,066$ km

4.5.3 Constellations Using J_2-Propelled Orbits

The proposed elliptical J_2-propelled orbits are particularly suitable to be adopted in the 3-D Lattice Theory of Flower Constellations (FC) [16, 12], which extends the 2-D Lattice Theory [11] by including the J_2 perturbation. Important characteristics of the Lattice Theory of Flower Constellation are as follows:

1) It is a minimum-parameter design tool (no equivalency problem)
2) The theory is independent from compatibility condition (free to use any orbit). From a mathematical point of view the satellites phasing is described by a regular lattice on a three-dimensional torus (each axis is an angle, modulo 2π) in a four-Dimensional space.

Since the 2-D Lattice Theory does not include the J_2 perturbation, from a practical point of view it can be used for circular orbits or orbits at critical inclinations ($i = 63.4^\circ$ or $i = 116.6^\circ$) only, as the J_2 effect will slowly destroy the initial optimal configuration and the station keeping cost will quickly becomes expensive. While the variation of Ω can be compensated by a proper selection of the orbital period (this variation is identical for all orbits, and consequently it won't destroy the symmetric distribution) the ω variation changes the latitudinal locations of perigee/apogee with catastrophic departure from the initial optimal configuration. Trying to keep the perigee in his location is known to be very expensive.

The main idea of the 3-D Lattice Theory is again *to use, rather than to fight*, the J_2 effect. By placing on the same orbital plane orbits with identical shape that are uniformly distributed in ω due to the first of Eq. (4.1) a uniform rotation of these orbits on the same orbital plane is obtained, and this plane is rotating about the Earth spin axis due to second of Eq. (4.1). In particular, the satellites phasing in the 3-D Lattice Theory is described by

$$\begin{bmatrix} N_o & 0 & 0 \\ N_{c3} & N_{oo} & 0 \\ N_{c1} & N_{c2} & N_{so} \end{bmatrix} \begin{Bmatrix} \Omega_{ikj} \\ \omega_{ikj} \\ M_{ikj} \end{Bmatrix} = 2\pi \begin{Bmatrix} i-1 \\ k-1 \\ j-1 \end{Bmatrix} \bmod (2\pi) \tag{4.12}$$

where N_o is the number of orbital planes, N_{oo} the number of orbits per orbital plane, N_{so} the number of satellites per orbit, $i \in [1, N_o]$, $j \in [1, N_{so}]$, $k \in [1, N_{oo}]$, and $N_{c1} \in [1, N_o]$, $N_{c2} \in [1, N_{oo}]$, and $N_{c3} \in [1, N_o]$ are three integers (called configuration numbers) identifying the satellite phasing. In Eq. (4.12), the indices have the following meaning: the "i, k, j" satellite indicates that it belongs to the j-th mean anomaly location of the k-th orbit belonging to the i-th orbital plane. Again, the importance of this theory consists of extending the constellation design to the use of elliptical orbits at *any inclination* under the linear J_2 effect. This would be perfect to accommodate J_2-propelled constellations.

4.6 Conclusions

A linear theory to design orbits and constellations where the Earth oblateness perturbation, the J_2 perturbation, generates dynamics that are periodic in inertial or in rotating (Earth) frame is presented. In these orbits, called "J_2-propelled orbits," the linear (secular) J_2 effect *is used instead of being fought* to allow the satellites accessing specific three-dimensional volumes around the Earth. Equations to derive the orbital parameters are provided to obtain specific dynamics. Main motivations is to design space missions (satellites and constellations) able to measure (or to monitor) physical quantities (e.g., magnetic or electric fields) in large space volumes by limiting the control costs to compensate the other gravitational and non-gravitational orbital perturbations, only.

Two “J_2-propelled orbits” are proposed. The first one synchronizes the J_2 effect of the rotation of the apse line with the nodal precession of the orbital plane, while the second adds the further synchronization with the Earth’s rotation. Finally, the paper shows that the J_2-propelled orbits can be straightforwardly extended to J_2-propelled constellations using the 3-D Lattice theory of flower constellation, which is also briefly summarized, and for which the application belongs to future work.

5. CONCLUSIONS AND FUTURE WORKS

This chapter summarizes all the findings and conclusions of each chapter and suggests future works.

5.1 Conclusions

In this dissertation, three tasks are accomplished.

First, these works provide the quasi-equal area subdivision algorithm based on equal area spherical subdivision to obtain approximated solutions to the problem of uniform distribution of points on a 2-dimensional sphere, known as Smale's seventh problem. The algorithm provides quasi-equal area triangles by splitting the Platonic solids into subsequent spherical triangles of identical areas. The main feature of the proposed algorithm is that adjacent triangles share common vertices that can be merged. It allows for reshaping of the final triangles in order to remove obtuse triangles. The proposed algorithm is fast and efficient for generating a large number of points. Consequently, they are suitable for various applications requiring high value of N. The proposed algorithms are then applied to two geographical data distributions that are modeled by quasi-uniform distribution of weighted points.

Second, guidelines for designing a constellation of satellites using the Lattice Flower Constellations design theory have been presented. The problem of finding the optimal parameters for various missions have been addressed. Since the fitness function and constraints for optimization mainly depends on the mission objectives, the mission analysis have been performed from a geometric point. Optimization is performed using Genetic Algorithms to estimate the constellation, subject to specific mission constraints. The resulting constellations have been explored from the mission performance perspective, and demonstrate the effectiveness of the proposed approach to estimate the best design parameters for the considered missions.

Third, the linear J_2 orbital perturbation model is used to obtain orbits whose dynamics are periodic in the inertial frame and also in the Earth rotating frame. These orbits are here called "J_2-propelled" and "Earth-compatible J_2-propelled," respectively. The main advantage of these orbits is that they repeatedly cover specific volumes around the gravitational body. Therefore, low orbital maintenance costs are required to compensate the non-J_2 orbital perturbations. It is demonstrated that the J_2-propelled orbits can be straightforwardly extended to J_2-propelled constellations using the 3-D Lattice theory of flower constellation.

5.2 Future Work

Further work needs to be performed in the regional application such as regional navigation satellite system. While global missions such as global navigation have been explored to a certain extent, regional applications of Lattice Flower Constellations have not yet been fully exploited. The non-uniform constellations maybe would provide additional benefits for regional missions. Since the Lattice Flower Constellations theory is particularly efficient for global coverage due to the uniformity of satellite distribution, it is not possible to design asymmetric constellations. However, Lattice Flower Constellation theory with Necklace theory, a special area of number theory, can provide asymmetric constellations. It can be applied to design constellations with redundancy to consider satellite failures.

REFERENCES

[1] Wertz, J. R., editor, *Mission Geometry; Orbit and Constellation Design and Management*, Space Technology Library, Microcosm Press, El Segundo, CA, renewed edition ed., 2009.

[2] Finkelstein, S. and Sanford, S., "Learning from Corporate Mistakes: The Rise and Fall of Iridium," *Organizational Dynamics*, Vol. 29, No. 2, 2000, pp. 138–148.

[3] Monte, P. A. and Turner, A. E., "Constellation selection for globalstar, a global mobile communications system," *in Proccedings of the AIAA International Communication Satellite Systems Conference and Exhibit*, 1992, pp. 1350–1360.

[4] Hofmann-Wellenhof, B., Lichtenegger, H., and Wasle, E., *GNSS-Global Navigation Satellite Systems GPS, GLONASS, Galileo & more*, Springer Wien New York, 2008.

[5] Wertz, J. R. and Larson, W. J., editors, *Space Mission Analysis and Design*, Kluwer Academic Publishers, Netherlands, 1999.

[6] Lüders, R., "Satellite Networks for Continuous Zonal Coverage," *American Rocket Society Journal*, Vol. 31, 1961, pp. 179–184.

[7] Lüders, R. and Ginsberg, L., "Continuous Zonal Coverage - A Generalized Analysis," *AIAA Mechanics and Control of Flight Conference*, Anaheim, CA, August 1974, pp. 1–13.

[8] Walker, J., "Some Circular Orbit Patterns Providing Continuous Whole Earth Coverage," *British Interplanetary Journal Society*, Vol. 24, 1971, pp. 369–384.

[9] Walker, J., "Continuous Whole-Earth Coverage by Circular Orbit Satellite

Patterns," Tech. Rep. 77044, Royal Aircraft Establishment, March 1977.

[10] Mortari, D. and Wilkins, M. P., "The Flower Constellation Set Theory Part I: Compatibility and Phasing," *IEEE Transactions on Aerospace and Electronic Systems*, Vol. 44, No. 3, July 2008, pp. 953–963.

[11] Avendaño, M. E., Davis, J. J., and Mortari, D., "The 2-D lattice theory of Flower Constellations," *Celestial Mechanics and Dynamical Astronomy*, Vol. 116, No. 4, 2013, pp. 325–337.

[12] Davis, J. J., Avendaño, M. E., and Mortari, D., "The 3-D Lattice Theory of Flower Constellations," *Celestial Mechanics and Dynamical Astronomy*, Vol. 116, No. 4, 2013, pp. 339–356.

[13] Avendaño, M. E., Mortari, D., and Davis, J. J., "The lattice theory of Flower Constellations," *Paper AAS 10-172 of the 20th AAS/AIAA Space Flight Mechanics Meeting*, San Diego, CA, February 2010, pp. 1093–1104.

[14] Vallado, D. A., *Fundamentals of Astrodynamics and Applications*, McGraw–Hill, New York, 1997.

[15] Standish, E. M., "Report of the IAU WGAS Sub-group on Numerical Standards," In Highlights of Astronomy, I. Appenzeller, ed. Dordrecht: Kluwer Academic Publishers, 1995.

[16] Davis, J. J., *Constellation Reconfiguration: Tools and Analysis*, Ph.D. thesis, Texas A&M University, 2010.

[17] Robinson, R., "Arrangement of 24 points on a sphere," *Mathematische Annalen*, Vol. 144, 1961, pp. 17–48.

[18] Berman, J. and Hanes, K., "Optimizing the arrangement of points on the unit sphere," *Mathematics of Computation*, Vol. 31, No. 140, 1977, pp. 1006–1008.

[19] Smale, "Mathematical Problems for the Next Century," *Mathematical Intelligencer*, Vol. 20, 1998, pp. 7–15.

[20] Saff, E. and Kuijlaars, A., "Distributing many points on a sphere," *The Mathematical Intelligencer*, Vol. 19, 1997, pp. 5–11.

[21] Mortari, D., Avendaño, M., and Davalos, P., "Uniform Distribution of Points on a Sphere with Application in Aerospace Engineering," *Paper AAS 11-261 of the 21th AAS/AIAA Space Flight Mechanics Meeting*, New Orleans, LO, February 2011, pp. 2247–2260.

[22] Dragnev, P. D., Legg, D. A., and Townsend, D. W., "Discrete Logarithmic Energy on the Sphere," *Pacific Journal of Matehmatics*, Vol. 207, 2002, pp. 345–358.

[23] ONeill, E. and Laubscher, R., "Extended Studies of the Quadrilateralized Spherical Cube Earth Data Base," Tech. report 3-76, Computer Sciences Corp Silver Spring Md System Sciences Div, 1976.

[24] Snyder, J., "An Equal-Area Map Projection for Polyhedral Globes," *Cartographica*, Vol. 29, No. 1, 1992, pp. 10–21.

[25] Teanby, N., "An icosahedron-based method for even binning of globally distributed remote sensing data," *Computers & Geosciences*, Vol. 32, 2006, pp. 1442–1450.

[26] Massey, N., "Feature trackingonthehierarchicalequalareatriangularmesh," *Computers & Geosciences*, Vol. 44, 2012, pp. 42–51.

[27] Bronshtein, I. N., Semendyayev, K. A., Musiol, G., and Muehlig, H., *Handbook of Mathematics*, Springer-Verlag, Berlin, Heidelberg, 5th ed., 2007.

[28] Zwillinger, D., editor, *Standard Mathematical Tables and Formulae*, CRC Press, Inc., Boca Raton, FL, 31st ed., 2002.

[29] Popko, E. S., *Divided spheres : geodesics and the orderly subdivision of the sphere*, CRC press, 2012.

[30] Shub, M. and Smale, S., "Complexity of Bezout's theorem V: Polynomial

time," *Theoretical Computer Science*, Vol. 133, 1994, pp. 141–164.

[31] Rakhmanov, E. A., Saff, E. B., and Zhou, Y. M., "Minimal Discreter Energy on the Sphere," *Mathematical Research Letters*, Vol. 1, 1994, pp. 647–662.

[32] Chan, S., Samuels, A. T., Shah, N. B., Underwood, J. E., and de Weck, O. L., "Optimization of Hybrid Satellite Constellations using Multiple Layers and Mixed Circular-Elliptical Orbits," *22nd AIAA International Communications Satellite Systems Conference & Exhibit 2004*, Monterey, CA, May 2004.

[33] Park, K., Ruggieri, M., and Mortari, D., "Comparisons between GalileoSat and Global Navigation Flower Constellations," *2005 IEEE Aerospace Conference*, Big Sky, MT, March 2005, pp. 1516–1523.

[34] Lee, S. and Mortari, D., "2-D Lattice Flower Constellations for Radio Occultation Missions," *Frontiers in Aerospace Engineering*, Vol. 2, No. 2, 2013, pp. 79–90.

[35] Potter, P., Ramankutty, N., Bennett, E. M., and Donner, S. D., "Characterizing the Spatial Patterns of Global Fertilizer Application and Manure Production," *Earth Interactions*, Vol. 14, 2010.

[36] Center for International Earth Science Information Network (CIESIN)/Columbia University or International Earth Science Information Network (CIESIN)/Columbia University, and Centro Internacional de Agricultura Tropical (CIAT), "Gridded Population of the World: Future Estimates (GPWFE)," Palisades, NY: Socioeconomic Data and Applications Center (SEDAC), Columbia University. Available at http://sedac.ciesin.columbia.edu/gpw., 2005.

[37] D., G., *Genetic Algorithms in Search, Optimization and Machine Learning*, Addison-Wesley, Reading, MA, Reading, MA, 1989.

[38] Venkataraman, P., *Applied Optimization with MATLAB Programming*, John

Wiley & Sons, New York, 2002.

[39] Gallagher, K. and Sambridge, M., "Genetic Algorithms: A Powerful Tool for Large-scale Nonlinear Optimization Problems," *Computers & Geosciences*, Vol. 20, No. 7/8, 1994, pp. 1229–1236.

[40] Lee, S. and Mortari, D., "Improved uniform points on a sphere with application to any geographical data distribution," *Paper AAS 13-729 of the AAS/AIAA Astrodynamics Specialist Conference*, Hilton Head, SC, August 2013, pp. 431–446.

[41] Center for International Earth Science Information Network (CIESIN)/Columbia University, and Centro Internacional de Agricultura Tropical (CIAT), "Gridded Population of the World, Version 3 (GPWv3): Population Density Grid," Palisades, NY: NASA Socioeconomic Data and Applications Center (SEDAC), 2005.

[42] Center for International Earth Science Information Network (CIESIN)/Columbia University, and Centro Internacional de Agricultura Tropical (CIAT), "Country-level GDP and Downscaled Projections based on the A1, A2, B1, and B2 Marker Scenarios, 1990-2100, [digital version]," Palisades, NY: CIESIN, Columbia University. Available at http://www.ciesin.columbia.edu/datasets/downscaled. (date accessed), 2002.

[43] Jamalipour, A., *Low Earth Orbital Satellites for Personal Communication Networks*, Artech House, 1998.

[44] Young, M., Muntz, E., and Wang, J., "Maintaining Continuous Low Orbit Flight by Using In-Situ Atmospheric Gases for Propellant," *Rarefied Gas Dynamics: 22-nd International Symposium*, Sydney, Australia, July 2000.

[45] Speckman, L. E., Lang, T. J., and Boyce, W. H., "An Analysis of the Line of Sight Vector Between Two Satellites in Common Altitude Circular Orbits,"

AIAA/AAS Astrodynamics Conference, Portland, OR, August 1990, pp. 866–874.

[46] Yunck, T. P., "An Overview of Atmospheric Radio Occultation," *Journal of Global Positioning Systems*, Vol. 1, No. 1, 2002, pp. 58–60.

[47] Kursinski, E. R., Hajj, G. A., Schofield, J. T., Linfield, R. P., and Hardy, K. R., "Observing Earth's Atmosphre by Occultation Using Global Positioning System," *Journal of Geophysical Reasearch*, Vol. 102, No. 19, 1997, pp. 23,429–23,465.

[48] Melbourne, W., Davis, E., Duncan, C., Hajj, G. A., Hardy, K., Kursinski, E., Meehan, T., Young, L., and Yunck, T., "The Application of Spaceborne GPS to Atmospheric Limb Sounding and Global Change Monitoring," Tech. rep., JPL Publication 94-18, Jet Propulsion Laboratory, California Institute of Technology, Pasadena, CA, 1994.

[49] Bracewell, R. N., *The Fourier transform and its applications*, McGraw-Hill, NY, 1965.

[50] Liou, Y., Pavelyev, A., Matyugov, S., Yakovlev, O., and Wickert, J., *Radio Occultation Method for Remote Sensing of the Atmosphere and Ionosphere*, In-Tech, 2010.

[51] Fjeldbo, G. and Eshleman, V. R., "The Bistatic Radar-Occultation Method for the Study of Planetary Atmosphere," *Journal of Geophysical Research*, Vol. 70, No. 13, 1965, pp. 3217–3225.

[52] Fjeldbo, G. and Kliore, A. J., "The Neutral Atmosphere of Venus as Studied with the Mariner V Radio Occultation Experiments," *Astronomical Journal*, Vol. 76, No. 2, 1971, pp. 123–140.

[53] Liu, A. S., "On the Determination and Investigation of the Terrestrial Ionospheric Refractive Indices using GEOS-3/ATS-6 Satellite-to-Satetllite Tracking

Data," *Radio Science*, Vol. 13, No. 4, 1978, pp. 709–716.

[54] Ware, R., Exner, M., Feng, D., Gorbunov, M., Hardy, K., Herman, B., Kuo, Y., Meehan, T., Melbourne, W., Rocken, C., Schreiner, W., Sokolovskiy, S., solheim, F., Zou, X., Anthes, R., Businger, S., and Trenberth, K., "GPS Sounding of the Atmosphere from Low Earth Orbit: Preliminary Results," *Bulletin of the American Meteorological Society*, Vol. 77, No. 1, 1996, pp. 19–40.

[55] Wickert, J., Reigbe, C., Beyerle, G., Konig, R., Marquardt, C., Schmidt, T., Grunwaldt, L., Galas, R., Meehan, T. K., Melbourne, W. G., and Hocke, K., "Atmosphere Sounding by GPS Radio Occultation: First Results from CHAMP," *Geophysical Research Letters*, Vol. 28, No. 17, 2001, pp. 3263–3266.

[56] Wickert, J., Beyerle, G., Konig, R., Heise, S., Grunwaldt, L., Michalak, G., Reigber, C., and Schmidt, T., "GPS Radio Occultation with CHAMP and GRACE: A First Look at a New and Promising Satellite Configuration for Global Atmospheric Sounding," *Annales Geophysicae*, Vol. 23, 2005, pp. 653–658.

[57] Schaub, H. and Junkins, J. L., *Analytical Mechanics of Space Systems*, American Institute of American and Astronautics, Reston, VA, 2nd ed., 2009.

[58] Lawson, P. R., Lay, O. P., Johnston, K. J., Beichman, C. A., Unwin, S. C., and Martin et. al., S. R., "Terrestrial planet finder interferometer (TPF-I) whitepaper for the AAAC exoplanet task force," Tech. rep., NASA Jet Propulsion Labs, Pasadena, CA, April 2007.

[59] Hyland, D. C., Kim, H., Khussainov, D., Kim, M., and Quinn, J. P., "A Novel Design of an Exo-solar planet Imager," *50th AIAA Aerospace Sciences Meeting including the New Horizons Forum and Aerospace Exposition*, Nashville, TN, January 2012.

[60] Léna, P., Rouan, D., Lebrun, F., Mignard, F., and Pelat, D., *Observational*

Astrophysics, Springer, 3rd ed., 2012.

[61] Blanc, P., Falzon, F., and Thomas, E., "A new concept of synthetic aperture instrument for high resolution earth observation from high orbits," Tech. rep., DTIC Document, 2005.

[62] Stepp, L. M., Daggert, L. G., and Gillett, P. E., "Estimating the cost of extremely large telescopes," *Proceedings of SPIE–the international society for optical engineering*, Vol. 4840, 2003, pp. 309–321.

[63] McAlister, H. A., "The future of high angular resolution astronomy: Seeing the unseen," *Vistas in Astronomy*, Vol. 30, 1987, pp. 27–38.

[64] Young, J., Haniff, C., Buscher, D., Creech-Eakman, M., Payne, I., Jurgenson, C., and Romero, V., "The MROI's capabilities for imaging geosynchronous satellites," *Proceedings - SPIE the International Society for Optical Engineering*, 2012.

[65] Millard, L. D. and Howell, K. C., "Control of Interferometric SpaceSpace Arrays for (u,v) Plane Coveage in Multi-Body Regimes," *Journal of the Astronautical Sciences*, Vol. 56, January–March 2008, pp. 71–97.

[66] Ramirez, J. and Chakravorty, S., "Fuel-Efficient Interferometric Imaging Maneuvers in Near-Earth Orbit," *Journal of Gui*, Vol. 31, July–August 2008, pp. 1133–1144.

[67] Howell, K. C. and Millard, L. D., "Control of satellite imaging formations in multi-body regimes," *Acta Astronautica*, Vol. 64, 2009, pp. 554–570.

[68] Brown, R. H. and Twiss, R. Q., "A Test of a New Type of Stellar Interferometer on Sirius," *Nature*, Vol. 178, No. 4541, 1956, pp. 1046–1048.

[69] Brown, R. H. and Twiss, R. Q., "Interferometry of the Intensity Fluctuations in Light," *Proceedings of the Royal Society of London*, Vol. 242, No. 1230, 1957, pp. 300–324.

[70] M.E.J., G., “Point Arrays Having Compact, Non-Redundant Autocorrelations,” *Journal of the Optical Society of America*, Vol. 16, 1971, pp. 272–273.

[71] Hussein, I., Scheeres, D., and Hyland, D., “Interferometric Observatories in Earth Orbit,” *Journal of Guidance, Control and Dynamics*, Vol. 27, 2004, pp. 297–301.

[72] Tonetti, S., Hyland, D., and Mortari, D., “The Flower Formation Flying. Part II: Application,” *Paper AAS 08-186 of the AAS/AIAA Space Flight Mechanics Meeting*, Galveston, TX, January 2008, pp. 1317–1332.

[73] Tonetti, S., “Optimization of Flower Constellations: Applications in Global Navigation System and Space Interferometry,” *47th AIAA Aerospace Sciences Meeting Including The New Horizons Forum and Aerospace Exposition*, Orlando, FL, January 2009.

[74] Born, M. and Wolf, E., *Principles of optics: electromagnetic theory of propagation, interference and diffraction of light*, Cambridge university press, 1999.

[75] Rayleigh, L., “Investigations in optics, with special reference to the spectroscope,” *Philosophical Magazine*, Vol. 8, No. 49, 1876, pp. 261–274.

[76] Goodman, J. W., *Introduction to Fourier Optics*, McGraw-Hill Science/Engineering/Math, 1996.

[77] Chakravorty, S., Kabamba, P., and Hyland, D., “Modeling of Image Formation in Multi-Spacecraft Interferometric Imaging Systems,” *Journal of the Astronautical Sciences*, Vol. 53, No. 3, 2005, pp. 281–300.

[78] Monnier, J. D., “Optical interferometry in astronomy,” *Reports on Progress in Physics*, Vol. 66, 2003, pp. 789–857.

[79] Al-Twaijry, H. A., *Multi-spacecraft optimal interferometric imaging*, Ph.D. thesis, The Univeristy of Michigan, 2006.

[80] Carlo, P. M. D., Marano, G., Luca, G. F. D., LAbbate, M., Oricchio, D.,

Venditti, P., and Santovito, M. R., "Intersatellite link for Earth Observation Satellites constellation," *SpaceOps 2006 Conference*, Rome, Italy, June 2006.

[81] Vtipil, S. D. and Newman, B., "Determining an Earth Observation Repeat-Ground-Track Orbit for an Optimization Methodologys," *Journal of Spacecraft and Rockets*, Vol. 49, No. 1, 2012, pp. 157–164.

[82] Abdelkhalik, O., Mortari, D., and Park, K. J., "Satellite constellation design for earth observation," *Paper AAS 05–148 of the 2005 Space Flight Mechanics Meeting Conference*, Copper Mountain, CO, January 2005, pp. 711–719.

[83] Middlestead, R. W., LeLevier, R. E., and Smith, M. D., "Satellite Crosslink Communications Vulnerability in a Nuclear Environment," *IEEE Journal on Selected Areas in Communications*, Vol. 5, No. 2, 1987, pp. 138–145.

[84] Keller, H., Salzwedel, H., Schorcht, G., and Zerbe, V., "Geometric aspects of polar and near polar circular orbits for the use of intersatellite links for global communication," *Vehicular Technology Conference, 1998. VTC 98. 48th IEEE*, Vol. 1, 1998, pp. 199–203.

[85] Wang, J., Li, L., and Zhou, M., "Topological dynamics characterization for LEO satellite networks," *Computer Networks*, Vol. 51, 2007, pp. 43–53.

[86] Sebacher, K. S., Lambert, S. G., Pautler, J. A., and Carter, J. P., "Laser Crosslink Configurations for RF Satellite Communications Systems," *Military Communications Conference*, Vol. 1, IEEE, 1985.

[87] Miriampally, V. R. and R., K. C., "Intersatellite optical communication link a novel approach," *International Journal of Applied Engineering and Technology*, Vol. 3, 2013, pp. pp.1–8.

[88] Fortescue, P., Swinerd, G., and Stark, J., editors, *Spacecraft Systems Engineering*, Wiley, 2011.

[89] Pisacane, V. L., editor, *Fundamental of Space Systems*, Oxford University

Press, 2nd ed., 2005.

[90] Han, S., Gui, Q., and Li, J., "Analysis of the connectivity and robustness of inter-satellite links in a constellation," *Science China Physics, Mechanics and Astronomy*, Vol. 54, No. 6, 2011, pp. 991–995.

[91] Jungnickel, D., *Graphs, Networks and Algorithms*, Springer Publishing Company, Incorporated, 3rd ed., 2007.

[92] Gross, J. and Yellen, J., *Graph Theory and Its Applications*, CRC Press, Inc., 1999.

[93] Pratt, S. R., Raines, R. A. J., F., C. E., and Temple, M. A., "An Operational and Performance Overview of the IRIDIUM Low Earth Orbit Satellite System," *IEEE Communications Surveys and Tutorials*, Vol. 2, 1999, pp. pp.2–10.

[94] Hunziker, R. R., "Low-thrust Station Keeping Guidance for a 24-hour Satellite," *AIAA Journal*, Vol. 8, No. 7, 1970, pp. 1186–1192.

[95] Beigelman, I. and Gurfil, P., "Optimal fuel-balanced impulsive formationkeeping for perturbed spacecraft orbits," *Journal of guidance, control, and dynamics*, Vol. 31, No. 5, 2008, pp. 1266–1283.

[96] Wang, G. B., Meng, Y., Zheng, W., and Tang, G. J., "Artificial Frozen Orbit Control Scheme Based on J_2 Perturbation," *Science China Technological Sciences*, Vol. 53, 2010, pp. 3138–3144.

[97] Brouwer, D., "Solution of the Problem of Artificial Satellite Theory Without Drag," *Astronomical Journal*, Vol. 64, 1959, pp. 378–396.

[98] Bate, R. R., Mueller, D. D., Saylor, W. W., and White, J. E., *Fundamentals of astrodynamics*, New York: Dover Publications, Inc, 1971.

[99] Battin, R. H., *An introduction to the mathematics and methods of astrodynamics*, American Institute of American and Astronautics, 1999.

[100] Wertz, J. R., editor, *Orbit and Constellation Design and Management*, Micro-

cosm Press and Kluwer Academic Publishers, 2001, pp. 65–66.

[101] Abramson, M., Carter, D., Kolitz, S., McConnell, J., Ricard, M., and Sanders, C., "The design and implementation of drapers earth phenomena observing system (epos)," *AIAA space 2001 conference*, 2001.

[102] Fortescue, P., Stark, J., and Swinerd, G., editors, *Spacecraft Systems Engineering*, John Wiley & Sons Ltd., Chichester, West Sussex, England, 3rd ed., 2003.

[103] King, J. C., "Quantization and Symmetry in Periodic Coverage Patterns with Applications to Earth Observation," *The Journal of the astronautical sciences*, Vol. 24, No. 1, 1976, pp. 347–363.

[104] Lo, M. W., "The Perturbation of Ground Tracks of Periodic Orbits," *AIAA-90-2898 Astrodynamics Conference*, Portland, OR, August 1990.

[105] Abdelkhalik, O. and Mortari, D., "Two-way orbits," *Celestial Mechanics and Dynamic Astronomy*, Vol. 94, No. 4, April 2006, pp. 399–410.

[106] Vtipil, S. D. and Newman, B., "Determining an Efficient Repeat Ground Track Method for Earth Observation Satellites: For Use in Optimization Algorithms," *AIAA/AAS Astrodynamics Specialist Conference*, Toronto, Ontario Canada, August 2010.

[107] Mortari, D., Avendaño, M. E., and Lee, S., "J_2-Propelled Orbits and Constellations," *AIAA/AAS Astrodynamics Specialists Conference*, Minneapolis, MN, August 2012.

[108] Schaub, H. and Junkins, J. L., *Analytical mechanics of space systems*, American Institute of Aeronautics and Astronautics, Inc., Reston, VA, 2003.

[109] Lara, M. and Gurfil, P., "Integrable Approximation of J_2-perturbed Relative Orbits," *Celestial Mechanics and Dynamic Astronomy*, Vol. 114, No. 3, 2012, pp. 229–254.

[110] Martinusi, V. and Gurfil, P., "Solutions and Periodicity of Satellite Relative Motion Under Even Zonal Harmonics Perturbations," *Celestial Mechanics and Dynamic Astronomy*, Vol. 111, No. 4, 2011, pp. 387–414.

[111] Carter, D., "When is the Groundtrack Drift Rate Zero?" CSDL Memorandum ESD-91-020, 1991, Cambridge, MA: Charles Stark Draper Laboratory.

[112] Bruccoleri, C., *Flower Constellation Optimization and Implementation*, Ph.D. thesis, Texas A&M University, 2007.

APPENDIX A

THE LATTICE FLOWER CONSTELLATIONS VISUALIZATION TOOL

Original 2-D Lattice Flower Constellations Visualization Tool “Ikebana” is important LFC demonstrator programmed in Java by Dr Martín E. Avendaño. Ikebana is designed to be an interactive simulation application. However, it is an extremely lightweight program to show LFC in a limited 3-D display as illustrated in Fig. A.1.

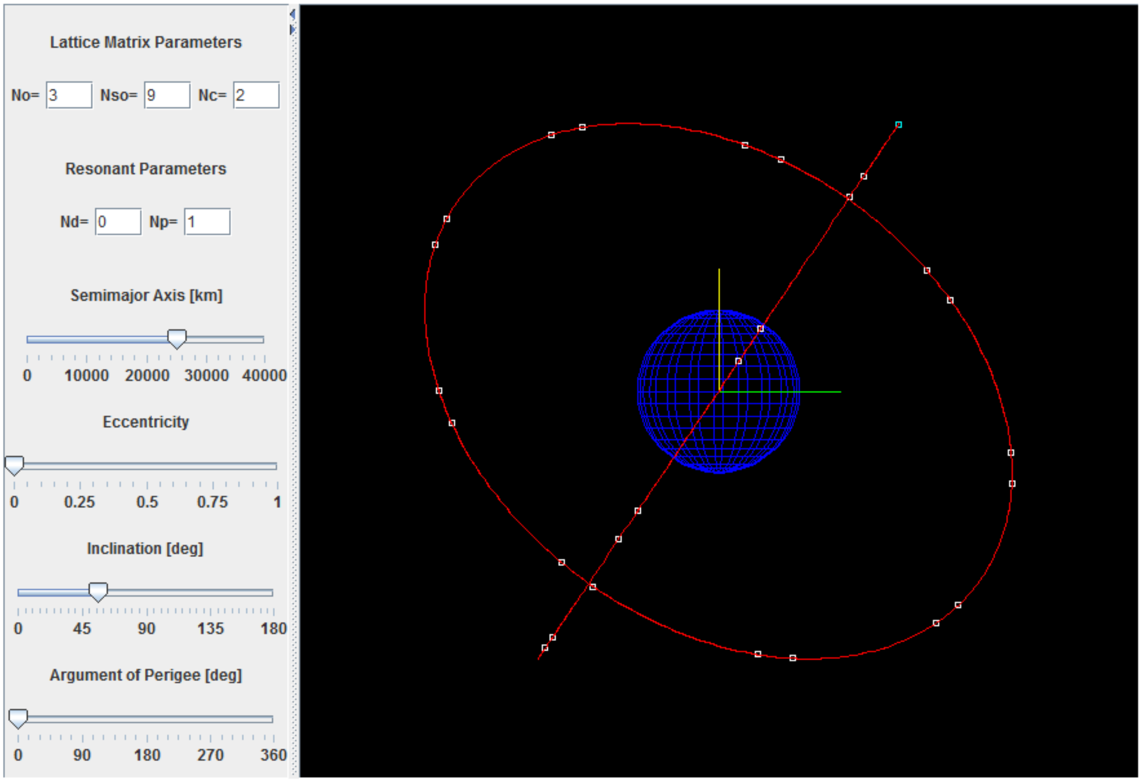

Lattice Matrix Parameters

No= 3 Nso= 9 Nc= 2

Resonant Parameters

Nd= 0 Np= 1

Figure A.1: Ikebana

A.1 2-D Lattice Flower Constellations Visualization Tool

The new version of 2-D Lattice Flower Constellation Visualization Tool is developed based on the programming of Ikebana in order to improve display performance and flexibility.

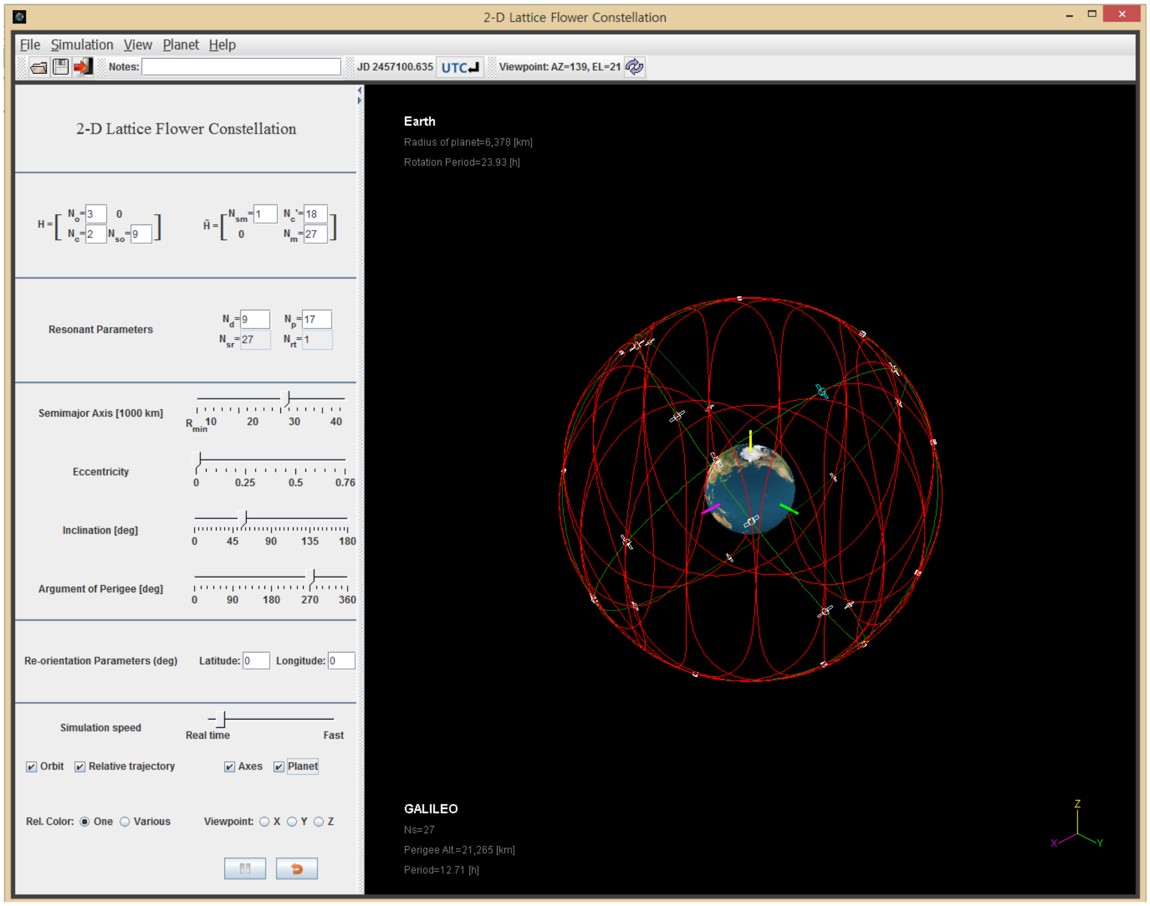

2-D Lattice Flower Constellation

Notes:

JD 2457100.635

Viewpoint: AZ=139, EL=21

2-D Lattice Flower Constellation

$H = \begin{bmatrix} N_o=3 & 0 \\ N_c=2 & N_{so}=9 \end{bmatrix}$ $\tilde{H} = \begin{bmatrix} N_{sm}=1 & N_c'=18 \\ 0 & N_m=27 \end{bmatrix}$

Resonant Parameters $N_d=9$ $N_p=17$ $N_{sr}=27$ $N_{rt}=1$

Re-orientation Parameters (deg) Latitude: 0 Longitude: 0

☑ Orbit ☑ Relative trajectory ☑ Axes ☑ Planet

Rel. Color: ● One ○ Various

Viewpoint: ○ X ○ Y ○ Z

Earth

Radius of planet=6,378 [km]

Rotation Period=23.93 [h]

GALILEO

Ns=27

Perigee Alt=21,265 [km]

Period=12.71 [h]

Figure A.2: 2-D LFC visualization tool

As shown in Figure A.2, the planet with satellites is displayed in the right part of screen. Orbits and the relative trajectories are provided with different colors. Most of the user interfaces which control various conditions are located in the left part of screen. In the user interfaces, the program provides explanation if user pushes button label. They help the user handle program easily. Basic functions such as file input, output, etc. are implemented by menu bar. User interfaces are as follows.

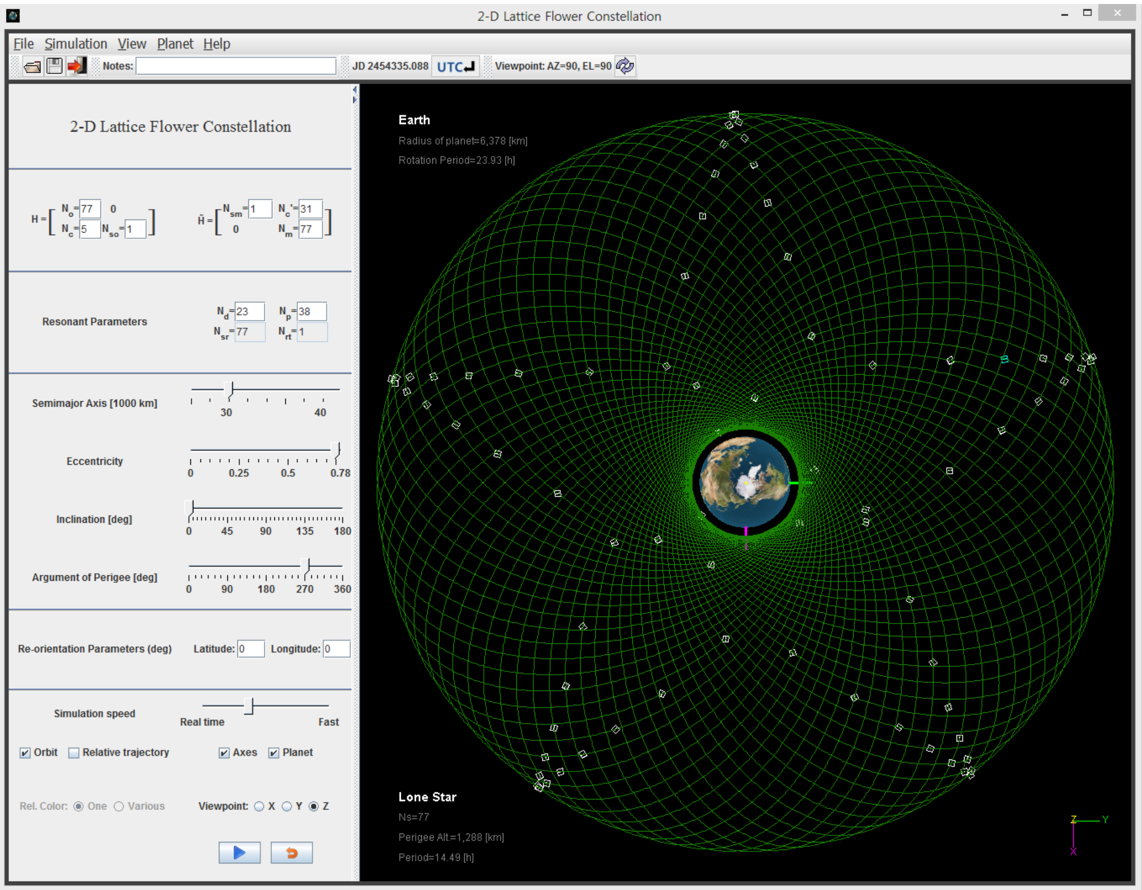

JD 2454335.088

Viewpoint: AZ=90, EL=90

$H = \begin{bmatrix} N_o = 77 & 0 \\ N_c = 5 & N_{so} = 1 \end{bmatrix}$ $\tilde{H} = \begin{bmatrix} N_{sm} = 1 & N_c' = 31 \\ 0 & N_m = 77 \end{bmatrix}$

$N_d = 23$ $N_p = 38$

$N_{sr} = 77$ $N_{rt} = 1$

Latitude: 0 Longitude: 0

☑ Orbit ☐ Relative trajectory ☑ Axes ☑ Planet

Rel. Color: ● One ○ Various Viewpoint: ○ X ○ Y ● Z

Earth

Radius of planet=6,378 [km]

Rotation Period=23.93 [h]

Lone Star

Ns=77

Perigee Alt=1,288 [km]

Period=14.49 [h]

Figure A.3: The Lone Star constellation in 2-D LFC visualization tool

- File pop-up menu : The File pop-up menu provides save the parameters for LFC to file or load the data from LFC-file. The file format is new and is compatible with extensions of Flower Constellation Visualization and Analysis Tool

(FCVAT) by Dr. Christian Bruccoleri [See Ref. 112]. Figure A.3 illustrated *The Lone Star Constellation* found in original flower constellation theory.

- Simulation pop-up menu : The Simulation pop-up menu provides switching between Planet Fixed frame and Inertial frame.
- View pop-up menu : The View pop-up menu provides various size of satellite size and satellite shape.
- Planet pop-up menu : The Planet pop-up menu provides various planet such as Sun and Mercury to be a focal point.
- Entries of H matrix : The Entries of H are meaningful physical invariants of the constellation: $h_{11} = N_o$ is the number of inertial orbits, N_{so} is the number of satellites per orbit, and $h_{21} = N_c$ is the configuration number, that controls the phasing of the satellites between orbits. Once entries of H matrix are input, upper triangular matrix $\tilde{H}$ can be calculated.
- Entries of $\tilde{H}$ matrix : The Entries of $\tilde{H}$ are carrying the following meaning: $\tilde{h}_{22} = N_m$ is the number of different mean anomalies, $\tilde{h}_{11} = N_{sm}$ is the number of inertial orbits containing satellites with a given mean anomaly, and $\tilde{h}_{12} = N_c'$ is the dual configuration number. Once entries of $\tilde{H}$ matrix are input, lower triangular matrix H can be calculated.
- Resonant parameters : In order to use compatible orbits the period, T_d, of revolution of the rotating frame and the orbital period, T_p, of the satellites must satisfy that $N_d T_d = N_p T_p$ for some positive, coprime integers N_d and N_p. Once N_d and N_p are input, the number of satellites belonging to a single relative trajectory, N_{sr}, and the number of distinct relative trajectories, N_{rt}, can be computed.

- Semi-major axis control slider : The Semi-major axis control slider varies the semi-major axis. Move the thumb by pressing the right mouse button on it and dragging it along the bar. You can also move the thumb by clicking in the bar or pressing the left mouse button.

- Eccentricity control slider : The Eccentricity control slider varies the eccentricity.

- Inclination control slider : The inclination control slider varies the inclination.

- Argument of perigee control slider : The Argument of perigee control slider varies the argument of perigee.

- Re-orientation parameters editor box : The Re-orientation parameters editor box can be used to input the desired latitude and longitude for re-orientation

- Simulation speed control slider : The Simulation speed control slider varies the speed of the simulation.

- Orbit checkbox button : The Orbit checkbox button reveals or conceals the orbits of constellation.

- Relative trajectory checkbox button : The Relative trajectory checkbox button reveals or conceals the relative trajectory.

- Axes checkbox button : The Axes checkbox button reveals or conceals the axes of coordinate.

- Planet checkbox button : The Planet checkbox button reveals or conceals the planet surface.

- Viewpoint radio button : Viewpoint radio button changes the viewpoint among default viewpoints.

- Play button : The Play button starts the satellite's orbit and the planet's rotation thread. The button label switches from "play symbol" to "pause symbol" as appropriate.

- Reset button : The Reset button initializes the program.

A.2 3-D Lattice Flower Constellations Visualization Tool

Since a relative trajectory is not available in 3-D LFC theory, 3-D Lattice Flower Constellations Visualization Tool does not provide the relative trajectory as shown in Figure A.4. Because J_2 effect causes right ascension ascending node and argument of perigee to vary secularly, the 3-D LFC Visualization Tool provides angular momentum and eccentricity vectors. User interfaces are as follows.

- N_o editor box: The N_o represent the number of orbital planes.

- N_ω editor box : The N_ω represent the number of unique orbits (with different arguments of perigee) on each plane.

- N_{so} editor box : The N_{so} represent the number of satellites on each of those orbits.

- N_{c1}, N_{c2}, and N_{c3} editor box: $N_{c1} \in [1, N_o]$, $N_{c2} \in [1, N_\omega]$, and $N_{c3} \in [1, N_o]$ are three integers (called configuration numbers) identifying the satellite phasing.

- Angular momentum vector checkbox button : The Angular momentum vector checkbox button reveals or conceals the angular momentum vector of the first orbit in the constellation.

- Eccentricity vector checkbox button : The Eccentricity vector checkbox button reveals or conceals the eccentricity vector of the first orbit in the constellation.

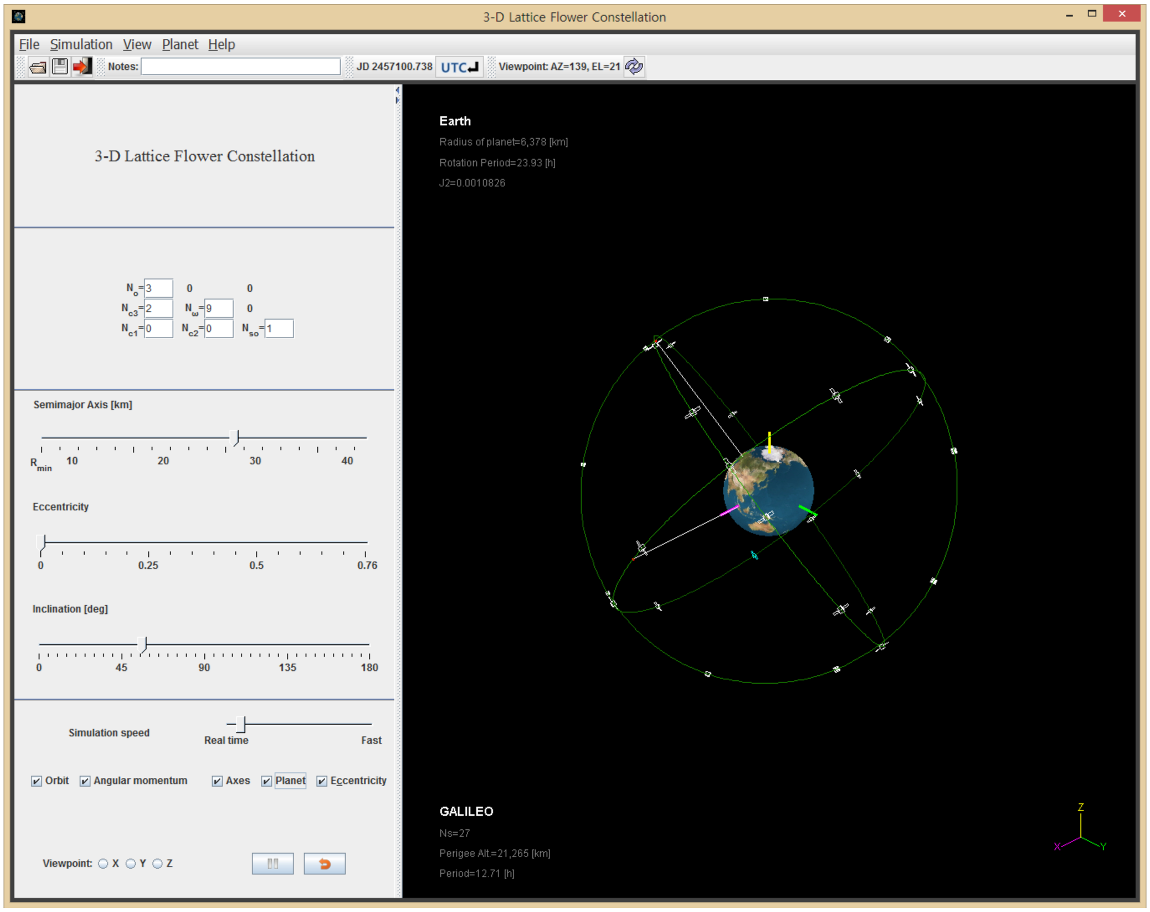

Notes:

JD 2457100.738

Viewpoint: AZ=139, EL=21

3-D Lattice Flower Constellation

N_o=3 0 0
N_{c3}=2 N_ω=9 0
N_{c1}=0 N_{c2}=0 N_{so}=1

☑ Orbit ☑ Angular momentum ☑ Axes ☑ Planet ☑ Eccentricity

Viewpoint: ○ X ○ Y ○ Z

Earth
Radius of planet=6,378 [km]
Rotation Period=23.93 [h]
J2=0.0010826

GALILEO
Ns=27
Perigee Alt.=21,265 [km]
Period=12.71 [h]

Figure A.4: 3-D LFC visualization tool